Invariant Solar Sail Formations in Elliptical Sun-Synchronous Orbits

by

Khashayar Parsay

B.S., Mathematics, University of Maryland, 2007

B.S., Aerospace Engineering, University of Maryland, 2007

M.E., Aerospace Engineering, University of Maryland, 2008

M.S., Aerospace Engineering, University of Colorado, 2013

A thesis submitted to the

Faculty of the Graduate School of the

University of Colorado in partial fulfillment

of the requirements for the degree of

Doctor of Philosophy

Department of Aerospace Engineering Sciences

2016

This thesis entitled:
Invariant Solar Sail Formations in Elliptical Sun-Synchronous Orbits
written by Khashayar Parsay
has been approved for the Department of Aerospace Engineering Sciences

_____

Dr. Hanspeter Schaub - Committee Chair

_____

Dr. Webster Cash

_____

Dr. Dale Lawrence

_____

Dr. Daniel Scheeres

_____

Dr. Trevor Williams

Date _____

The final copy of this thesis has been examined by the signatories, and we find that both the content and the form meet acceptable presentation standards of scholarly work in the above mentioned discipline.

Parsay, Khashayar (Ph.D., Aerospace Engineering Sciences)

Invariant Solar Sail Formations in Elliptical Sun-Synchronous Orbits

Thesis directed by Dr. Hanspeter Schaub - Committee Chair

Current and past missions that study the Earth's geomagnetic tail require multiple spacecraft to fly in formation about a highly eccentric Keplerian reference orbit that has its apogee inside a predefined science region of interest. Because the geomagnetic tail is directed along the Sun-Earth line and therefore rotates annually, inertially fixed Keplerian orbits are only aligned with the geomagnetic tail once per year. This limitation reduces the duration of the science phase to less than a few months annually.

Solar sails are capable of creating non-Keplerian, Sun-synchronous orbits that rotate with the geomagnetic tail. A solar sail flying in a Sun-synchronous orbit will have a continuous presence in the geomagnetic tail throughout the entire year, which significantly improves the in situ observations of the magnetosphere. To achieve a Sun-synchronous orbit, a solar sail is required to maintain a Sun-pointing attitude, which leads to the artificial precession of the orbit apse line in a Sun-synchronous manner, leaving the orbit apogee inside the science region of interest throughout entire the year.

To study the spatial and temporal variations of plasma in the highly dynamic environment of the magnetosphere, multiple spacecraft must fly in a formation. The objective for this dissertation is to investigate the feasibility of solar sail formation flying in the Earth-centered, Sun-synchronous orbit regime. The focus of this effort is to enable formation flying for a group of solar sails that maintain a nominally *fixed* Sun-pointing attitude during formation flight, solely for the purpose of precessing their orbit apse lines Sun-synchronously. A fixed-attitude solar sail formation is motivated

by the difficulties in the simultaneous control of orbit and attitude in flying solar sails.

First, the secular rates of the orbital elements resulting from the effects of solar radiation pressure (SRP) are determined using averaging theory for a Sun-pointing attitude sail. These averaged rates are used to analytically derive the necessary conditions for a drift-free solar sail formation in Sun-synchronous orbits, assuming a fixed Sun-pointing orientation for each sail in formation. Next, the problem of formation design is solved using nonlinear programming for optimal two-craft, three-craft, and four-craft solar sail formations, in terms of formation quality and stability. Finally, the problem of formation establishment is addressed using optimal control theory, assuming that the sails are capable of making small changes to their orientations with respect to the Sun. These studies demonstrate the feasibility of solar sail formation flying for exploring the geomagnetic tail and improve upon previous work, which only considered unnatural relative motions that require continuous use of active control to remain in formation.

Dedication

To my parents, Kambiz and Nasrin,

who taught me the value of education

To my fiancée, Kamala,

for her unconditional love and support

Acknowledgements

Foremost, I would like to sincerely thank my Ph.D. advisor, Dr. Hanspeter Schaub. This work would have not been possible without your support, insight, and mentorship. Your passion for research and teaching has always inspired me and I am very grateful for your encouragement and motivation throughout this work, especially when progress stalled at times. I would also like to extend my gratitude to my committee members. I am truly grateful for the discussions I had with Dr. Trevor Williams, whose extensive academic and industry experience substantially helped me on several topics in this thesis. I am indebted to Dr. Daniel Scheeres for pointing me towards previous research on the average effects of solar radiation pressure and for meeting with me to clarify my questions about his previous work on this topic. This greatly strengthened this thesis and laid the foundation for the work presented in Chapter 2. I am grateful for Dr. Dale Lawrence's suggestions, especially in addressing the control problem in Chapter 4. His attention to the smallest detail never fails to amaze me and I am truly thankful for that. I owe thanks to Dr. Webster Cash for his objective criticism and valuable suggestions especially during my comprehensive exam.

Many thanks to my good friends and former colleagues Aaron Rosengren and Daan Stevenson for their friendship and support. I am especially indebted to Aaron for our numerous discussions on Sun-synchronous orbits. Your insights and expertise helped me greatly on this thesis.

I would like to acknowledge my colleagues whom I had the privilege to work with on the NASA Magnetosphere Multi-Scale (MMS) mission, especially Laurie Mann, Jason Tichy, Stefan Novak, Neil Ottenstein, Edwin Dove, John Reagoso, Daniel Mattern, Eric Palmer, Cinnamon Wright,

Contents

Chapter

Tables

Table

Figures

Figure

Chapter 1

Introduction

1.1   Motivation

The Earth's magnetic field is continuously subjected to strong interactions with charged particles, leading to many complicated phenomena such as magnetic reconnection. Magnetic reconnection is a poorly understood phenomenon that occurs when magnetic field lines realign and magnetic energy is converted to thermal and kinetic energy (Fig. 1.1). It is responsible for the creation of magnetospheric substorms and for the energy transfer from solar wind to the magnetosphere. Magnetic reconnection is not unique to Earth's magnetosphere and it occurs ubiquitously. Thus, understanding Earth's magnetic recconection is a crucial step in demystifying the dynamics of plasma in our solar system.

Most of what is known about magnetic reconnection comes from theoretical studies and computer models. Laboratory experiments on magnetic reconnection have been carried out, such as the Magnetic Reconnection Experiment (MRX) at Princeton Plasma Physics Laboratory (PPPL). But despite five decades of research, magnetic reconnection and its overall operation remain poorly understood. Learning about magnetic reconnection will allow for the prediction of this universal process which affects our technological systems, including communications networks, GPS navigation, and electrical power grids. The key to understanding this physical process lies in the particle measurements of reconnection sites via in situ observation. The reconnection sites are initially very
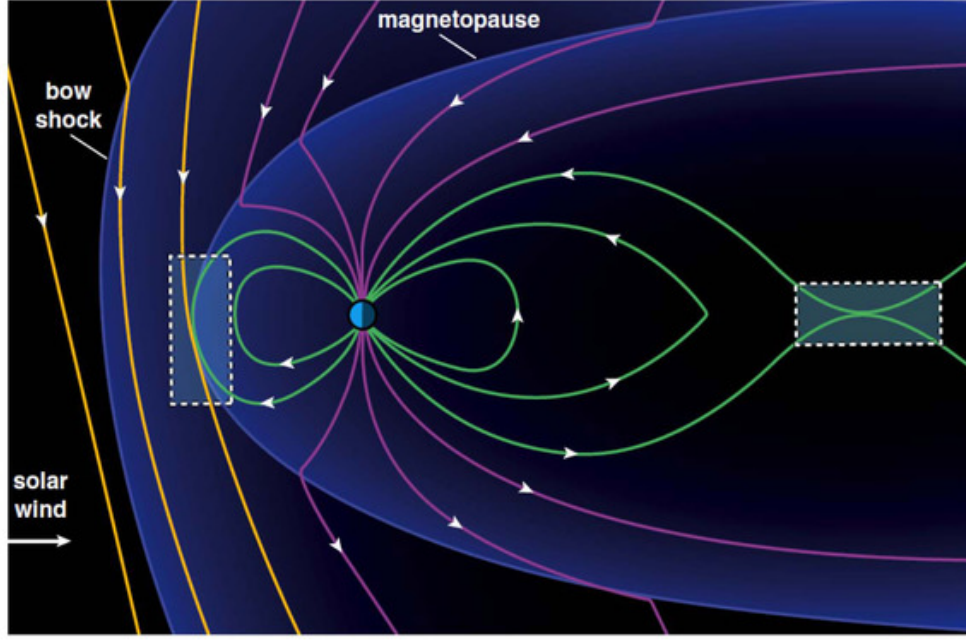
Figure 1.1: Magnetic Reconnection Sites on Day-side and Night-side of the Magnetosphere [1]

small, between 1,000-10,000 km, and vary with solar activity. Furthermore, reconnections last at most a few minutes per substorm occurance, which can happen once per three hours. For these reasons, in situ observation of magnetic reconnection is a challenging task [53, 11]. Achieving long residence times in the geomagnetic tail is therefore particularly important for studying the magnetic reconnection phenomena. It may take a few months before a single magnetic recconection event is detected and each event typically lasts only a few minutes. Therefore, the *continuous* presence of a spacecraft within the reconnection region is critical for in situ observation because it increases probability of observation.

The Earth's magnetic tail is directed along the Sun-Earth line and therefore rotates annually. Conventional magnetosphere missions require a highly elliptical orbit with its apogee inside the geomagnetic tail. The placement of the orbit apogee within a specific region of interest allows for the maximization of time the spacecraft spends in that region. An inertially fixed orbit is aligned with the geomagnetic tail only once a year, which limits the continuous presence and duration of the science phase to less than three months. **Solar sail low-thrust propulsion, however,**
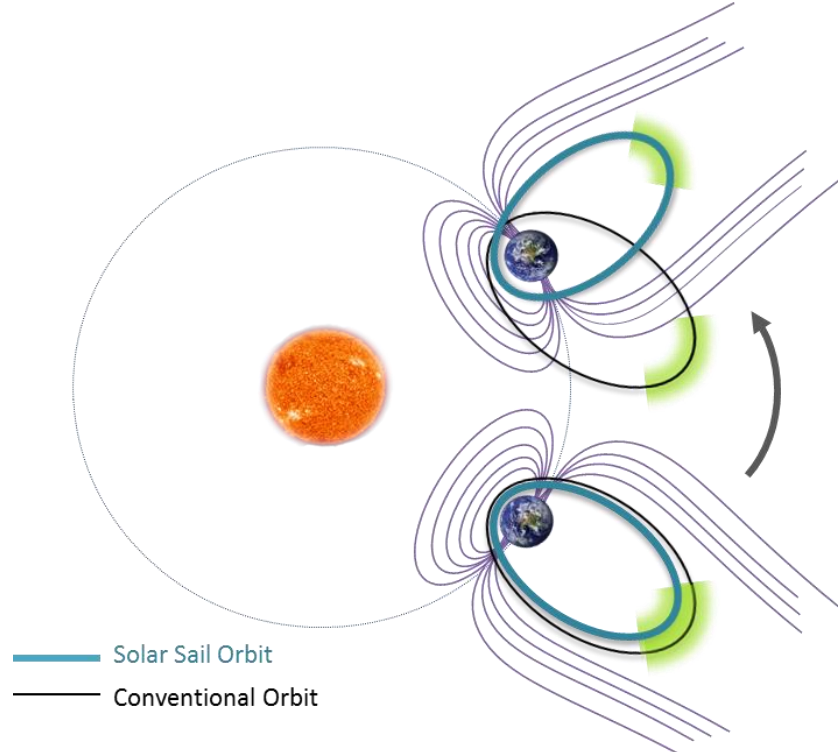
Figure 1.2: Comparison of Chemical and Solar Sail Propulsion in Geomagnetic Tail Exploration

is capable of achieving long residence times in the geomagnetic tail by continuously precessing the orbit apse line (Fig. 1.2).

A solar sail is a high area-to-mass ratio structure made of an ultra-thin reflective surface which utilizes solar radiation pressure (SRP) to propel a spacecraft in space. Unlike conventional spacecraft, the rotational and translational dynamics are highly coupled for solar sails. A small change in attitude results in a change in the total SRP net force on the sail's reflective surface area, which directly affects the translational motion of the sailcraft. The main advantage of solar sails is that they are propellant-free and are able to create highly non-Keplerian orbits. However, the applications of solar sails are limited because of their inability to generate a Sun-ward acceleration. Also, the manufacture and deployment of solar sails are quite difficult when compared to conventional spacecraft. It is for these reasons that space agencies are reserved when funding solar sail missions.
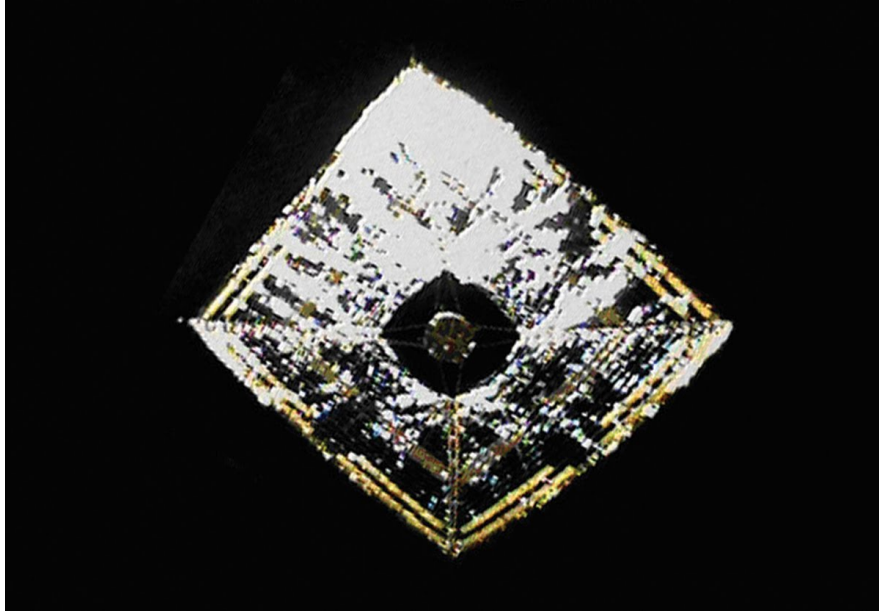
Figure 1.3: Image of IKAROS Solar Sail Immediately after Deployment [45]

The first successful solar sail mission, Interplanetary Kite-craft Accelerated by Radiation Of the Sun (IKAROS), was launched by Japan Aerospace Exploration Agency (JAXA) in May 2010 [45]. IKAROS was a fly-by mission to Venus that accomplished its goal in December 2010. IKAROS was capable of changing its reflectivity to control its attitude, in a process called *reflectivity modulation.* To change its reflectivity, liquid crystals were installed that could switch between specular and diffuse reflection modes when running current through them. Its 196 m^2 reflective surface was estimated to create a 1.12 mN force to propel the spacecraft.

Many magnetosphere missions require more than a single spacecraft to achieve their scientific objective. National Aeronautics and Space Administration's (NASA) Time History of Events and Macroscale Interactions during Substorms (THEMIS) and Magnetospheric Multi-Scale (MMS) missions, along with European Space Agency's (ESA) Cluster II mission are some of the currently active magnetosphere missions requiring multiple spacecraft to accomplish their scientific objectives. THEMIS was launched in Feb 2007 with the main scientific objective of studying auroras. It initially comprised of five spacecraft. The THEMIS mission confirmed that auroras are triggered
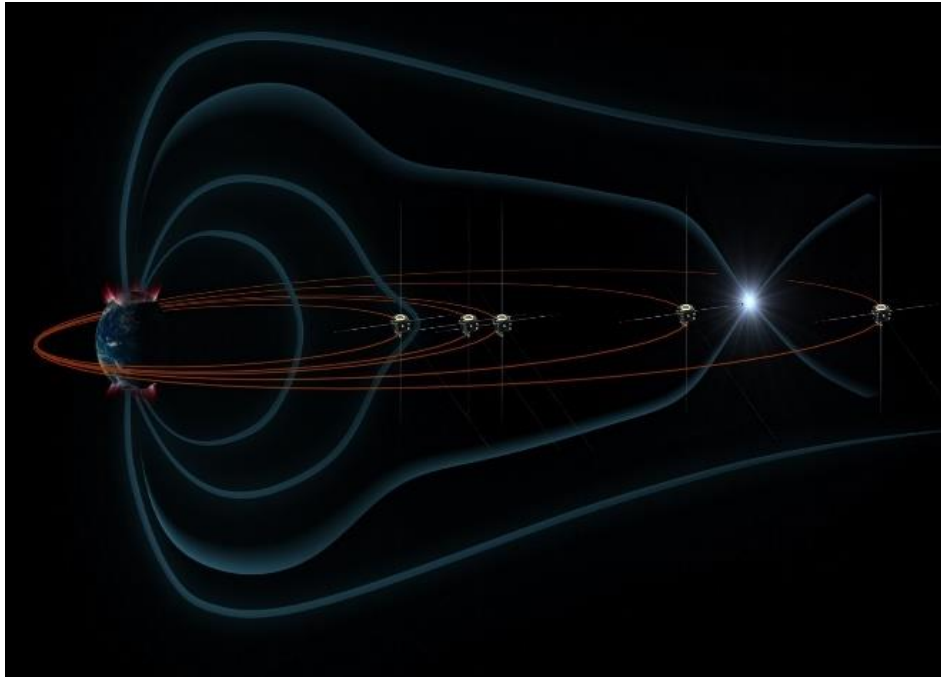
(a) THEMIS Mission Orbits [2]
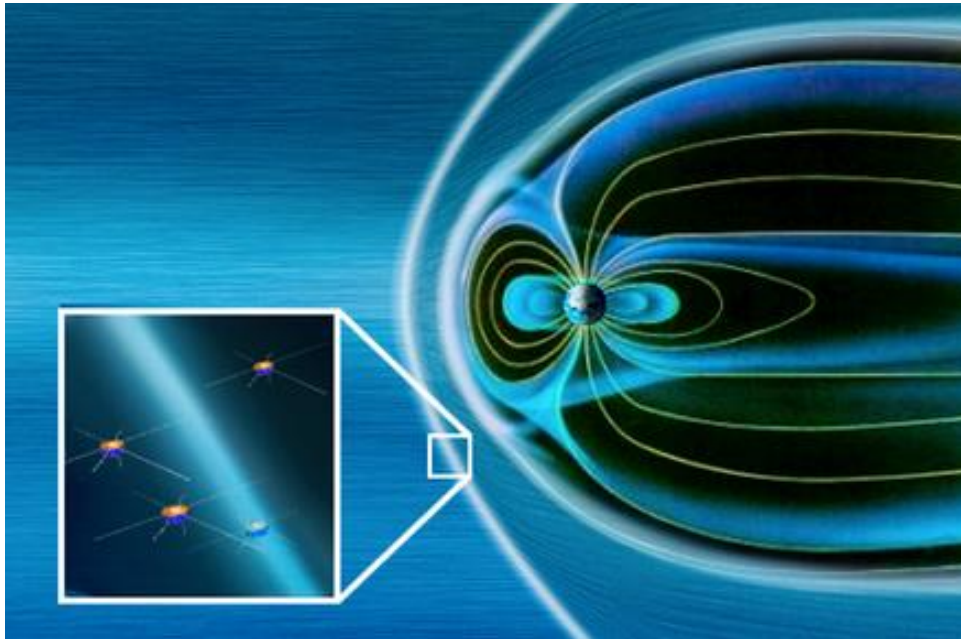
(b) Cluster II Formation [3]

Figure 1.4: Mission Orbits for THEMIS and Cluster II Mission
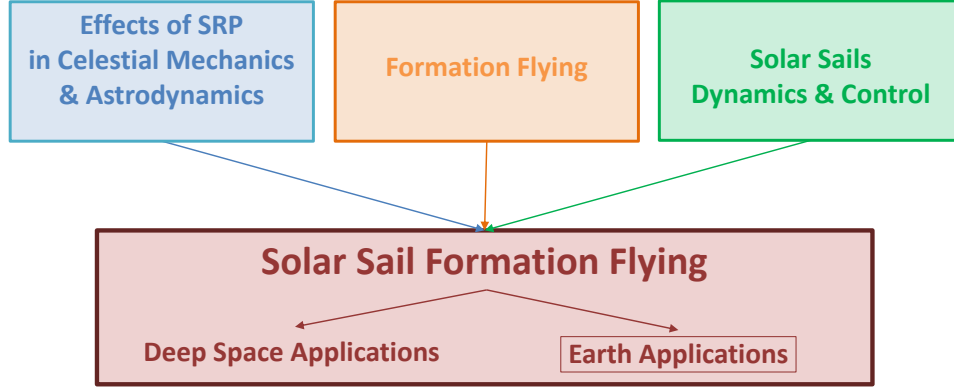
Figure 1.5: Scope of Dissertation

by magnetic reconnection. Two of the THEMIS probes are now in lunar orbits forming the Acceleration, Reconnection, Turbulence and Electrodynamics of Moon's Interaction with the Sun (ARTEMIS) mission. These two probes study the effects of the Sun's radiation on the Moon in the absence of a magnetic field to shield it. The Cluster II mission was launched in July 2000 in order to study the dayside of the magnetosphere in three dimensions over an entire solar cycle of 11 years. Cluster II uses four identical spinning spacecraft that form a tetrahedron around the orbit apogee of a 4 R_E × 19.6 R_E reference orbit with an inclination of 135°.

Generally, exploring the Earth's magnetic environment in three dimensions requires multiple satellites to fly in formation. NASA launched the MMS mission to study the three-dimensional structure of magnetic reconnection using four identical spinning spacecraft. The spacecraft form a regular tetrahedron formation within a specified region of interest around orbit apogee. The MMS mission has two primary science phases. In the first phase, the formation flies in a 1.2 R_E × 12 R_E orbit, with the apogee lying inside the dayside of the magnetosphere. In the second phase, the orbit apogee is raised from 12 R_E to 25 R_E, with the orbit apogee lying within the nightside of the magnetosphere. The duration of both science phases are less than three months because of MMS's inertially fixed orbits. Since the exact location of the magnetic reconnection is unknown and, more importantly, varies with Sun activity, the tetrahedron formation must change its size, ranging from 400 km to 10 km in terms of averaged side length.

This dissertation aims to explore the possibility of *solar sail formation flying* in Earth-centered, Sun-synchronous orbits that would allow a formation to remain in the geomagnetic tail throughout the entire year as opposed to the few months achieved using conventional spacecraft (e.g. MMS mission). This study draws from three main areas, namely, the effects of SRP in celestial mechanics and astrodynamics, formation flying, and solar sail dynamics and control (Fig. 1.5). Since controlling solar sails are very difficult in practice due to highly coupled rotational and translational dynamics, the focus is on enabling solar sail formation flying that requires minimal formation maintenance effort once the desired relative geometry is achieved. Both problems of formation design and formation establishment are explored for two-craft, three-craft, and four-craft solar sail formations.

1.2   Literature Review

Solar sailing is a relatively new field despite the fact that the original concept was introduced in 1921 [38]. Many technical hurdles, such as the development of appropriate sail material, had to be overcome before making solar sailing a reality. Recently, there has been a great interest in solar sail mission among researchers. The ability of solar sails to generate families of highly non-Keplerian orbits has led to the introduction of many new classes of missions. Both deep space and Earth applications have been considered in the literature [60]. Some of the deep space applications proposed for solar sailing are Sun-centered, Keplerian, and non-Keplerian orbits [40, 24, 23, 44, 16], high-speed interplanetary travel [56, 12, 9, 43, 32], small body deflection, rendezvous, and exploration [37, 64, 52, 37, 17, 46, 13, 42], and many N-body applications, especially in the restricted three-body problem (RTBP) [21, 50, 61, 20, 51, 41, 36, 31]. A more detailed overview of the current progress and future plans for solar sailing are discussed in Ref. [60, 38]. Fewer studies exist for Earth-centered applications. Ref. [62, 63] discuss the dynamics and control of a solar sail in an Earth-centered elliptical orbit. Many different control laws to vary orbital elements are discussed for planet-centered solar sailing in Ref. [34, 38]. An Earth pole-sitter mission employing a hybrid

sail that combines solar sailing with solar electric propulsion (SEP) is proposed and studied in Ref. [7]. Because the focus of this dissertation is studying the magnetosphere using solar sails, the literature around this particular problem is discussed next in more detail.

McInnes and Macdonald propose the novel low-cost GEOSAIL mission to explore the Earth's magnetosphere using a single low performance sail [39, 33, 34]. In the GEOSAIL mission, the approximately 2000 m^2 solar sail would fly in a moderately elliptical orbit of size 10 R_E × 30 R_E that lies in the ecliptic plane and would employ a simple Sun-pointing steering law to precess the orbit apse line Sun-synchronously, allowing the orbit apogee to remain in the geomagnetic tail throughout the entire year. It is shown that the short period eclipses around the apogee of the Sun-synchronous orbit have little effect on the required solar sail performance for the range of orbits applicable to magnetsphere missions. The GEOSAIL mission is a great candidate for a technology demonstration mission with real scientific objectives. The simple Sun-pointing attitude requirement, that is even achievable by passive means, makes this mission a feasible option for near future solar sail missions. The initial feasibility study for the GEOSAIL mission was carried out in 2007 by ESA. However, since then, there has been no announcements regarding the future of this novel mission and whether it is going to be funded.

As mentioned, many of the scientific objectives for studying the magnetosphere cannot be achieved using a single spacecraft. Gong et al. [19] continued the work of McInnes and Macdonald by proposing solar sail formation flying for exploring the geomagnetic tail. In Ref. [19], the chief solar sail achieves a Sun-synchronous orbit using the same Sun-pointing attitude proposed for the GEOSAIL mission while the deputy solar sail uses active control to enable close-proximity formation flying. A linear quadratic regulator (LQR) is utilized by the deputy solar sail to enforce a relative projected-circular orbit (PCO), which is an unnatural relative motion. Mu et al. [47] expand upon the work in Ref. [19] by applying two nonlinear-based control laws that use reflectivity modulation for enforcing a projected-circular relative motion. An example of a solar sail maintaining and establishing an in-plane PCO orbit through changes in its reflectivity and orientation are illustrated in

(a) Deputy's relative trajectory without initial error

(b) Control Effort
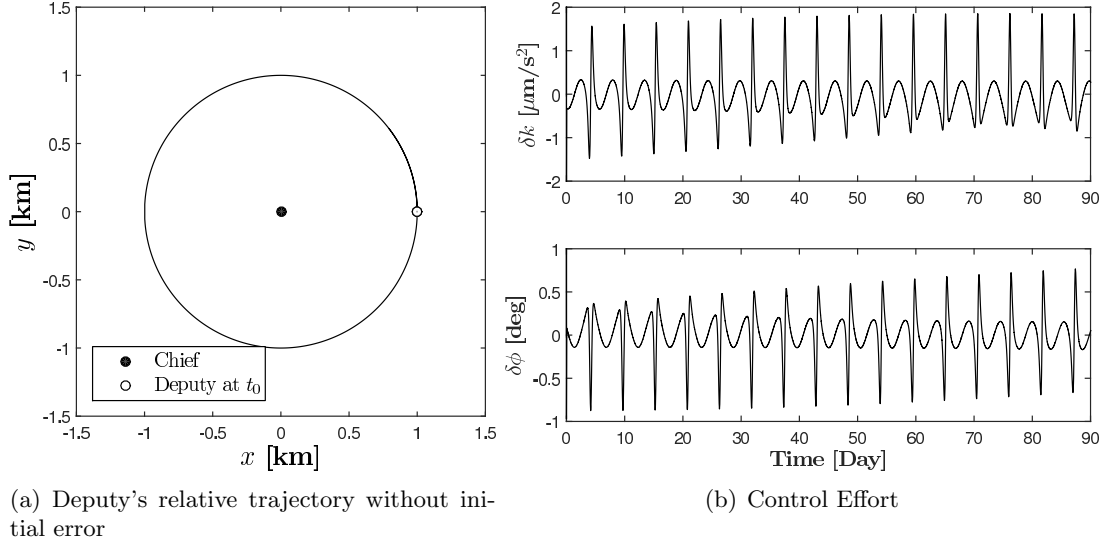
Figure 1.6: Maintenance of the Unnatural Deputy's Relative Motion in the Chief's LVLH xy Plane

Fig 1.6 and Fig. 1.7. Note that chief is maintaining a Sun-pointing attitude to artificially create a Sun-synchronous orbit. Because this formation geometry is not part of the natural relative dynamics, active control is necessary for maintaining the relative orbit. The coupled orbit and attitude control of a reflectivity modulated solar sail formation is discussed by Mu et al. in Ref. [48]. The results indicate that it is difficult to control the solar sail's attitude and orbit simultaneously using reflectivity modulation. This work is further advanced in Ref. [49] which considers the dynamics and control of a flexible solar sail under reflectivity modulation. It is found that deformation and oscillation have negligible effects on sails in terms of tracking a PCO trajectory if larger fluctuations in control inputs can be tolerated.

In general, all previous studies propose *unnatural* formation flying, where the deputy sails continuously change their orientations to maintain a desired relative motion with respect to the chief solar sail, who employs a Sun-pointing attitude to remain in a Sun-synchronous orbit. This dissertation takes a completely different approach, namely *natural* formation flying, where all solar sails in formation maintain a fixed Sun-pointing attitude solely for the purpose of precessing their orbit apse lines Sun-synchronously. In other words, this thesis focuses on determining *natural* rela-

(a) Deputy's relative trajectory with initial error

(b) Control Effort
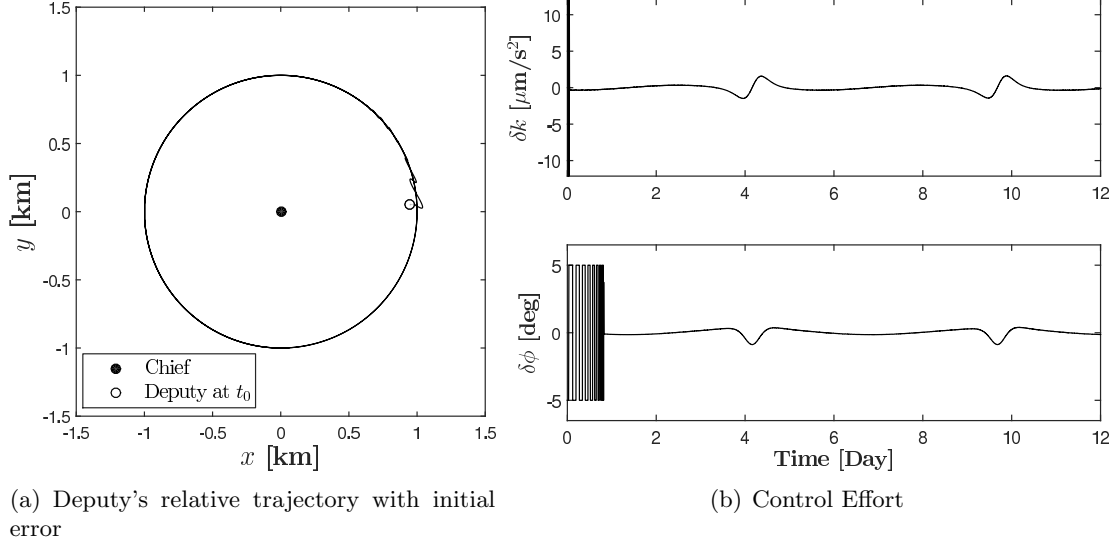
Figure 1.7: Establishment of the Unnatural Deputy's Relative Motion in the Chief's LVLH xy Plane

tive motions that do not require the deputy solar sails to continuously change their orientation in order to remain in formation; they only need to maintain a fixed Sun-pointing attitude to remain in a Sun-synchronous orbit. This approach is motivated by the significant reduction in operational cost and complexity with each solar sail employing a simple common steering law during the formation flight, instead of using active control for tracking a relative desired trajectory.

1.3   Research Objectives

This thesis aims to answer the following fundamental questions about the possibility of employing a solar sail formation in Sun-synchronous orbits for studying the magnetosphere:

(1) What are the necessary conditions for designing a natural solar sail formation that is invariant to the relative drift caused by solar radiation pressure (SRP)?

(2) How can a natural solar sail formation be designed using the necessary conditions for a SRP invariant solar sail formation?

(3) How can a natural solar sail formation be established through changes in the orientations of deputy solar sails?

This thesis is organized into three fundamental research goals:

- **Research Goal 1**: Derive necessary conditions for SRP invariant solar sail formations in Sun-synchronous orbits assuming fixed Sun-pointing attitude

- **Research Goal 2**: Design natural solar sail formations for two-craft, three-craft, and four-craft configurations (Formation Design)

- **Research Goal 3**: Determine a formation deployment strategy and establish desired formations using solar sail alone (Formation Establishment)

1.3.1   Research Goal 1

In Chapter 2, the averaged SRP dynamics of a solar sail flying in a Sun-synchronous orbit with a fixed Sun-pointing attitude similar to Ref. [39, 33, 34] are analytically derived. To minimize the secular drift between two solar sails in a formation, the secular drift rates of both sails must

be matched, which leads to the necessary conditions for designing solar sail formations with minimal relative drifts. A first-order approximation for the necessary conditions are derived next. The following outlines the specific tasks for accomplishing this thesis objective:

- Derive the averaged SRP dynamics for a solar sail in Earth-centered Sun-synchronous orbits

- Identify the secular drifts and derive the full nonlinear necessary conditions for drift-free solar sail formation flying (SRP invariant relative orbits)

- Derive the first-order necessary conditions for SRP invariant relative orbits and determine the accuracy of the first-order approximation

- Perform a sensitivity analysis with respect to sailcraft's orientation and reflectivity

1.3.2   Research Goal 2

Due to the truncation of the high order terms, the first-order conditions do not lead to truly SRP invariant relative orbits. In Chapter 3, a numerical algorithm is proposed to minimize the relative drifts between two solar sails in formation. Families of truly SRP invariant relative orbits are revealed by turning the formation design problem into a nonlinear programming problem (NLP). The problem of solar sail formation design over a specified region of interest around orbit apogee is explored for both triangle and tetrahedron formations in order to directly compare the results to active magnetosphere missions such as the Magnetosphere Multi-Scale (MMS) mission. The detailed tasks to be achieved for this research goal are listed as follows:

- Apply numerical optimization to design truly SRP invariant relative orbits in the presence of inaccuracies raised through first-order approximation

- Develop an algorithm to design a two-craft formation of a specific size within a region of interest around apogee

- Develop an algorithm to design a triangle formation of a specific size and shape within a region of interest around apogee

- Develop an algorithm to design a tetrahedron formation of a specific size and shape within a region of interest around apogee

- Numerically include the necessary conditions for SRP invariant relative orbits into the design of triangle formations and determine the effects of enforcing the condition on formation long-term stability

1.3.3   Research Goal 3

In Chapter 4, the problem of formation deployment and establishment are addressed. A simple formation deployment strategy is employed to accurately estimate the initial relative geometry. The control problem is then solved using optimal control theory, assuming that the deputy sail is capable of changing its orientation. The control effort to establish a solar sail formation is studied in detail for various formation shapes and sizes. The following outlines the specific tasks for accomplishing this thesis objective:

- Develop a simple deployment strategy to accurately estimate the initial formation geometry before applying control to establish desired formation

- Apply numerical optimal control theory to establish leader-follower formations, SRP invariant relative orbits, and triangle formations

- Explore the possibility of using a hybrid solar sail equipped with solar electric propulsion to establish a formation

1.4 Research Contributions

The following journal papers resulted from the work performed for this dissertation:

- **Parsay, K.** and Schaub, H., "Designing Solar Sail Formations in Sun-Synchronous Orbits for Geomagnetic Tail Exploration," _Acta Astronautica_, Vol. 107, 2015, pp. 218-233. doi: 10.1016/j.actaastro.2014.11.018

- **Parsay, K.** and Schaub, H., "Establishment of Natural Solar Sail Formation Using Solar Electric Propulsion," _AIAA Journal of Guidance, Control and Dynamics_, Vol. 39, No. 6, 2016, pp. 1417-1425. doi:10.2514/1.G001479

- **Parsay, K.** and Schaub, H., "Drift-Free Solar Sail Formations in Sun-Synchronous Orbits," In preparation.

- **Parsay, K.** and Schaub, H., "Optimal Establishment of a Solar Sail Formation in Sun-Synchronous Orbits," In preparation.

Chapter 2

Necessary Conditions for Solar Sail Formation Flying in Earth-Centered Sun-Synchronous Orbits

2.1 Equations of Motion for Solar Sails in Geocentric Orbits

The general equations of motion for a solar sail in an Earth orbit are written as

$$\ddot{\boldsymbol{r}} = -\frac{\mu}{r^3}\boldsymbol{r} + \boldsymbol{a}_\oplus + \boldsymbol{a}_\mathbb{C} + \boldsymbol{a}_\odot + \boldsymbol{a}_s \tag{2.1}$$

where $\boldsymbol{r}$ is the position vector of the spacecraft relative to the Earth and $\boldsymbol{a}_\oplus$, $\boldsymbol{a}_\mathbb{C}$, $\boldsymbol{a}_\odot$, and $\boldsymbol{a}_s$ are the accelerations due to Earth's nonsphericity, lunar gravitational effects, solar gravitational effects, and solar radiation pressure, respectively. The adopted inertial frame $\mathcal{N} = \{O, \boldsymbol{X}, \boldsymbol{Y}, \boldsymbol{Z}\}$ has its origin O at the center of the Earth where the $\boldsymbol{X}$ axis points from the origin to the equinox and $\boldsymbol{Z}$ points along the ecliptic north pole. The $\boldsymbol{Y}$ axis completes the right-handed coordinate system. For a flat, rigid, perfectly reflecting solar sail, the solar sail's acceleration due to the SRP can be written as

$$\boldsymbol{a}_s = k \left(\hat{\boldsymbol{n}}_s \cdot \hat{\boldsymbol{n}} \right)^2 \hat{\boldsymbol{n}} \tag{2.2}$$

where $\hat{\boldsymbol{n}}$ is a unit vector normal to the sail surface, $\hat{\boldsymbol{n}}_s$ is a unit vector from the Sun to the Earth, and the parameter k is the sail's characteristic acceleration. [38]

To determine the SRP acceleration $\boldsymbol{a}_s$, two local reference frames must be defined. Let $\mathcal{B} = \{o, \hat{\boldsymbol{n}}, \hat{\boldsymbol{t}}, \hat{\boldsymbol{l}}\}$ denote a body-fixed frame with its origin point o at the sail's center of mass while the
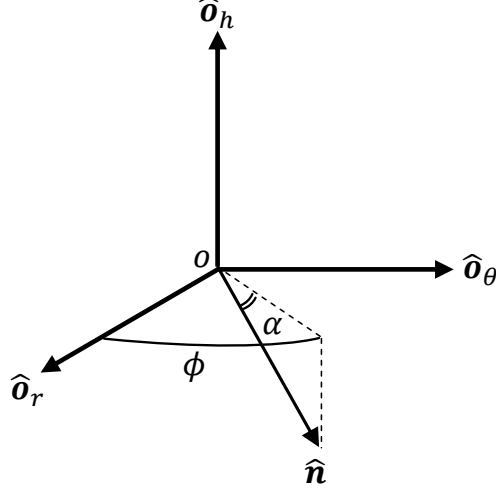
Figure 2.1: Sail's Normal Vector in the LVLH Frame

frame $\mathcal{O} = \{o, \hat{\boldsymbol{o}}_r, \hat{\boldsymbol{o}}_\theta, \hat{\boldsymbol{o}}_h\}$ is the sail's local-vertical-local-horizontal (LVLH) reference frame. As shown in Fig. 2.1, α and ϕ angles track the orientation of the $\mathcal{B}$ frame with respect to the $\mathcal{O}$ frame. The direction cosine matrix to transfer a vector expressed in the $\mathcal{O}$ frame to the $\mathcal{B}$ frame is given by

$$[\mathcal{B}\mathcal{O}] = [\boldsymbol{C}_2(\alpha)][\boldsymbol{C}_3(\phi)] \tag{2.3}$$

The sail's normal vector can then be expressed in the $\mathcal{O}$ frame as

$$^{\mathcal{O}}\hat{\boldsymbol{n}} = [\mathcal{B}\mathcal{O}]^{T}\,{}^{\mathcal{B}}\hat{\boldsymbol{n}} = \begin{bmatrix} \cos\alpha\cos\phi \\ \cos\alpha\sin\phi \\ -\sin\alpha \end{bmatrix}^{\mathcal{O}} \tag{2.4}$$

where $^{\mathcal{B}}\hat{\boldsymbol{n}} = [1\ \ 0\ \ 0]^T$ and the left-superscript indicates the frame that the $\hat{\boldsymbol{n}}$ vector is expressed in. The direction cosine matrix $[\mathcal{N}\mathcal{O}] = \begin{bmatrix} ^{\mathcal{N}}\hat{\boldsymbol{o}}_r & ^{\mathcal{N}}\hat{\boldsymbol{o}}_\theta & ^{\mathcal{N}}\hat{\boldsymbol{o}}_h \end{bmatrix}$ is used to transfer the sail's normal $^{\mathcal{O}}\hat{\boldsymbol{n}}$ from the reference frame $\mathcal{O}$ to the inertial frame $\mathcal{N}$ to be used in Eq. (2.1). Thus the sail's normal expressed in the $\mathcal{N}$ frame is

$$^{\mathcal{N}}\hat{\boldsymbol{n}} = [\mathcal{N}\mathcal{O}]\,^{\mathcal{O}}\hat{\boldsymbol{n}} \tag{2.5}$$

The sunlight direction expressed in the inertial frame $\mathcal{N}$ can be written as

$$^{\mathcal{N}}\hat{\boldsymbol{n}}_s = {}^{\mathcal{N}}\begin{bmatrix} -\cos\lambda_s \\ -\sin\lambda_s \\ 0 \end{bmatrix} \tag{2.6}$$

where the longitude of the Sun λ_s is determined through

$$\lambda_s = \lambda_{s_0} + \dot{\lambda}_s t \tag{2.7}$$

The SRP acceleration $^{\mathcal{N}}\boldsymbol{a}_s$ is determined by substituting Eq. (2.5) and Eq. (2.6) into Eq. (2.2). As illustrated in Fig. 2.2, the sail's normal $\hat{\boldsymbol{n}}$ points along the orbit apse line such that it is always directed along the Sun-line $\hat{\boldsymbol{n}}_s$. The sail's assumed orientation and orbit configuration leads to having $\phi = \pi - f$, $\alpha = 0$, and $\hat{\boldsymbol{n}}_s \cdot \hat{\boldsymbol{n}} = 1$. Therefore, the SRP acceleration $^{\mathcal{O}}\boldsymbol{a}_s$ expressed in the sail's local-vertical-local-horizontal (LVLH) frame may be written as

$$^{\mathcal{O}}\boldsymbol{a}_s = k\left(\hat{\boldsymbol{n}}_s \cdot \hat{\boldsymbol{n}}\right)^2 {}^{\mathcal{O}}\hat{\boldsymbol{n}} = {}^{\mathcal{O}}\begin{bmatrix} a_r \\ a_\theta \\ a_h \end{bmatrix} = {}^{\mathcal{O}}\begin{bmatrix} -k\cos f \\ k\sin f \\ 0 \end{bmatrix} \tag{2.8}$$

The Gauss variational equations [6] are used to determine the effects of the SRP perturbing acceleration. We have,

$$\frac{\mathrm{d}a}{\mathrm{d}f} = \frac{2pr^2}{\mu\left(1 - e^2\right)^2}\left(a_r e \sin f + a_\theta \frac{p}{r}\right) \tag{2.9a}$$

$$\frac{\mathrm{d}e}{\mathrm{d}f} = \frac{r^2}{\mu}\left[a_r \sin f + a_\theta\left(1 + \frac{r}{p}\right)\cos f + a_\theta e\frac{r}{p}\right] \tag{2.9b}$$

$$\frac{\mathrm{d}i}{\mathrm{d}f} = \frac{r^3}{\mu p}\cos\left(f + \omega\right)a_h \tag{2.9c}$$

$$\frac{\mathrm{d}\Omega}{\mathrm{d}f} = \frac{r^3}{\mu p \sin i}\sin\left(f + \omega\right)a_h \tag{2.9d}$$

$$\frac{\mathrm{d}\omega}{\mathrm{d}f} = \frac{r^2}{\mu e}\left[-a_r \cos f + a_\theta\left(1 + \frac{r}{p}\right)\sin f\right] - \frac{r^3}{\mu p \sin i}\sin\left(f + \omega\right)a_h \cos i \tag{2.9e}$$

$$\frac{\mathrm{d}t}{\mathrm{d}f} = \frac{r^2}{\sqrt{\mu p}}\left[1 - \frac{r^2}{\mu e}\left(a_r \cos f - a_\theta\left(1 + \frac{r}{p}\right)\sin f\right)\right] \tag{2.9f}$$

Because the out-of-plane component of a_h equals zero, there is no variation in the inclination and the right ascension of the ascending node. Eq. (2.8) is substituted into Eq. (2.9) and integrated over
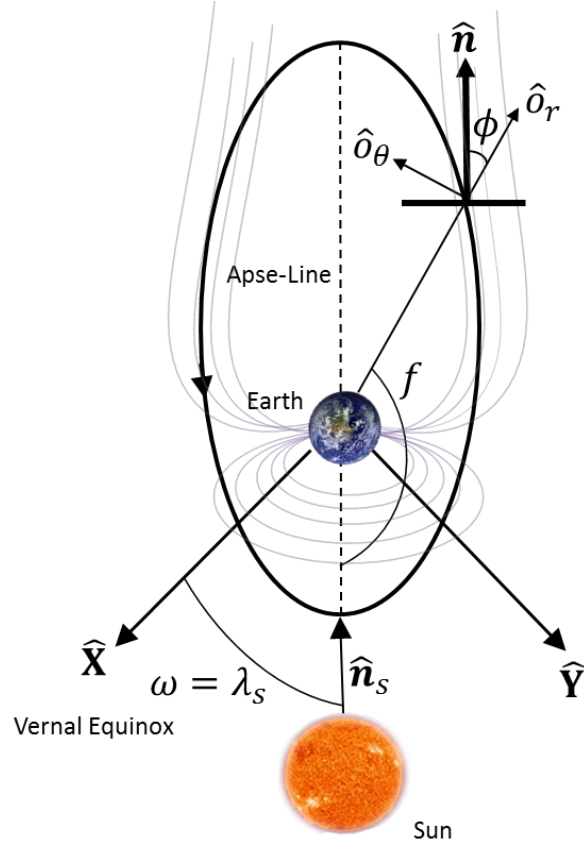
Figure 2.2: Solar Sail Geometry in Sun-Synchronous Orbit

a single orbit. The net change in the semi-major axis Δa and the net change in the eccentricity Δe over a single orbit are given by

$$\Delta a = \int_0^{2\pi} \frac{\mathrm{d}a}{\mathrm{d}f} \mathrm{d}f = 0 \tag{2.10a}$$

$$\Delta e = \int_0^{2\pi} \frac{\mathrm{d}e}{\mathrm{d}f} \mathrm{d}f = 0 \tag{2.10b}$$

For these two elements, the net change over a single orbit is zero under the SRP force. The change in the remaining orbital elements over a single orbit are

$$\Delta i = 0 \tag{2.11a}$$

$$\Delta\Omega = 0 \tag{2.11b}$$

$$\Delta\omega = \int_0^{2\pi} \frac{\mathrm{d}\omega}{\mathrm{d}f} \mathrm{d}f = \frac{3\pi a^2 \sqrt{1-e^2}k}{\mu e} \tag{2.11c}$$

To make the argument of perigee Sun-synchronous, the condition $\Delta\omega = \Delta\lambda_s$ must be satisfied over a single orbit where $\Delta\lambda_s$ is the change in the Sun's position in the ecliptic plane over a single orbit. Equivalently, the Sun-synchronous condition is written as $\Delta\omega = \Delta\lambda_s = \dot{\lambda}_s T$ where $T = \frac{2\pi}{\sqrt{\mu}}a^{\frac{3}{2}}$ is the period of the sail for a single orbit. From this condition, the required characteristic acceleration of the sail to precess the orbit apse line Sun-synchronously is determined as follows

$$k\left(a, e\right) = \frac{2}{3}\dot{\lambda}_s \frac{e}{\sqrt{(1-e^2)}}\sqrt{\frac{\mu}{a}} \tag{2.12}$$

Eq. (2.12) is used to determine the size of the solar sail for a particular desired orbit with the Sun-synchronous apse line requirement. The desired formation geometry may require that each solar sail have different a and e values. Consequently, the required characteristic acceleration may be different from one solar sail to another. Therefore, each solar sail employs the same simple steering law described with constant but different characteristic acceleration values compared to the other solar sails in the formation. The variations of the chief orbital elements under the SRP influence of Eq. (2.8) are illustrated in Fig. 2.3 for approximately 33 days for a 11 $R_E \times$ 30 R_E reference orbit that lies in the ecliptic. As shown in Fig. 2.3(a) and 2.3(b), both the semi-major axis a and eccentricity e experience periodic variations. Since $\alpha = 0$, there are no out-of-plane variations and both $i\left(t\right)$ and $\Omega\left(t\right)$ remain constant. As shown in Fig. 2.3(e), the argument of perigee increases by approximately one degree per day. This is a direct result of imposing the Sun-synchronous condition in Eq. (2.12). The required sail size to precess this reference orbit is 47×47 m^2, assuming that sail weighs 160 kg and has an efficiency of 95%. The required sail size reduces to 41×41 m^2 if the sail's mass is 120 kg. NASA's Sunjammer mission, which was canceled in October 2014 prior to launch, planned to fly a 38×38 m^2 solar sail with a total mass of 32 kg [5]. Thus, the assumptions made in this thesis about the sails' size and mass fall within the current or near future technology.

Although the effect of Earth's nonsphericity on the relative motion is minimal because of the high altitude of the orbits considered [19], the perturbations due to the gravitational effects of the Moon and Sun cannot be ignored. Thus, to illustrate the combined effects of Sun-pointing steering law and other perturbations on the osculating orbital elements, the mission orbit is propagated for a

full year according to Eq. (2.1), starting at the spring equinox (March 20, 2015) with an equatorial inclination of $23.4°$ corresponding to an orbit that lies in the ecliptic plane. The variations in the chief's orbital elements over one year is shown in Fig. 2.4. Despite the variations in orbit eccentricity and inclination, the argument of perigee remains Sun-synchronous.

(a) Semi-Major Axis

(b) Eccentricity

(c) Inclination

(d) Right Ascenstion of Ascending Node

(e) Argument of Perigee

(f) Motion in Inertial Frame
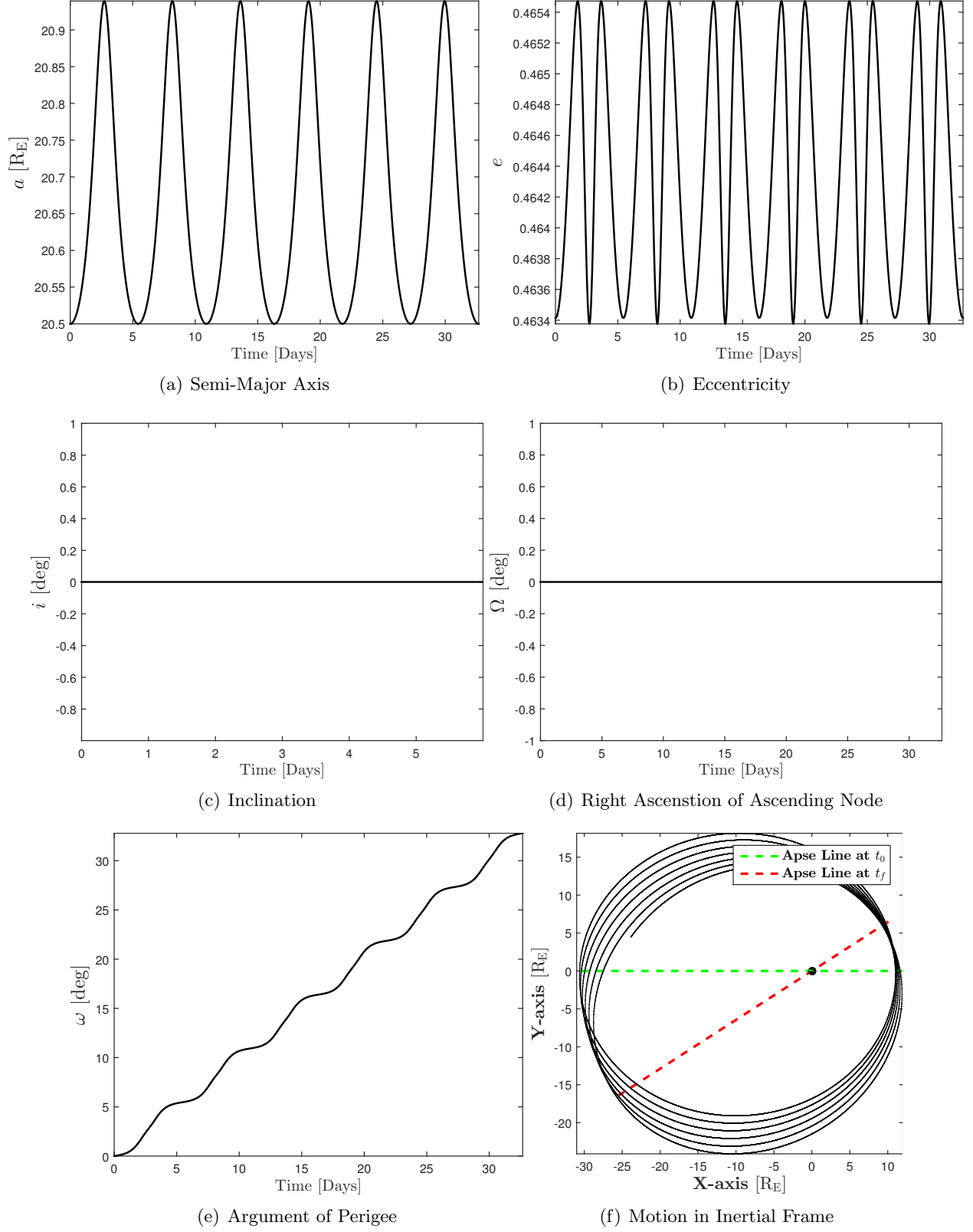
Figure 2.3: Sail's Orbital Elements Variations

(a) Semi-Major Axis

(b) Eccentricity

(c) Inclination

(d) Argument of Perigee
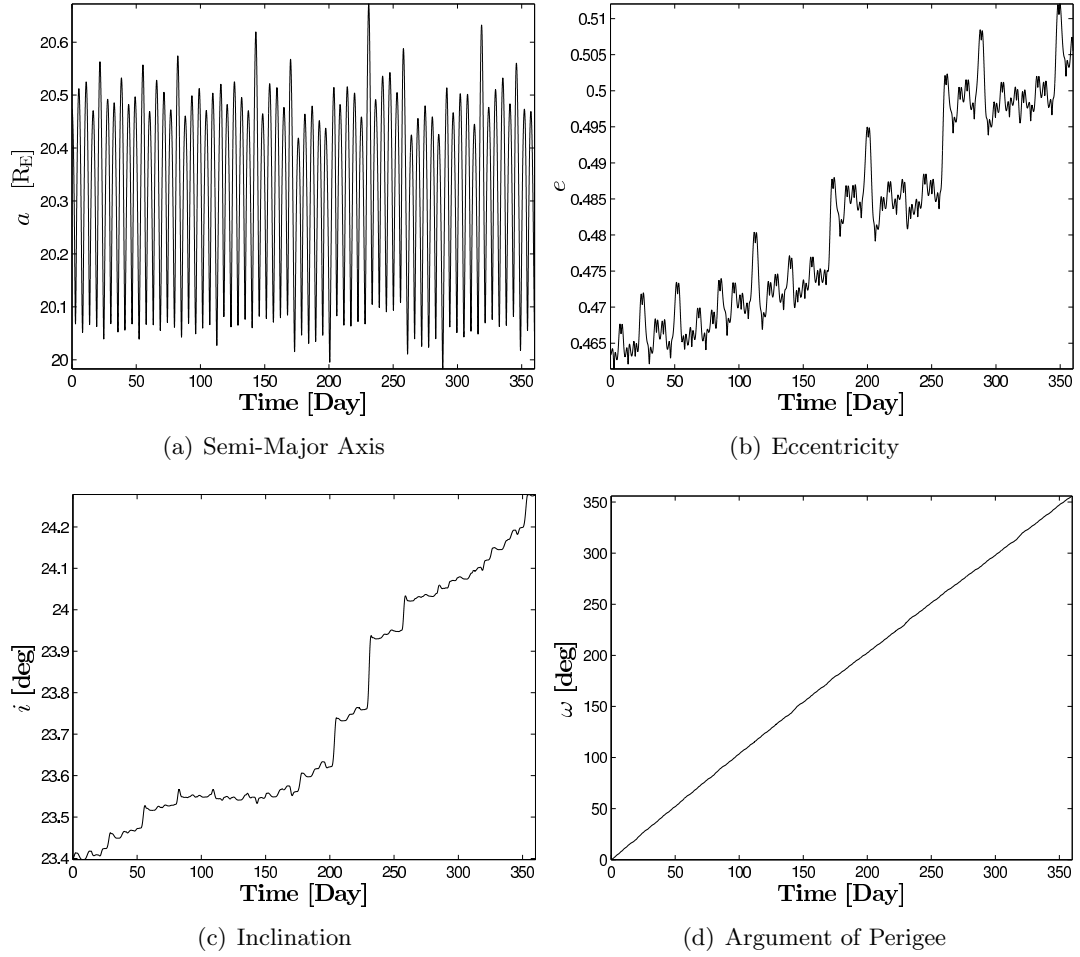
Figure 2.4: Variations of Chief's Orbital Elements under Perturbations

2.2 Average Effects of SRP in Sun-Synchronous Orbits

In this section, averaging theory is used to determine the secular variations in the orbital elements due to the SRP perturbing force in Sun-synchronous orbits. Classical averaging theory was mainly developed in order to study nonlinear non-autonomous systems [4] and it's a powerful tool in determining the long-term dynamics of artificial and natural satellites in orbital mechanics. The Gauss Variational equations are given as follows [6]

$$\dot{a} = \frac{2a^2}{h}\left(e\sin f a_r + \frac{p}{r}a_\theta\right) \tag{2.13a}$$

$$\dot{e} = \frac{1}{h}\left(p\sin f a_r + \left[(p+r)\cos f + re\right]a_\theta\right) \tag{2.13b}$$

$$\dot{i} = \frac{r\cos\theta}{h}a_h \tag{2.13c}$$

$$\dot{\Omega} = \frac{r\sin\theta}{h\sin i}a_h \tag{2.13d}$$

$$\dot{\omega} = \frac{1}{he}\left(-p\cos f a_r + (p+r)\sin f a_\theta\right) \tag{2.13e}$$

$$\dot{M} = n + \frac{b}{ahe}\left((p\cos f - 2re)a_r - (p+r)\sin f a_\theta\right) \tag{2.13f}$$

After substituting the SRP perturbing acceleration in Eq. (2.8) into Eq. (2.13), we have

$$\dot{a} = \frac{2a^2 k \sin f}{\sqrt{a\left(1-e^2\right)\mu}} \tag{2.14a}$$

$$\dot{e} = \frac{k\sqrt{a\left(1-e^2\right)\mu}(e+\cos f)\sin f}{\mu(1+e\cos f)} \tag{2.14b}$$

$$\dot{\omega} = \frac{k\sqrt{a\left(1-e^2\right)\mu}(2e\cos f - \cos 2f + 3)}{2e\mu(1+e\cos f)} \tag{2.14c}$$

$$\dot{M} = n + \frac{k\left(a^2\left(1-e^2\right)\right)^{3/2}(2e\cos f + \cos 2f - 3)}{2a^2e\sqrt{a\left(1-e^2\right)\mu}(e\cos f + 1)} \tag{2.14d}$$

Note the appearance of the true anomaly variable f in all terms. To remove the short-term variations and extract the secular variations, we average each element separately as follows [4],

$$\dot{\bar{a}} = \frac{1}{2\pi} \int_0^{2\pi} \dot{a} \, \mathrm{d}M = \frac{1}{2\pi} \int_0^{2\pi} \gamma \, \dot{a} \, \mathrm{d}f \tag{2.15a}$$

$$\dot{\bar{e}} = \frac{1}{2\pi} \int_0^{2\pi} \dot{e} \, \mathrm{d}M = \frac{1}{2\pi} \int_0^{2\pi} \gamma \, \dot{e} \, \mathrm{d}f \tag{2.15b}$$

$$\dot{\bar{\omega}} = \frac{1}{2\pi} \int_0^{2\pi} \dot{\omega} \, \mathrm{d}M = \frac{1}{2\pi} \int_0^{2\pi} \gamma \, \dot{\omega} \, \mathrm{d}f \tag{2.15c}$$

$$\dot{\bar{M}} = \frac{1}{2\pi} \int_0^{2\pi} \dot{M} \, \mathrm{d}M = \frac{1}{2\pi} \int_0^{2\pi} \gamma \, \dot{M} \, \mathrm{d}f \tag{2.15d}$$

The averaging must be performed with respect to the mean anomaly variable M. Because the equations in Eq. (2.14) are all expressed in terms of true anomaly, a change of variable is required before performing the integration. This change of variable is given by,

$$\mathrm{d}M = \frac{n}{h} r^2 \, \mathrm{d}f = \gamma \, \mathrm{d}f \tag{2.16}$$

Performing the integration, the secular variations of orbital elements due to the SRP force are written as,

$$\dot{\bar{a}} = 0 \tag{2.17a}$$

$$\dot{\bar{e}} = 0 \tag{2.17b}$$

$$\dot{\bar{\omega}} = \frac{3k\sqrt{\bar{a}\left(1 - \bar{e}^2\right)}}{2\bar{e}\sqrt{\mu}} \tag{2.17c}$$

$$\dot{\bar{M}} = \bar{n} - \frac{3\sqrt{\bar{a}}\left(1 + \bar{e}^2\right)k}{2\bar{e}\sqrt{\mu}} \tag{2.17d}$$

Note that if we assume that the characteristic acceleration is governed by Eq. (2.12), then Eq. (2.17) simplifies to the following expressions,

$$\dot{\bar{a}} = 0 \tag{2.18a}$$

$$\dot{\bar{e}} = 0 \tag{2.18b}$$

$$\dot{\bar{\omega}} = \dot{\lambda}_s \tag{2.18c}$$

$$\dot{\bar{M}} = \bar{n} - \frac{1 + \bar{e}^2}{\sqrt{1 - \bar{e}^2}} \dot{\lambda}_s \tag{2.18d}$$

The average value of a is zero which is a classical result; the semi-major axis experiences no secular change as a result of SRP perturbation. It turns out that the eccentiricity experiences no secular variation for a solar sail in a Sun-synchronous orbit. This is also evident by the previous result given in Eq. (2.10b) and Fig. 2.3(b). The only two elements that experience secular variations are the argument of perigee ω and the mean anomaly M. Note that if $k = 0$ (no reflectivity), we would have $\dot{\omega} = 0$, and $\dot{M} = n$ which are the classical results from the two-body problem. The results in Eq. (2.17) are critical for determining the necessary conditions to fly a drift-free solar sail formation in a Sun-synchronous orbit. The next section details how Eq. (2.17) may be used to derive first-order necessary conditions for SRP invariant relative motion in Sun-synchronous orbits.

2.3   Necessary Conditions for SRP Invariant Relative Motion

For the relative motion of two solar sails in Sun-synchronous orbits to remain invariant to the relative effects of SRP, the following two secular drift rates must be matched,

$$\dot{\bar{\omega}}_d = \dot{\bar{\omega}}_c \tag{2.19a}$$

$$\dot{\bar{M}}_d = \dot{\bar{M}}_c \tag{2.19b}$$

Assuming that two solar sails are flying in close-proximity and have a negligible difference between their characteristic accelerations, the first-order approximation of the deputy's average rates can be written in terms of the chief's average rates using,

$$\dot{\bar{\omega}}_d = \dot{\bar{\omega}}_c \left(\bar{a}_c, \bar{e}_c, k_c \right) + \delta\dot{\bar{\omega}} = \dot{\bar{\omega}}_c + \frac{\partial \dot{\bar{\omega}}}{\partial \bar{a}} \bigg|_{\bar{a}_c, \bar{e}_c, k_c} \delta\bar{a} + \frac{\partial \dot{\bar{\omega}}}{\partial \bar{e}} \bigg|_{\bar{a}_c, \bar{e}_c, k_c} \delta\bar{e} + \frac{\partial \dot{\bar{\omega}}}{\partial k} \bigg|_{\bar{a}_c, \bar{e}_c, k_c} \delta k \tag{2.20a}$$

$$\dot{\bar{M}}_d = \dot{\bar{M}}_c \left(\bar{a}_c, \bar{e}_c, k_c \right) + \delta\dot{\bar{M}} = \dot{\bar{M}}_c + \frac{\partial \dot{\bar{M}}}{\partial \bar{a}} \bigg|_{\bar{a}_c, \bar{e}_c, k_c} \delta\bar{a} + \frac{\partial \dot{\bar{M}}}{\partial \bar{e}} \bigg|_{\bar{a}_c, \bar{e}_c, k_c} \delta\bar{e} + \frac{\partial \dot{\bar{M}}}{\partial k} \bigg|_{\bar{a}_c, \bar{e}_c, k_c} \delta k \tag{2.20b}$$

where the the partials are all evaluated with respect to the chief's orbital elements and can be expressed using,

$$\left.\frac{\partial \dot{\omega}}{\partial \bar{a}}\right|_{\bar{a},\bar{e},k} = \frac{3\left(1 - \bar{e}^2\right) k}{4\bar{e}\sqrt{\bar{a}\left(1 - \bar{e}^2\right)\mu}} \tag{2.21a}$$

$$\left.\frac{\partial \dot{\omega}}{\partial \bar{e}}\right|_{\bar{a},\bar{e},k} = -\frac{3\bar{a}k}{2\bar{e}^2\sqrt{\bar{a}\left(1 - \bar{e}^2\right)\mu}} \tag{2.21b}$$

$$\left.\frac{\partial \dot{\omega}}{\partial k}\right|_{\bar{a},\bar{e},k} = \frac{3\sqrt{\bar{a}\left(1 - \bar{e}^2\right)}}{2\bar{e}\sqrt{\mu}} \tag{2.21c}$$

$$\left.\frac{\partial \dot{M}}{\partial \bar{a}}\right|_{\bar{a},\bar{e},k} = -\frac{3\left(\bar{a}^2\left(1 + \bar{e}^2\right) k + 2\bar{e}\mu\right)}{4\bar{a}^{5/2}\bar{e}\sqrt{\mu}} \tag{2.22a}$$

$$\left.\frac{\partial \dot{M}}{\partial \bar{e}}\right|_{\bar{a},\bar{e},k} = \frac{3\sqrt{\bar{a}}\left(1 - \bar{e}^2\right) k}{2\bar{e}^2\sqrt{\mu}} \tag{2.22b}$$

$$\left.\frac{\partial \dot{M}}{\partial k}\right|_{\bar{a},\bar{e},k} = -\frac{3\sqrt{\bar{a}}\left(1 + \bar{e}^2\right)}{2\bar{e}\sqrt{\mu}} \tag{2.22c}$$

Inspecting Eq. (2.20), in order to match the chief and deputy secular rates to the first-order approximation, the first variations of $\delta\dot{\omega}$ and $\delta\dot{M}$ must vanish. Therefore, the **first-order necessary conditions for SRP invariant relative orbits** are determined by,

$$\delta\dot{\omega} = \left.\frac{\partial \dot{\omega}}{\partial \bar{a}}\right|_{\bar{a},\bar{e},k} \delta\bar{a} + \left.\frac{\partial \dot{\omega}}{\partial \bar{e}}\right|_{\bar{a},\bar{e},k} \delta\bar{e} + \left.\frac{\partial \dot{\omega}}{\partial k}\right|_{\bar{a},\bar{e},k} \delta k = 0 \tag{2.23a}$$

$$\delta\dot{M} = \left.\frac{\partial \dot{M}}{\partial \bar{a}}\right|_{\bar{a},\bar{e},k} \delta\bar{a} + \left.\frac{\partial \dot{M}}{\partial \bar{e}}\right|_{\bar{a},\bar{e},k} \delta\bar{e} + \left.\frac{\partial \dot{M}}{\partial k}\right|_{\bar{a},\bar{e},k} \delta k = 0 \tag{2.23b}$$

The differential elements $\delta\bar{a}$, $\delta\bar{e}$, and δk are used to determine the deputy's averaged elements using,

$$k_d = k_c + \delta k \tag{2.24a}$$

$$\bar{a}_d = \bar{a}_c + \delta\bar{a} \tag{2.24b}$$

$$\bar{e}_d = \bar{e}_c + \delta\bar{e} \tag{2.24c}$$

As evident in Eq. (2.23), there are **two constraints** ($\delta\dot{\omega} = 0$ and $\delta\dot{M} = 0$) that the deputy states must satisfy for a SRP invariant relative motion with respect to a chief solar sail flying

in a Sun-synchronous orbit. These two constraints are functions of **three variables** ($\delta\bar{a}$, $\delta\bar{e}$, and δk). Therefore, there is only **one free variable** to choose; once a variable is chosen, the other two free variables are prescribed such that both SRP invariant conditions in Eq. (2.23) are satisfied. For instance, if the deputy solar sail has a fixed characteristic acceleration, there is only one unique orbit that the deputy can occupy that leads to a SRP invariant relative motion with respect to the chief flying in a Sun-synchronous orbit. The concept of SRP invariant relative orbits are analogous to J_2 invariant relative orbits that were introduced by Alfriend and Schaub in Ref. [58]. The difference is that the Earth's oblateness causes secular drifts in three of the orbital elements ω, Ω, and M.

2.4   A Trivial Solution for SRP Invariant Relative Motion

A *trivial solution* in the families of SRP invariant relative orbits is the leader-follower or string of pearls formation for two solar sails that have the same characteristic acceleration. When two solar sails are in a leader-follower formation ($a_d = a_c$ and $e_d = e_c$) and have the same characteristic acceleration, the secular rates are identically matched, as evident in Eq. 2.17. A natural leader-follower formation may be established if the following initial differential orbital elements are established at orbit apogee of the chief's solar sail,

$$\delta\text{œ}_0 = \begin{bmatrix} 0 & 0 & 0 & 0 & 0 & \delta f_0 \end{bmatrix}^T \tag{2.25}$$

If the chief is in a circular orbit, the deputy holds a constant offset behind or ahead of the chief throughout the entire orbit, depending on the sign of δf_0. For a chief in an eccentric orbit, the deputy's relative motion is a bounded periodic motion that takes place behind the chief if $\delta f_0 < 0$ and ahead of the chief if $\delta f_0 > 0$ and satisfies the following condition at orbit apogee [59]

$$\frac{\dot{y}_0}{x_0} = \frac{-n\,(2 - e)}{\sqrt{(1 - e)\,(1 + e)^3}} \tag{2.26}$$

where n and e are the chief's mean motion and eccentricity, respectively. The formation size is only dependent on the magnitude of δf_0. An example of such relative motion is illustrated in
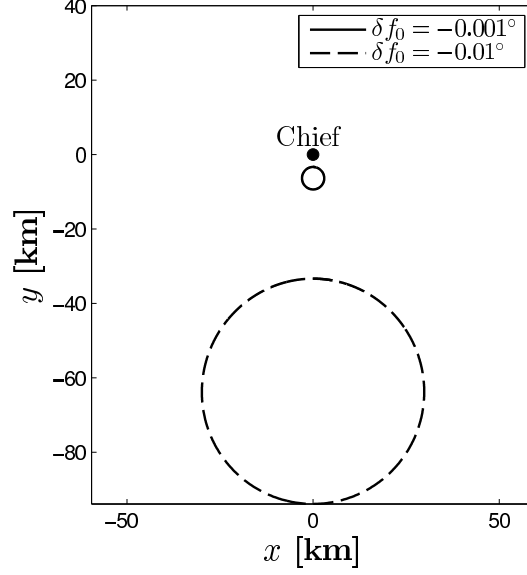
Figure 2.5: Deputy's Keplerian Relative Motion in the Chief's LVLH Frame for Two Different True Anomaly Offsets

Fig. 2.5 for two different formation sizes of $\delta f_0 = -0.001°$ and $\delta f_0 = -0.01°$. The minimum and maximum distances between the chief and deputy sails occur at the chief's apogee and perigee, respectively. The minimum distance can be analytically computed using the along-track equation given in Eq. (2.27) [57],

$$y \approx r_c \left(\delta f + \delta \omega + \delta \Omega \cos i \right) \tag{2.27}$$

Since $\delta\omega = \delta\Omega = 0$, the minimum distance is determined as

$$y_{\min} = r_c \delta f \tag{2.28}$$

To determine the center and the radius of the relative circular orbit (leader-follower formation), the relative motion is propagated for a full orbit and a least-squares solution is used to fit a circle to the deputy's relative motion. Let (x_o, y_o) and R denote the center and the radius of the relative circular motion of the deputy. To determine (x_o, y_o) and R, the following problem must be solved,

$$\text{minimize} \quad J = \sum_{i=1}^{N} \left[(x_i - x_o)^2 + (y_i - y_o)^2 - R^2 \right]^2 \tag{2.29}$$

$$\text{with respect to} \quad x_o, y_o, R$$

where N is the number of integration steps taken in propagating the formation for one full orbit. This minimization problem may be converted to a simple least-squares problem by a change of variables. Expanding the cost function leads to

$$J = \sum_{i=1}^{N} \left(x_i^2 - 2x_i x_o + y_i^2 - 2y_i y_o + w \right)^2$$

where $w = x_o^2 + y_o^2 - R^2$ is used as a new variable. Let $\boldsymbol{\epsilon} = \mathbf{A}\mathbf{x} - \mathbf{b}$ where

$$\mathbf{A} = \begin{bmatrix} -2x_1 & -2y_1 & 1 \\ -2x_2 & -2y_2 & 1 \\ \vdots & \vdots & \vdots \\ -2x_N & -2y_N & 1 \end{bmatrix}, \mathbf{x} = \begin{bmatrix} x_o \\ y_o \\ w \end{bmatrix}, \mathbf{b} = - \begin{bmatrix} x_1^2 + y_1^2 \\ x_2^2 + y_2^2 \\ \vdots \\ x_N^2 + y_N^2 \end{bmatrix}$$

Hence, the cost function in Eq. (3.3) may now be rewritten as $J = \|\boldsymbol{\epsilon}\|_2^2$. The center and the radius of the circular relative motion are found using the least-squares solution $\mathbf{x} = \left(\mathbf{A}^T \mathbf{A} \right)^{-1} \mathbf{A}^T \mathbf{b}$. The radius of the relative circular orbit is solved using $R = \sqrt{x_o^2 + y_o^2 - w}$. For the $\delta f_0 = -0.001°$ case shown in Fig. 2.5, the center and the orbit radius of the deputy's relative motion are $(x_o, y_o) = (0, -6.33)$ km and $R = 2.98$ km. For the formation size $\delta f_0 = -0.01°$, they are $(x_o, y_o) = (0, -63.3)$ km and $R = 29.8$ km.

The formation stability of the natural leader-follower formation under gravitational and SRP perturbations is examined for a solar sail formation established using $\delta \boldsymbol{œ}_0 = \begin{bmatrix} 0 & 0 & 0 & 0 & 0 & -0.001° \end{bmatrix}^T$. The simulation is generated for two different periods as illustrated in Fig. 2.6. The relative out-of-plane motion degrades but the effect is negligible, with a maximum out-of-plane separation of only 9 m. The formation remains quasi-periodic even after six months, despite the secular drift in the along-track direction. In reality, the achievement of the desired differential elements is bound to have small errors. Thus, formation reconfiguration is necessary after a few months. Although the natural-leader follower formation requires no control effort from the deputy sail to maintain the formation, there are challenges in establishing the desired formation. The establishment of a natural solar sail formation is discussed in Chapter 4.

(a) 3 months

(b) 6 months
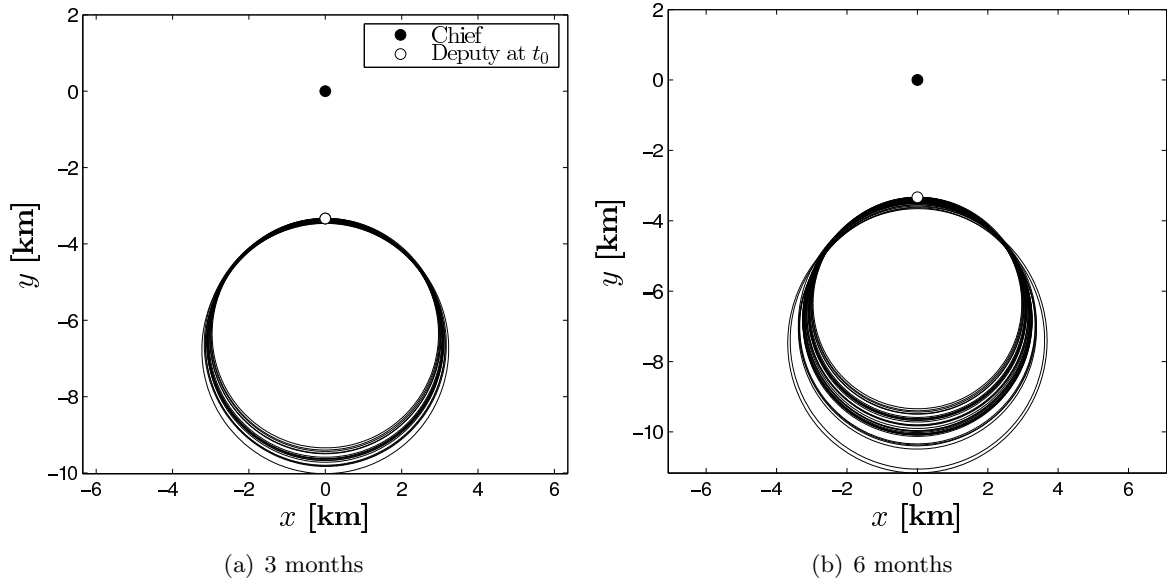
Figure 2.6: Deputy's Relative Motion in the Chief's LVLH xy Plane Under Perturbations

2.5   Analytical Design of SRP Invariant Relative Motion

Given the chief's averaged elements and characteristic acceleration, an SRP invariant formation is established using the following procedure, assuming that the free variable is δk. After choosing a δk value that is within the deputy's reflectivity modulation capability, the two invariant conditions in Eq. (2.23) are solved for the averaged element differences between the deputy and chief solar sails. The averaged deputy's elements are then solved using Eq. (2.24). The deputy's osculating elements will then be solved using an iterative process.

A few quasi-periodic relative orbits that are designed using the procedure described are illustrated in Fig. 2.8. For each case, the formation is propagated for 10 orbits (approximately 55 days). Despite the enforcement of the SRP invariant relative conditions, the formations experience secular drifts. This is directly related to the fact that the condition derived is only accurate to the first-order. Larger δk values lead to faster drift rates since the linear first-order assumption for deriving the necessary conditions is more accurate for smaller δk values, such as the one shown in Fig. 2.8(e). In Chapter 3, a numerical optimization is employed to remove the secular drifts shown in Fig. 2.8. The numerical approach allows the design of truly SRP invariant solar sail formations in Sun-synchronous orbits.
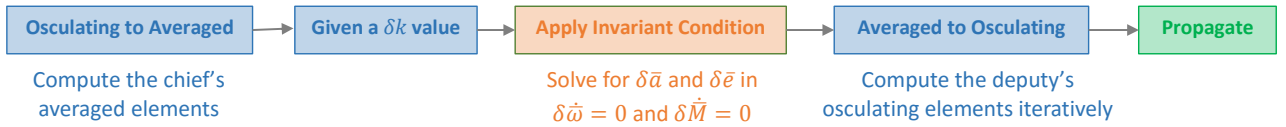
Figure 2.7: Procedure to Design a SRP Invariant Solar Sail Formation in Sun-Synchronous Orbits
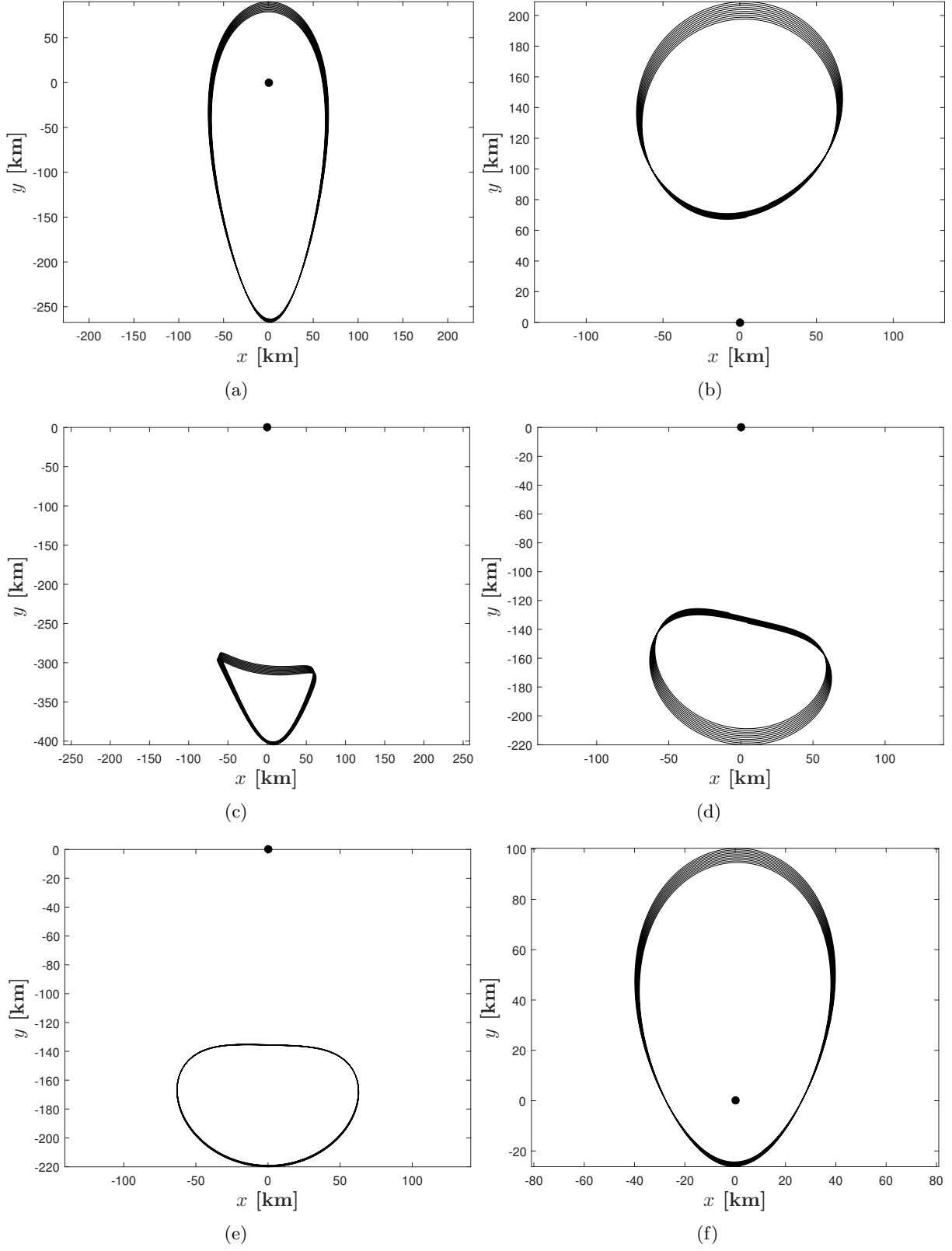
Figure 2.8: SRP Invariant Formation Design using First-Order Approximation Condition

2.6   Effects of Uncertainty in Attitude

Averaging theory is applied to determine the secular drifts in terms of the presence of a constant attitude error. This is mainly motivated by the fact that the solar sails are assumed to maintain a Sun-pointing attitude at all times for the purpose of precessing their orbit apse lines Sun-synchronously. Assuming that the sail's normal vector has an attitude error with respect to the nominal Sun-pointing attitude described by the two constant angles $\delta\alpha$ and $\delta\phi$, we have,

$$\phi = \phi_{\text{nom}} + \delta\phi = \pi - f + \delta\phi \tag{2.30a}$$

$$\alpha = \alpha_{\text{nom}} + \delta\alpha = \delta\alpha \tag{2.30b}$$

After substituting the new ϕ and α into Eq. (2.8) and substituting the result into the Gauss variational equations, we have,

$$\dot{a} = \frac{2a^2 k \cos\delta\alpha(\sin(f - \delta\phi) - e\sin\delta\phi)}{\sqrt{a\left(1 - e^2\right)\mu}} \tag{2.31a}$$

$$\dot{e} = \frac{k \cos\delta\alpha\sqrt{a\left(1 - e^2\right)\mu}(2\cos\delta\phi\sin f(e + \cos f) - \sin\delta\phi(4e\cos f + \cos 2f + 3))}{2\mu(1 + e\cos f)} \tag{2.31b}$$

$$\dot{i} = -\frac{k \sin\delta\alpha\sqrt{a\left(1 - e^2\right)\mu}\cos(f + \omega)}{\mu(1 + e\cos f)} \tag{2.31c}$$

$$\dot{\Omega} = -\frac{k \sin\delta\alpha\csc i\sqrt{a\left(1 - e^2\right)\mu}\sin(f + \omega)}{\mu(1 + e\cos f)} \tag{2.31d}$$

$$\dot{\omega} = \frac{k \cos\delta\alpha\sqrt{a\left(1 - e^2\right)\mu}(\cos\delta\phi(2e\cos f - \cos 2f + 3) - \sin\delta\phi\sin 2f)}{2e\mu(1 + e\cos f)} - \dot{\Omega}\cos i \tag{2.31e}$$

$$\dot{M} = n + \frac{k\left(a^2\left(1 - e^2\right)\right)^{3/2}\cos\delta\alpha(\cos\delta\phi(2e\cos f + \cos 2f - 3) + 2\sin\delta\phi\sin f(2e + \cos f))}{2a^2 e\sqrt{a\left(1 - e^2\right)\mu}(1 + e\cos f)} \tag{2.31f}$$

To remove the short-period variations, the osculating orbital elements in Eq. (2.31) are averaged with respect to mean anomaly using,

$$\dot{\bar{a}} = \frac{1}{2\pi} \int_0^{2\pi} \dot{a} \, dM \tag{2.32a}$$

$$\dot{\bar{e}} = \frac{1}{2\pi} \int_0^{2\pi} \dot{e} \, dM \tag{2.32b}$$

$$\dot{\bar{i}} = \frac{1}{2\pi} \int_0^{2\pi} \dot{i} \, dM \tag{2.32c}$$

$$\dot{\bar{\Omega}} = \frac{1}{2\pi} \int_0^{2\pi} \dot{\Omega} \, dM \tag{2.32d}$$

$$\dot{\bar{\omega}} = \frac{1}{2\pi} \int_0^{2\pi} \dot{\omega} \, dM \tag{2.32e}$$

$$\dot{\bar{M}} = \frac{1}{2\pi} \int_0^{2\pi} \dot{M} \, dM \tag{2.32f}$$

Upon taking the integration and simplification, the average orbital element rates for a solar sail in Sun-synchronous orbits with a constant attitude error are determined to be,

$$\dot{\bar{a}} = 0 \tag{2.33a}$$

$$\dot{\bar{e}} = -\frac{3k\sqrt{\bar{a}\left(1 - \bar{e}^2\right)}}{2\sqrt{\mu}} \cos \delta\alpha \sin \delta\phi \tag{2.33b}$$

$$\dot{\bar{i}} = \frac{3\bar{e}k \cos \bar{\omega}}{2\sqrt{\frac{\mu(1-\bar{e}^2)}{\bar{a}}}} \sin \delta\alpha \tag{2.33c}$$

$$\dot{\bar{\Omega}} = \frac{3\bar{e}k \csc \bar{i} \sin \bar{\omega}}{2\sqrt{\frac{\mu(1-\bar{e}^2)}{\bar{a}}}} \sin \delta\alpha \tag{2.33d}$$

$$\dot{\bar{\omega}} = \frac{3k\sqrt{\bar{a}\left(1 - \bar{e}^2\right)}}{2\bar{e}\sqrt{\mu}} \cos \delta\alpha \cos \delta\phi - \frac{3\bar{e}k \cot \bar{i} \sin \bar{\omega}}{2\sqrt{\frac{\mu(1-\bar{e}^2)}{\bar{a}}}} \sin \delta\alpha \tag{2.33e}$$

$$\dot{\bar{M}} = \bar{n} - \frac{3\bar{a}^2\left(1 + \bar{e}^2\right)k}{2\bar{a}^{3/2}\bar{e}\sqrt{\mu}} \cos \delta\alpha \cos \delta\phi \tag{2.33f}$$

The main advantage of deriving the average orbital element rates is their elegant simplified form, which immediately reveals a great deal about the long-term dynamics of the system. Additionally, they are more computationally efficient than the full osculating equations of motion. To verify the validity of Eq. (2.33), these approximate analytic expressions are compared to the full osculating Gauss variational equations in Eq. (2.13) for $(\delta\phi, \delta\alpha) = (1°, 1°)$. As illustrated in Fig. 2.9, the averaged equations correctly predict the secular growth in the orbital elements resulting from the errors in the sail's Sun-pointing attitude.

Next, the averaged rates for the orbital elements in Eq. (2.33) are used to generate the contour plots in Fig. 2.10. These plots illustrate the net change in the orbital elements over an orbit due to constant errors in the sail's orientation. The net change in eccentricity over an orbit is shown in Fig. 2.10(a). As expected from Eq. (2.33b), the effects of the $\delta\phi$ attitude errors are dominant over the span of small $\delta\alpha$ values. Even for very small $\delta\phi$ values, the eccentricity experiences a change of approximately 0.0001. The net change in the orbit inclination is shown in Fig. 2.10(b). The variation in inclination is completely dominant by the out-of-plane variation in the sail's attitude $\delta\alpha$. Errors in the ϕ angle will only effect the inclination for substantially high $\delta\phi$ values. These effects creep in through the variations in the e and ω orbital elements as evident by Eq. (2.33c). Similar to inclination, Fig. 2.10(c) shows that the effects of out-of-plane angle $\delta\alpha$ are dominant over the in-plane angle $\delta\phi$ in changing the right ascension of the ascending node. As expected, the argument of perigee is affected more by the in-plane variation relative to the right ascension of the ascending node. Fig. 2.10(f) illustrates the net change in the longitude of orbit's perigee ($\varpi = \omega + \Omega$). Based on these figures, one can conclude that, uncorrected attitude errors can quickly lead to the divergence of the nominal orbit or cause secular growth in the relative geometry between two solar sails.

(a) Semi-Major Axis

(b) Eccentricity

(c) Inclination

(d) Right Ascention of Ascending Node

(e) Argument of Perigee

(f) Mean Anomaly
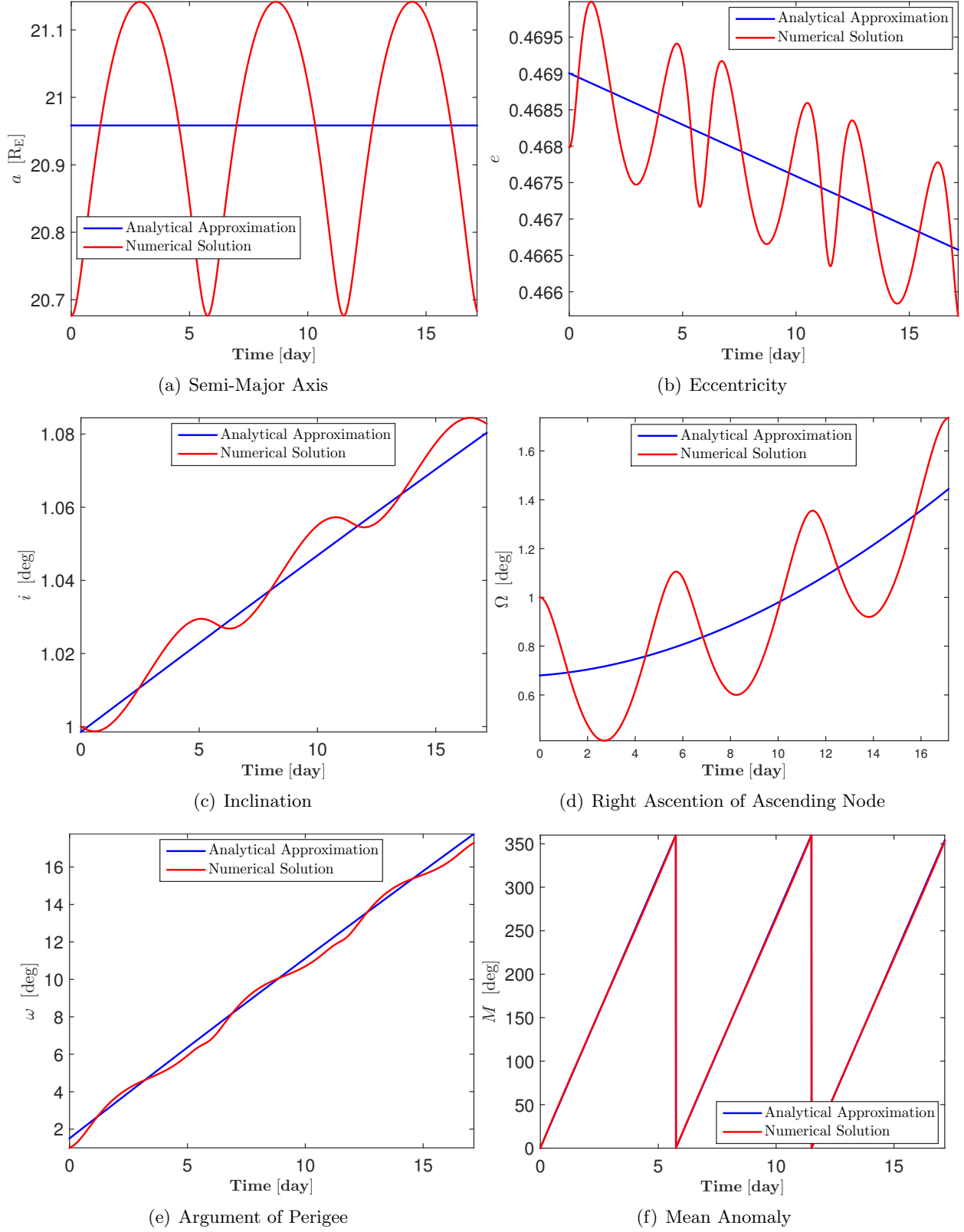
Figure 2.9: Verification of Averaged Orbital Element Rates Resulting from Changes in the Nominal Sun-Pointing Attitude

(a) Change in e Over an Orbit

(b) Change in i [deg] Over an Orbit

(c) Change in Ω [deg] Over an Orbit

(d) Change in ω [deg] Over an Orbit

(e) Change in M [deg] Over an Orbit

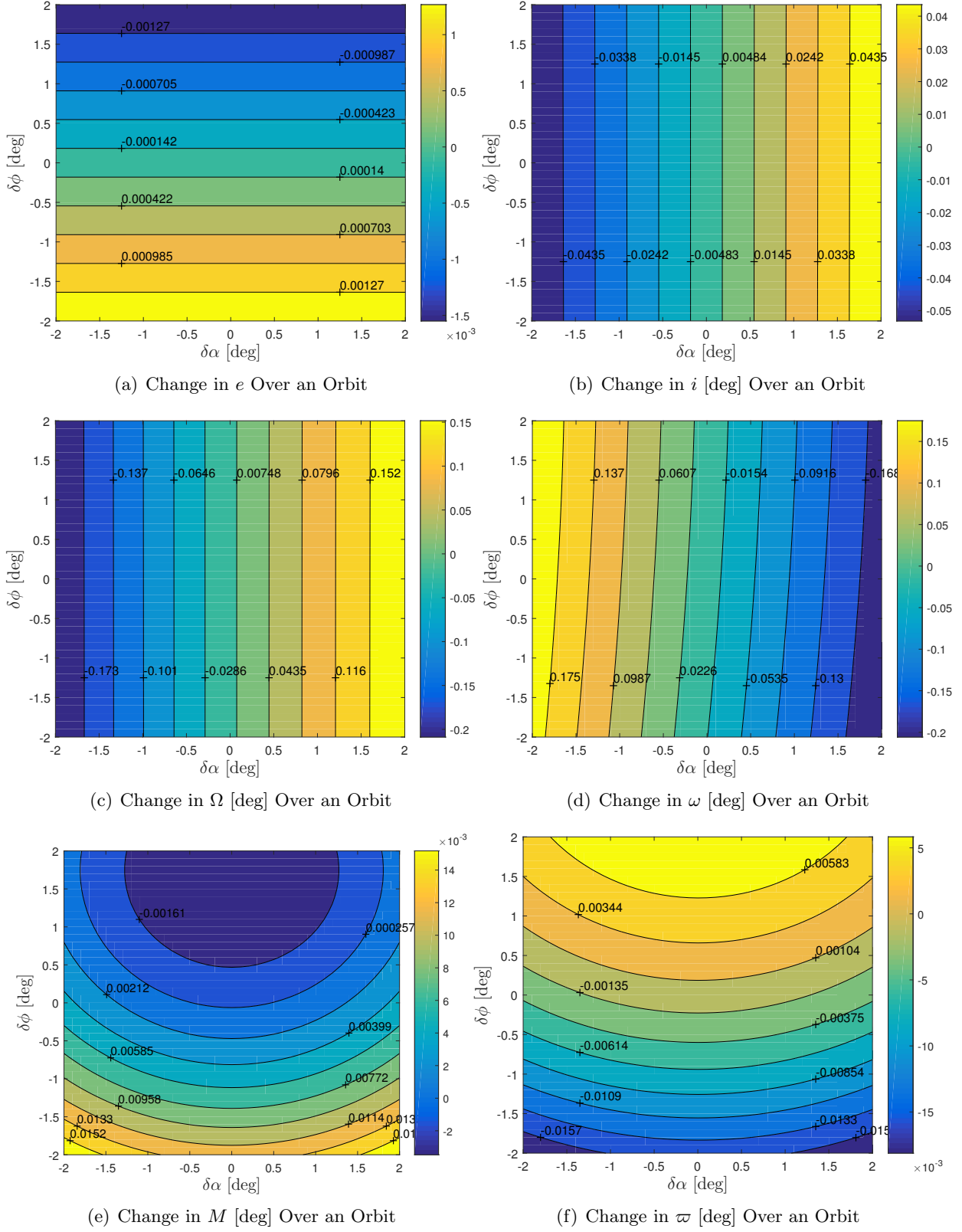(f) Change in ϖ [deg] Over an Orbit

Figure 2.10: Sensitivity of Orbital Elements to Constant Attitude Error

2.7   Effects of Uncertainty in Orbital Elements and Reflectivity

In this section, we evaluate the effects of errors in the orbital elements and reflectivity on the Sun-synchronous condition, which requires $\omega = \lambda_s$. The metric chosen is how much change ω experiences over an orbit given uncertainty in other orbital elements and reflectivity. To do this, the first variation of the rate of change in the argument of perigee $\delta\dot{\omega}(a, e, k)$, given in Eq. (2.23b), is used to determine the net change in argument of perigee over one orbit using $\Delta\bar{\omega} = T \times \delta\dot{\bar{\omega}}$, where T is the orbit period.

The contour plot shown in Fig. 2.11(a) illustrates the effects of uncertainty in the semi-major axis and eccentricity on the argument of perigee. The effects of unmodeled errors in characteristic acceleration and uncertainty in semi-major axis are shown in Fig. 2.11(b). Fig. 2.11(c) illustrates the change in argument of perigee due to errors in eccentricity and characteristic acceleration. As evident, the combined effects of uncertainties in eccentricity and characteristic acceleration can lead to changes in the argument of perigee as large as 0.1 degree over an orbit. Depending on the objective of the mission, this difference in argument of perigee may not be tolerable for the relative motion, especially for missions such as MMS, where the spacecraft are expected to maintain a tight formation of a certain size and shape. Fig. 2.12(a) illustrates the effects of uncertainty in the differential elements, namely the argument of perigee, on the relative motion geometry. As evident in the figure, an uncertainty in the argument of perigee of the size $\delta\omega = 0.05°$ significantly changes the shape of the nominal leader-follower formation, leading to about a 100 km error in the along-track (y) direction. Using Fig. 2.12(b), one can conclude that an uncertainty in reflectivity larger than 0.1% leads to significant changes in the size and shape of the formation, which may not satisfy the requirements for tight formations such as the one being flown in the MMS mission.
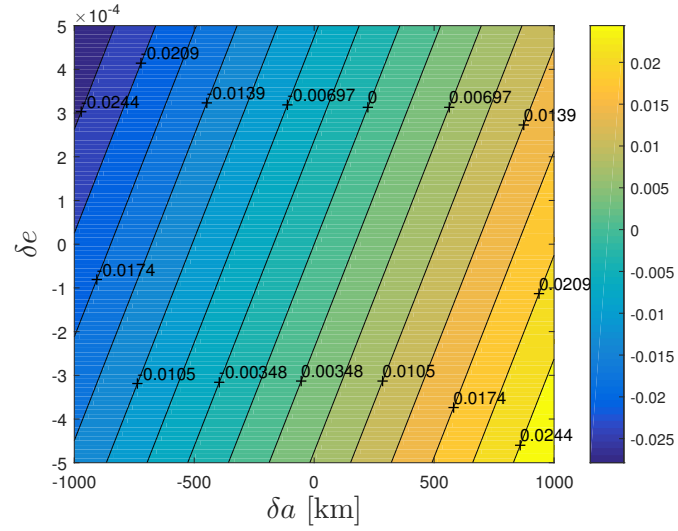
(a) Change in ω [deg] Over One Orbit due to Errors in a & e
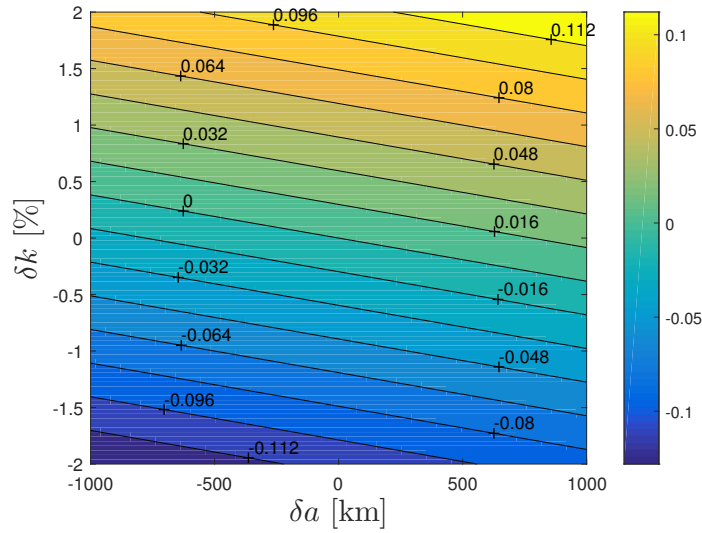
(b) Change in ω [deg] Over One Orbit due to Errors in a & k
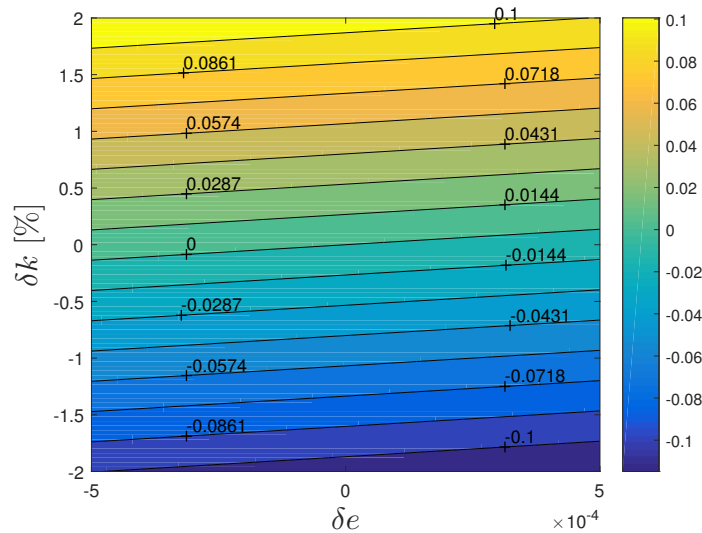
(c) Change in ω [deg] Over One Orbit due to Errors in e & k

Figure 2.11: Sensitivity of Argument of Perigee to Errors in Semi-Major Axis, Eccentricity, and the Sail's Characteristic Acceleration (Reflectivity)

(a) Relative Motion in Chief's LVLH Frame

(b) Change in ω [deg] Over One Orbit due to Errors in k
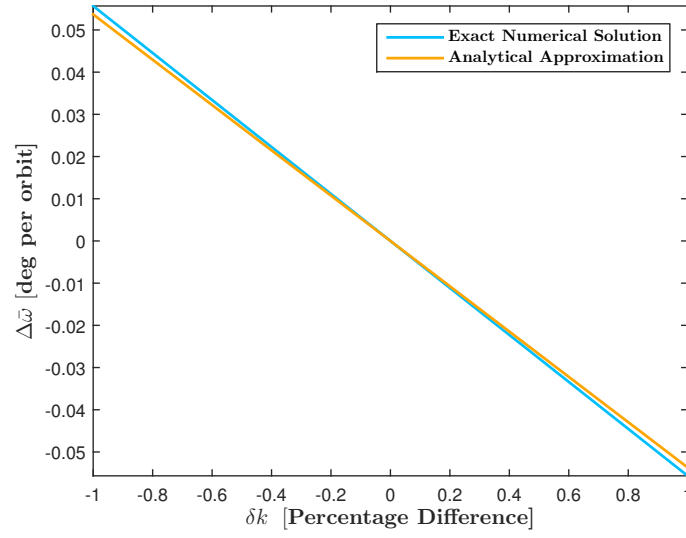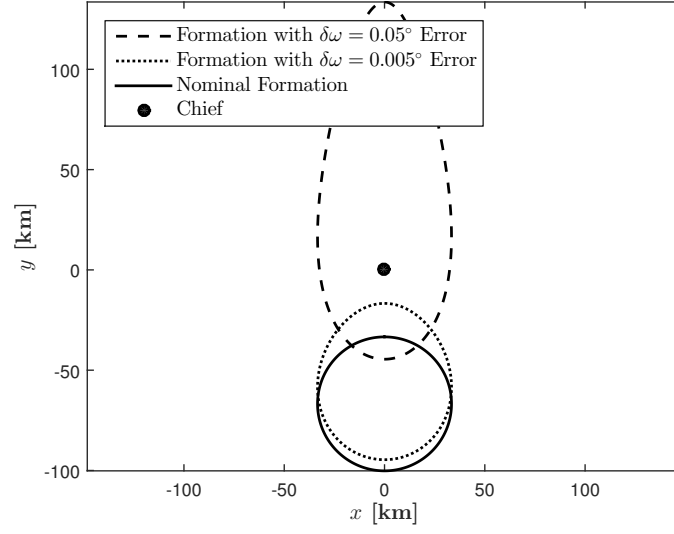
Figure 2.12: Effects of $\delta\omega$ Error on Leader-Follower Formation

Chapter 3

Solar Sail Formation Design in Sun-Synchronous Orbits

In Chapter 2, the necessary conditions for achieving SRP invariant solar sail formation flight in Sun-synchronous orbits were derived. The first-order necessary conditions lead to quasi-periodic relative motions that experience some relative drift due to the truncation in the higher order terms. In this chapter, numerical optimization techniques are employed to remove any relative drift arising from the first-order approximation. Employing numerical methods leads to the design of truly SRP invariant relative motions in Sun-synchronous orbits. The numerical algorithms are used to design two-craft, triangle, and tetrahedron solar sail formations. As mentioned in previous chapters, all sails are assumed to maintain a Sun-pointing attitude to precess their orbit apse line Sun-synchronously upon achieving the desired relative states. The employment of numerical optimization to remove the relative drifts between solar sails has two advantages over the method proposed in Chapter 2:

- It allows the design variables to be *osculating elements*, thereby side stepping averaged-osculating mapping that can potentially introduce errors into the design of a drift-free formation.

- It allows for the inclusion of other perturbations in the design of a formation. Because of the high altitudes of orbits required to study the geomagnetic tail, it is critical to include the third-body effects of the Moon and Sun in the formation design problem.

Next, the problem formulation is discussed in detail. The formation design problem is then solved numerically using nonlinear programming techniques. MATLAB's constrained nonlinear optimization routine, *fmincon* with *active set* algorithm, is employed to solve the optimization problem. The formation design problem may be summarized as follows:

Formation Design Problem Statement

Given: chief's osculating elements $\boldsymbol{œ}_{c_0} = \begin{bmatrix} a_{c_0} & e_{c_0} & \omega_{c_0} & M_{c_0} \end{bmatrix}^T$ at epoch t_0

Determine: deputy's osculating elements $\boldsymbol{œ}_{d_0} = \begin{bmatrix} a_{d_0} & e_{d_0} & \omega_{d_0} & M_{d_0} \end{bmatrix}^T$ at epoch t_0 such that the relative motion is SRP invariant

---

3.1   SRP Invariant Solar Sail Formations

Let l denote the sail's mean longitude, defined as,

$$l = \omega + M \tag{3.1}$$

The total relative change in mean longitude over an arbitrary number of complete revolutions is defined as,

$$\Delta l = \int_{t_0}^{t_f} \left(\dot{l}_d(t) - \dot{l}_c(t) \right) \mathrm{d}t \tag{3.2}$$

The variable Δl indicates how much the deputy has drifted apart with respect to the chief over a given time span. Given the chief's osculating elements $\boldsymbol{œ}_{c_0}$, a two-craft formation design algorithm is proposed as follows,

$$
\begin{aligned}
\text{minimize} \quad & J = |\Delta l| \\[2mm]
\text{with respect to} \quad & a_{d_0}, e_{d_0} \\[2mm]
\text{subject to} \quad & \ddot{\boldsymbol{r}}_c = -\frac{\mu}{r_c^3}\boldsymbol{r}_c + \boldsymbol{a}_{s_c} \\[2mm]
& \ddot{\boldsymbol{r}}_d = -\frac{\mu}{r_d^3}\boldsymbol{r}_d + \boldsymbol{a}_{s_d} \\[2mm]
\text{free variables} \quad & k_d, M_{d_0}, \omega_{d_0}
\end{aligned}
\tag{3.3}
$$

In this formulation, it is assumed that the free variable is the deputy's characteristic acceleration k_d while the a_{d_0} and e_{d_0} osculating elements are left to be determined numerically, such that the relative motion is SRP invariant. The algorithm allows for the minimization of the relative drift between the two sails through a search of the osculating element space. The minimization of total relative change in mean longitude over a specific time span is equivalent to matching the average longitude rates. The first-order SRP invariant relative motion conditions using osculating elements are used to provide an initial guess for the deputy's elements, since nonlinear programming problems require an initial guess to solve the problem. The problem formulation in Eq. (3.3) can be modified to have either the semi-major axis or eccentricity as a free variable rather than the characteristic acceleration. Hence, the formulation may be equivalently rewritten as

$$
\begin{aligned}
\text{minimize} \quad & J = |\Delta l| \\
\text{with respect to} \quad & e_{d_0}, k_d \\
\text{subject to} \quad & \ddot{\boldsymbol{r}}_c = -\frac{\mu}{r_c^3}\boldsymbol{r}_c + \boldsymbol{a}_{s_c} \\
& \ddot{\boldsymbol{r}}_d = -\frac{\mu}{r_d^3}\boldsymbol{r}_d + \boldsymbol{a}_{s_d} \\
\text{free variables} \quad & a_{d_0}, M_{d_0}, \omega_{d_0}
\end{aligned}
\tag{3.4}
$$

In Eq. (3.4), the free variable is chosen to be the deputy's semi-major axis a_{d_0} while the algorithm searches for the corresponding e_{d_0} and k_d that leads to an SRP invariant relative motion. The deputy's mean anomaly M_{d_0} and ω_{d_0} are the other free variables that can be tweaked to control the differential elements δM and $\delta \omega$ for designing formation geometries of different size and shape. Although ω_{d_0} is a free variable, there are lower and upper bounds for how much ω_{d_0} can change with respect to the Sun's longitude angle λ_s. This is due to the Sun-synchronous condition that each sail must satisfy. Therefore, the deputy's ω_{d_0} must remain close to the Sun's longitude angle λ_s.

An example of the algorithm proposed in Eq. (3.4) is illustrated in Fig. 3.1. A family of SRP invariant relative orbits are illustrated in Fig. 3.1(a). In these examples, the deputy's semi-major axis is varied such that $0 \leq \delta a_0 \leq 1$ km, while keeping δM_0 constant. In Fig. 3.1(b),

the δM_0 is varied while keeping δa_0 constant. For both simulations, it is assumed that $\delta \omega_0 = 0$ ($\omega_{d_0} = \omega_{c_0} = \lambda_{s_0}$). Each trajectory is propagated for 10 orbits. As evident in both Fig. 3.1(a) and Fig. 3.1(b), the relative motion does not experience any relative drift, unlike the secular drifts that arise in Fig. 2.8 due to the first-order approximation of the SRP invariant relative orbit conditions.
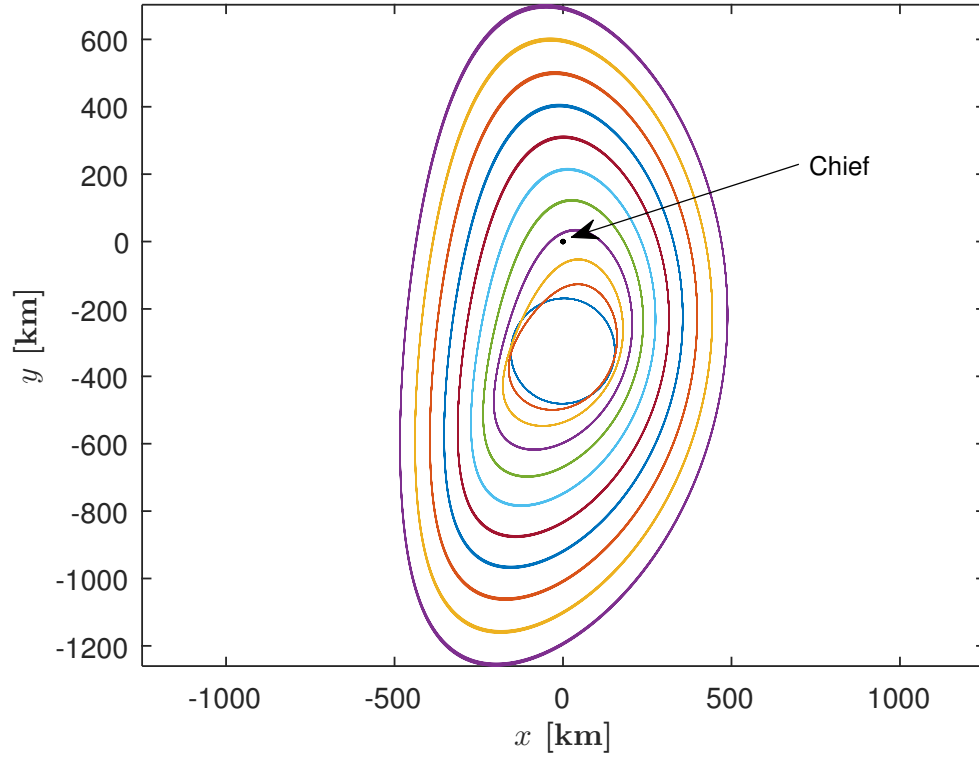
(a) Varying a_{d_0} while keeping M_{d_0} constant
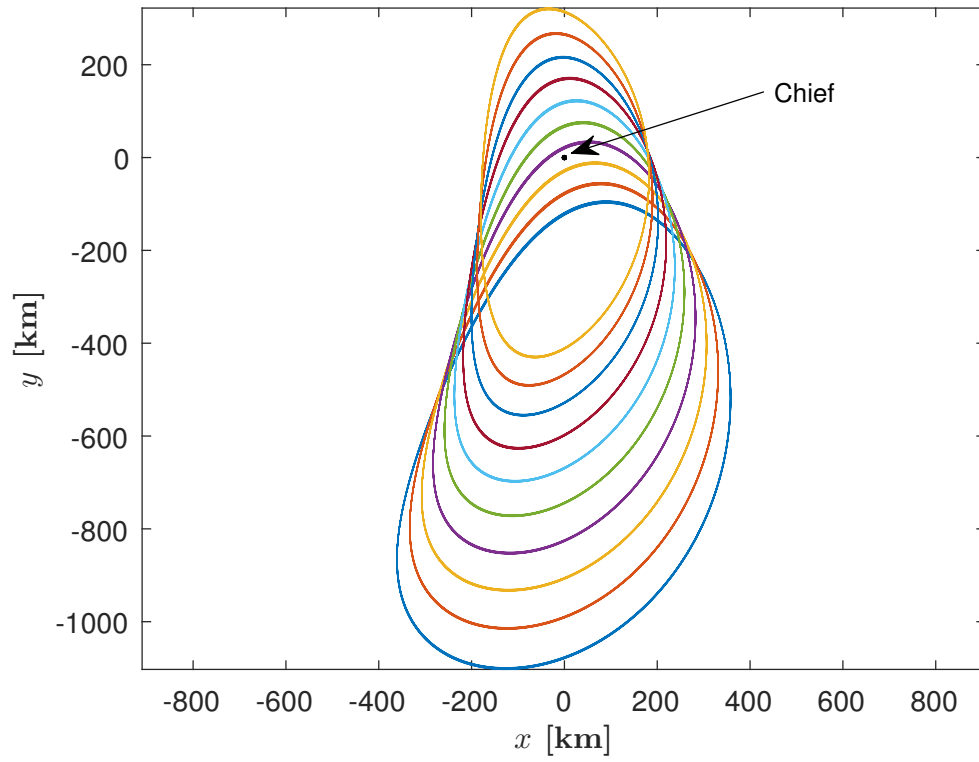
(b) Varying M_{d_0} while keeping a_{d_0} constant

Figure 3.1: Deputies' Relative Motion in Chief's LVLH Frame

3.2   Solar Sail Formation Design in a Specified Region of Interest

The science region of interest (RoI) for exploring the geomagnetic tail is shown in Fig. 3.2. In this thesis, the region of interest is defined as all portions of the chief's orbit with radius above 21 R_E. The objective is to design formations that achieve their desired size and shape within this specified region of interest around apogee. Depending on the number of solar sails in formation, a different metric is defined to evaluate the quality of formation in terms of size and shape for two-craft, three-craft, and four-craft formations.

3.2.1   Two-Craft Formation

For the two-craft formation, the average inter-spacecraft range within the RoI is defined as the metric for evaluating the quality of a formation. The relative position vector between two solar sails at any point in time is written as,

$$s(t) = \boldsymbol{r}_d(t) - \boldsymbol{r}_c(t) \tag{3.5}$$

The average distance between the two solar sails within the RoI is defined as,

$$\bar{\rho} = \frac{1}{N} \sum_{k=1}^{N} \rho_k \tag{3.6}$$

where $\rho_k = ||\boldsymbol{s}_k||$ and N is the number of integration steps within the RoI. The algorithm defined in Eq. (3.4) is modified as follows to design a two-craft formation of a particular size within the
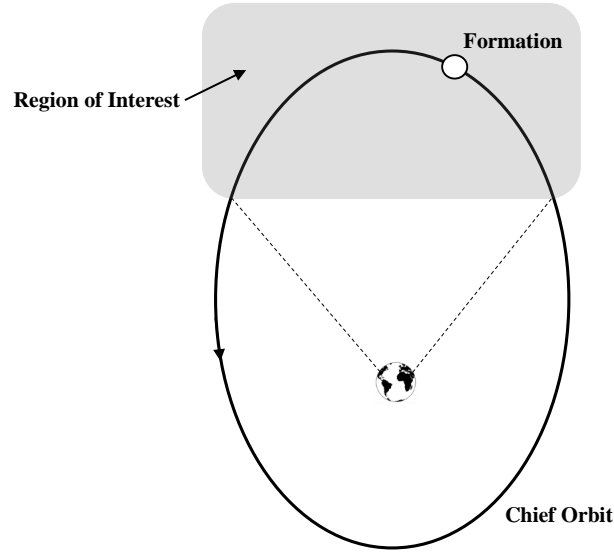
Figure 3.2: Solar Sail Formation in a Region of Interest around Apogee

science region of interest,

$$
\begin{aligned}
\text{minimize} \quad & J = |\Delta l| \\
\text{with respect to} \quad & e_{d_0}, k_d, M_{d_0} \\
\text{subject to} \quad & \ddot{\boldsymbol{r}}_c = -\frac{\mu}{r_c^3}\boldsymbol{r}_c + \boldsymbol{a}_{s_c} \\
& \ddot{\boldsymbol{r}}_d = -\frac{\mu}{r_d^3}\boldsymbol{r}_d + \boldsymbol{a}_{s_d} \\
& \bar{\rho}_{\min} \leq \bar{\rho} \leq \bar{\rho}_{\max} \\
\text{free variables} \quad & a_{d_0}, \omega_{d_0}
\end{aligned}
\tag{3.7}
$$

Examples of the two-craft formation designed to maximize the science gain in the RoI are shown in Fig. 3.3 for the various formation sizes of 30, 180, and 300 km, in terms of average separation distance. The highlighted region represents the time that the formation is flying within the RoI.
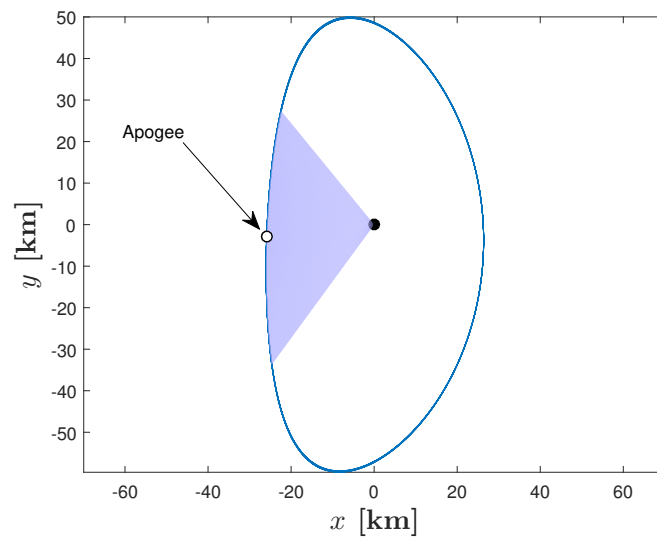
(a) 30 km Formation
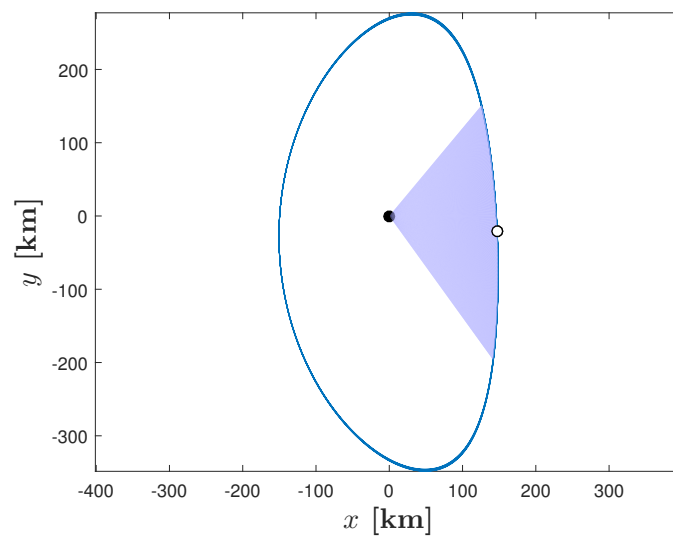
(b) 180 km formation
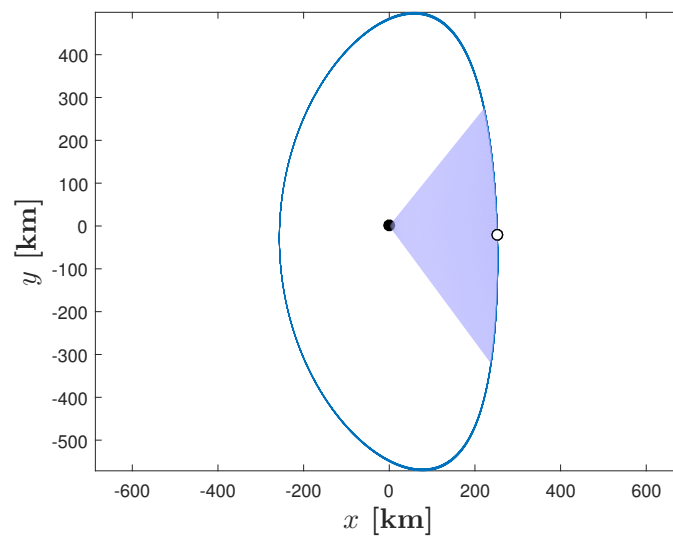
(c) 300 km Formation

Figure 3.3: Deputies' Relative Motion in Chief's LVLH Frame

3.2.2   Triangle Formation

In this section, the desired three-craft formation geometry to be designed inside the RoI is a breathing in-plane equilateral triangle. For this simple formation geometry, a preliminary formation is designed analytically. This preliminary formation is then used as an initial guess for the numerical algorithm to design a triangle inside the RoI. The initial step in designing a formation is to define a metric that measures the *quality* of formation. For the MMS mission, it is desired that the formation remains close to a regular tetrahedron as long as possible within the RoI. MMS uses an instantaneous metric called Quality Factor (Q) which measures both shape (Q_v) and size (Q_s) of tetrahedron formation with respect to a regular tetrahedron at any given time [27, 25, 26, 35]. This formation quality metric is adapted in this thesis to design triangle and tetrahedron formations. The use of the formation quality factor Q allows direct comparison to be made between the results in this thesis and formations designed for the MMS mission. For a triangle formation, the quality factor is defined using,

$$Q(t) = Q_a(t) \times Q_s(t) \tag{3.8}$$

In order to define Q_a and Q_s explicitly, the following parameters need to be introduced. Each side of the triangle formation at any given time, $\boldsymbol{s}_j$, is defined as,

$$\boldsymbol{s}_1 = \boldsymbol{r}_{d_1} - \boldsymbol{r}_c$$
$$\boldsymbol{s}_2 = \boldsymbol{r}_{d_2} - \boldsymbol{r}_c \tag{3.9}$$
$$\boldsymbol{s}_3 = \boldsymbol{r}_{d_1} - \boldsymbol{r}_{d_2}$$

where $\boldsymbol{r}_c$, $\boldsymbol{r}_{d_1}$, $\boldsymbol{r}_{d_2}$ are the position vectors of chief, first deputy, and second deputy respectively. The area of the triangle formation is defined at any epoch via,

$$A(t) = \frac{1}{2}|\boldsymbol{s}_1 \times \boldsymbol{s}_2| \tag{3.10}$$

Given the inter-spacecraft range of $\rho_j = \|\boldsymbol{s}_j\|$, the average side-length for triangle formation is determined by

$$\bar{L} = \frac{1}{3} \sum_{j=1}^{3} \rho_j \tag{3.11}$$

The area of an equilateral triangle with an average side-length of $\bar{L}$ is,

$$A_r = \frac{\sqrt{3}}{4} \bar{L}^2 \tag{3.12}$$

The instantaneous metric $Q_a(t)$ for evaluating the shape of a triangle formation is defined as the ratio of the actual triangle area to the area of an equilateral triangle with averaged side-length of $\bar{L}$,

$$Q_a(t) = \frac{A}{A_r} \tag{3.13}$$

The size metric, Q_s, is a smooth piecewise function defined as,

$$Q_s(\bar{L}) = \begin{cases} 0 & \bar{L} < l_1 \\ \frac{\left(\bar{L}-l_1\right)^2 \left(\bar{L}+l_1-2l_2\right)}{(l_2-l_1)^4} & l_1 \le \bar{L} \le l_2 \\ 1 & l_2 < \bar{L} \le l_3 \\ \frac{\left(\bar{L}-l_4\right)^2 \left(\bar{L}+l_4-2l_3\right)}{(l_4-l_3)^4} & l_3 < \bar{L} \le l_4 \\ 0 & \bar{L} > l_4 \end{cases} \tag{3.14}$$

where, $l_1, \cdots, l_4$ are constants that are chosen for every formation size in order to define the acceptable size range. The average value of the metric Q within the RoI at N number of integration steps is

$$\bar{Q}_{\text{RoI}} = \frac{1}{N} \sum_{k=1}^{N} Q_k \tag{3.15}$$

The average quality factor, $\bar{Q}_{\text{RoI}}$, must be maximized for a triangle formation to remain as close to an equilateral triangle within the RoI. Thus, the cost function is chosen to be,

$$J = \bar{Q}_{\text{RoI}} \tag{3.16}$$

Having defined the cost function, the triangle formation design problem may be formulated as,

$$\text{minimize} \quad J = -\sum_{n=1}^{N_{\text{orb}}} J_n$$

$$\text{with respect to} \quad \Delta \text{œ}_0 = \begin{bmatrix} \Delta a_{j_0} & \Delta e_{j_0} & \Delta \omega_{j_0} & \Delta M_{j_0} \end{bmatrix}^T$$

$$\text{subject to} \quad \ddot{\boldsymbol{r}} = -\frac{\mu}{r^3}\boldsymbol{r} + \boldsymbol{a}_s \tag{3.17}$$

$$\Delta i_{j_0} = 0, \Delta \Omega_{j_0} = 0$$

$$k_j = \frac{2}{3}\dot{\lambda}_s \frac{e_j}{\sqrt{1-e_j^2}}\sqrt{\frac{\mu}{a_j}}$$

where N_{orb} is the number of orbits that the average quality factor within the RoI is optimized over. Enforcing the characteristic acceleration value assures that each orbit remains Sun-synchronous.

To solve the NLP problem, a crude initial guess is designed analytically. This initial guess is a perfect equilateral triangle at the chief's apogee. This *instantaneous* equilateral triangle is illustrated in Fig. 3.4. Given the chief's apogee radius of $\boldsymbol{r}_{a_c}$, deputies' apogee radius are determined using,

$$\boldsymbol{r}_{a_j} = \boldsymbol{r}_{a_c} + \boldsymbol{L}_j \tag{3.18}$$

where $^{\mathcal{T}}\boldsymbol{L}_j$ are the triangle sides expressed in a local frame $\mathcal{T} = \begin{bmatrix} \hat{\boldsymbol{t}}_1 & \hat{\boldsymbol{t}}_2 & \hat{\boldsymbol{t}}_3 \end{bmatrix}$ that has its origin at the chief's position,

$$^{\mathcal{T}}\boldsymbol{L}_1 = \begin{bmatrix} \frac{1}{2}L & \frac{\sqrt{3}}{2}L & 0 \end{bmatrix}^T \tag{3.19a}$$

$$^{\mathcal{T}}\boldsymbol{L}_2 = \begin{bmatrix} -\frac{1}{2}L & \frac{\sqrt{3}}{2}L & 0 \end{bmatrix}^T \tag{3.19b}$$

The triangle frame $\mathcal{T}$ is defined with respect to the LVLH frame $\mathcal{O}$ via,

$$[\mathcal{OT}] = [\boldsymbol{C}_1(\theta_1)][\boldsymbol{C}_2(\theta_2)][\boldsymbol{C}_3(\theta_3)] \tag{3.20}$$

For this initial guess, it is assumed that all solar sails have the same osculating semi-major axis at this instant and that they are all at their orbit apogee. Thus, the perigee radius for each spacecraft is computed by $r_{p_j} = 2a_c - r_{a_j}$ where $r_{a_j} = ||\boldsymbol{r}_{a_j}||$. The deputies' eccentricities are determined
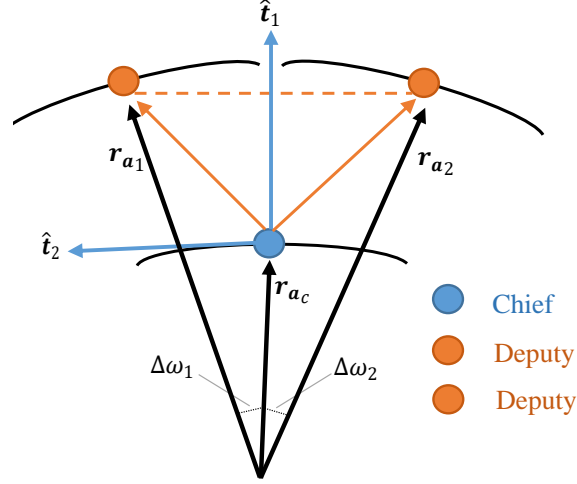
Figure 3.4: Instantaneous Equilateral Triangle at Chief's Apogee

Table 3.1: Initial Guess for Triangle Orbital Elements

Chief	Deputy 1	Deputy 2
a_c	a_c	a_c
e_c	$\frac{r_{a_1}-r_{p_1}}{2a_c}$	$\frac{r_{a_2}-r_{p_2}}{2a_c}$
i_c	i_c	i_c
Ω_c	Ω_c	Ω_c
ω_c	$\omega_c + \Delta\omega$	$\omega_c - \Delta\omega$
$f_c = \pi$	f_c	f_c

using their apogee and perigee radii. Because the formation's geometry of interest is an in-plane triangle, the deputies' inclinations and right ascension of ascending nodes are identical to those of the chief. The argument of perigee for each deputy is determined using,

$$\omega_{d_1} = \omega_c + \Delta\omega \qquad (3.21\text{a})$$

$$\omega_{d_2} = \omega_c - \Delta\omega \qquad (3.21\text{b})$$

where the differential element $\Delta\omega$ is,

$$\Delta\omega = \cos^{-1}\left(\frac{\boldsymbol{r}_{a_j} \cdot \boldsymbol{r}_{a_c}}{r_{a_j} r_{a_c}}\right) \qquad (3.22)$$

The orbital elements for each spacecraft in this crude initial guess is summarized in Table 3.1. To determine the quality and stability of this formation, the formation is propagated for approximately

15 orbits. As evident in Fig. 3.5(a), the formation forms a perfect equilateral triangle at the orbit apogee but is immediately deformed after apogee, as is also shown by the sharp decrease in the formation quality factor Q. The average quality factor is approximately $\bar{Q} = 0.61$. This is far below the limit acceptable for a formation that is useful for collecting science data, but serves as an adequate initial guess for the numerical optimizer. The relative motion as seen by the chief's LVLH frame is illustrated in Fig. 3.5(b). The time history of inter-spacecraft ranges are shown in Fig. 3.5(c). There are no dangerous close approaches throughout the entire simulation.
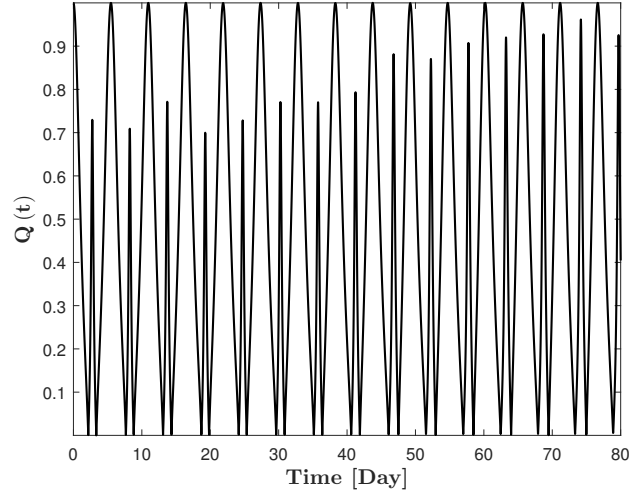
(a) Formation Quality Factor
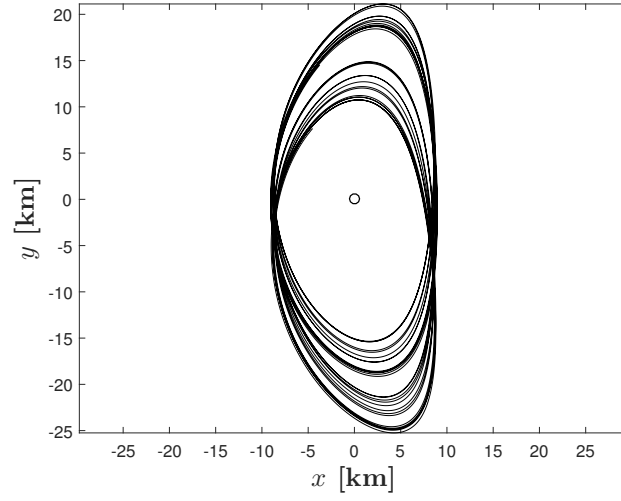
(b) Deputies' Relative Motion in Chief's LVLH Frame
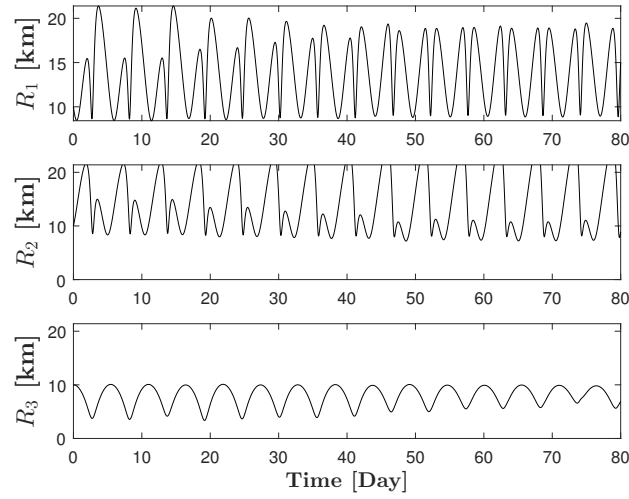
(c) Inter-Spacecraft Range

Figure 3.5: Initial Guess for In-Plane Equilateral Triangle Formation Design

The algorithm described in Eq. (3.17) is utilized to design in-plane equilateral triangle formations with various sizes. The selected formation sizes in terms of average side-lengths are 10, 60, 160, 400 km. The chosen formation sizes are directly motivated by the formation sizes that are used in the MMS mission. Fig. 3.6 illustrates the optimized solution for the 10 km triangle formation. As illustrated in Fig. 3.6(a), the quality factor remains acceptable for at least 60 days. The minimum spacecraft range is around 10 km, indicating a safe formation for the entire simulation. Because the eccentricity of the optimized orbits are different, it requires each solar sail to have a slightly different characteristic accelerations according to the Sun-synchronous condition. For this formation, the required change in reflectivity is less than 0.02% for both deputies. Fig. 3.7-3.9 show the optimized solutions for the 60, 160, and 400 km formations, respectively. Similar to the 10 km formation, the designed formations are stable for at least 60 days and do not experience any dangerous close approaches. The optimized initial conditions for 10, 160, 400 km formation sizes are given in Table. B.1, Table. B.2, and Table. B.3, respectively.

In all formations designed, there is a slow secular drift that leads to a slow degradation of the formation quality. The main reason for this apparent relative drift is the absense of enforcing the relative SRP invariant condition. As it can be seen from Eq. (3.17), the objective is to maximize the quality of the formation and there is no enforced constraint that involves minimizing the relative drifts between the solar sails. The inclusion of the relative SRP invariant condition is discussed in Section 3.3.
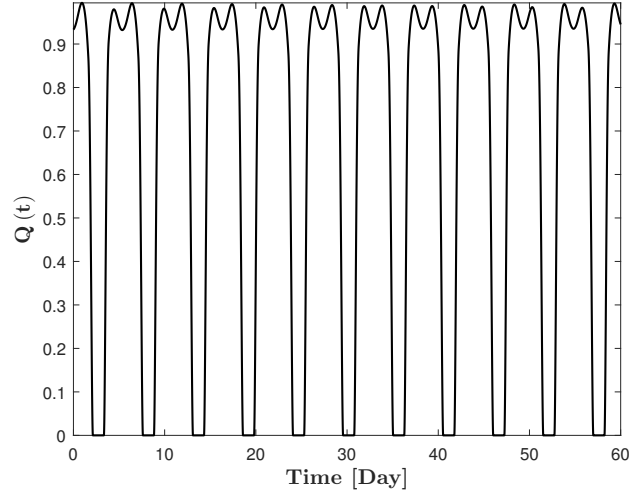
(a) Formation Quality Factor

(b) Deputies' Relative Motion in Chief's LVLH Frame
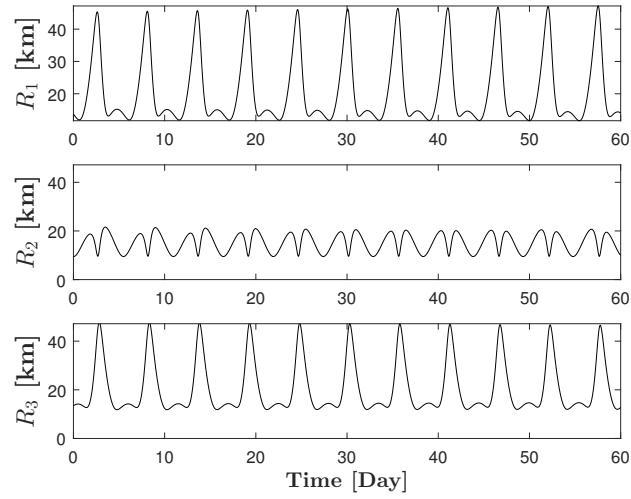
(c) Inter-Spacecraft Range

Figure 3.6: In-Plane Equilateral Triangle Formation with Average Side-Length of 10 km
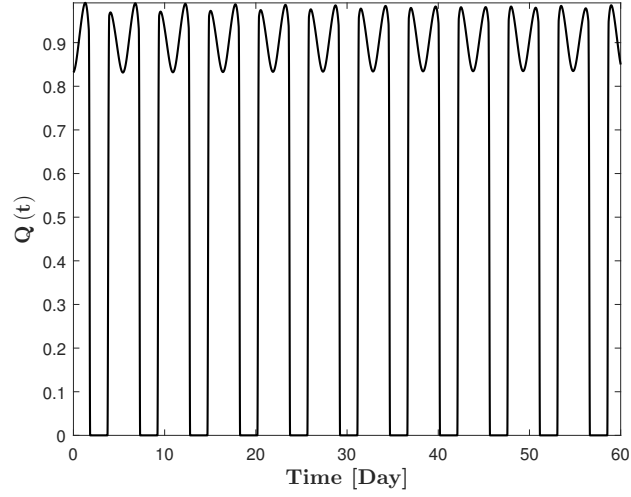
(a) Formation Quality Factor
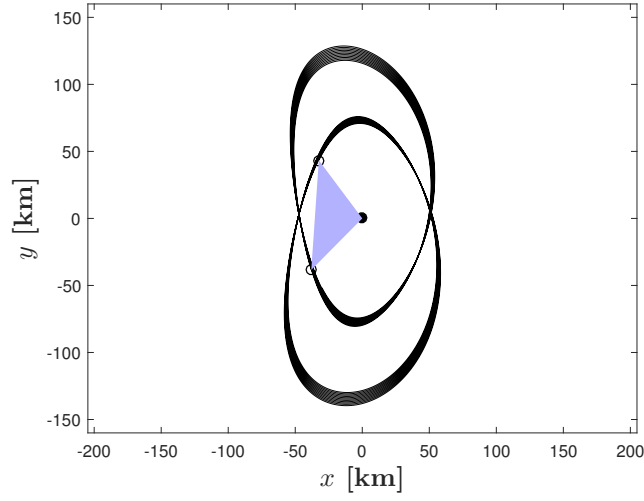
(b) Deputies' Relative Motion in Chief's LVLH Frame
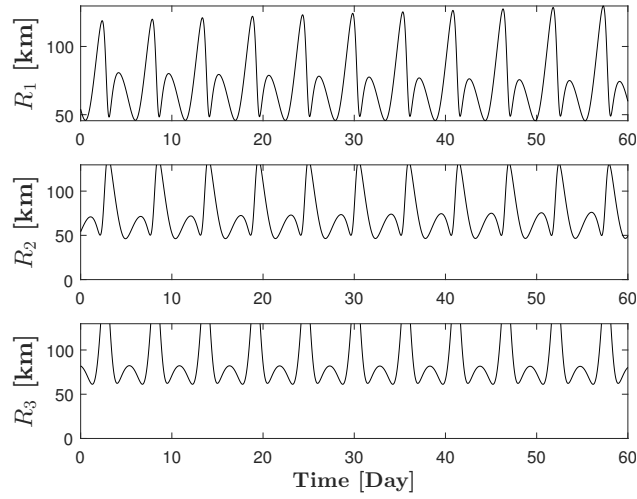
(c) Inter-Spacecraft Range

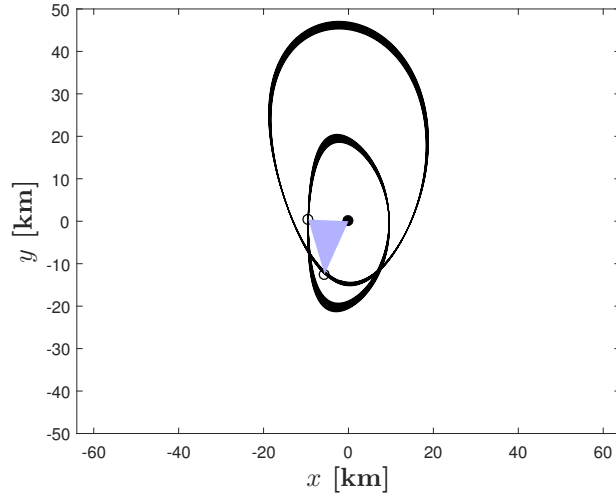Figure 3.7: In-Plane Equilateral Triangle Formation with Average Side-Length of 60 km
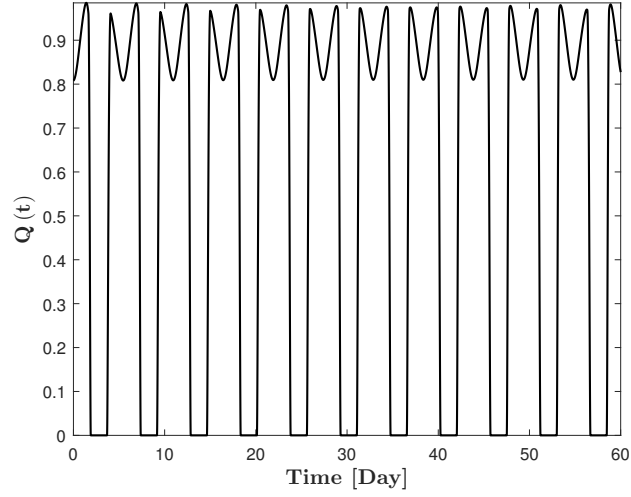
(a) Formation Quality Factor
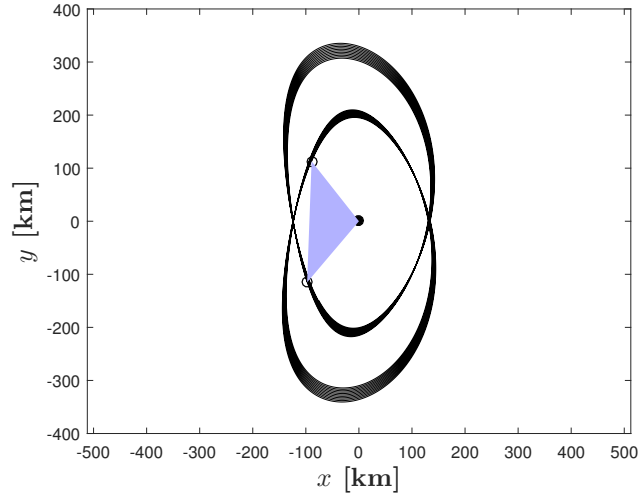
(b) Deputies' Relative Motion in Chief's LVLH Frame
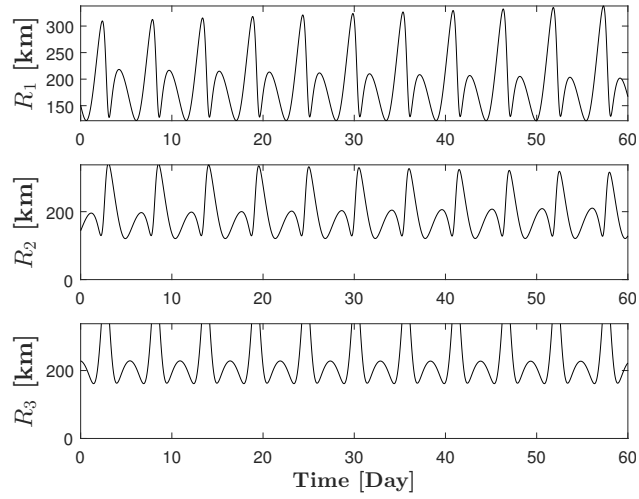
(c) Inter-Spacecraft Range

Figure 3.8: In-Plane Equilateral Triangle Formation with Average Side-Length of 160 km
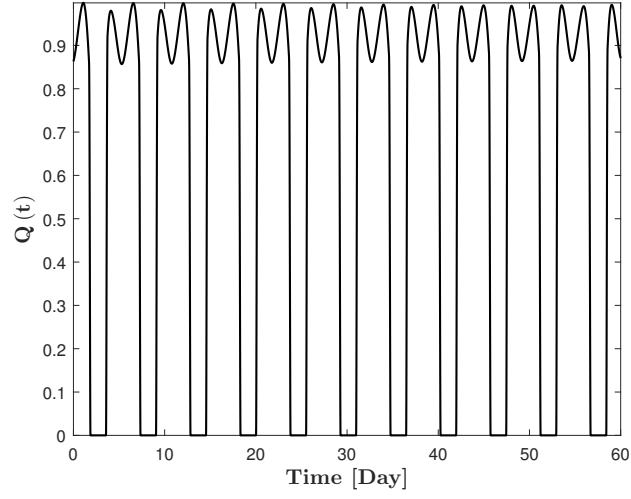
(a) Formation Quality Factor
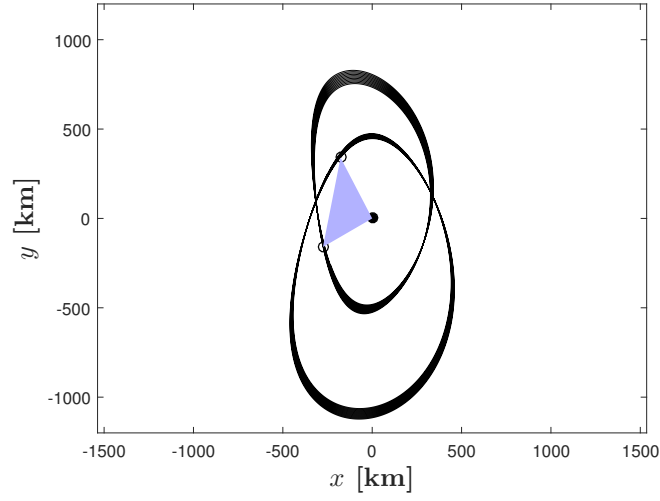
(b) Deputies' Relative Motion in Chief's LVLH Frame
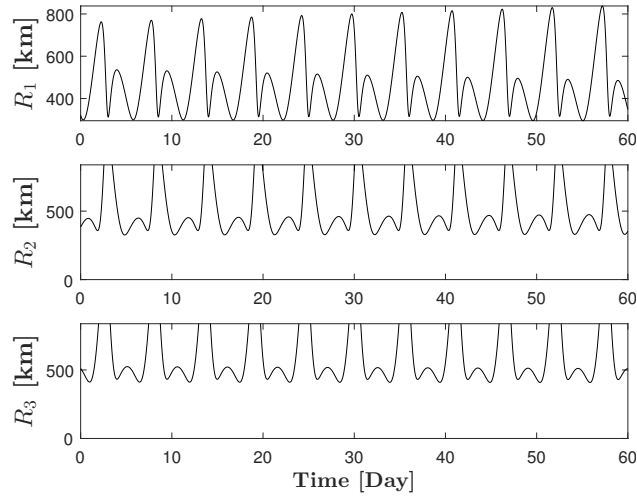
(c) Inter-Spacecraft Range

Figure 3.9: In-Plane Equilateral Triangle Formation with Average Side-Length of 400 km

3.2.3   Tetrahedron Formation

The minimum number of spacecraft to study the spatial and temporal changes of magnetic reconnection in three-dimensions is four. This section investigates the possibility flying four solar sails that form a tetrahedron within the RoI. The formation design problem is analogous to the triangle formation, with a modification in the cost function. For the shape metric, the volume metric, Q_v, is used as opposed to the area metric Q_a in the triangle formation design problem. Therefore, for the tetrahedron formation design, the instantaneous quality factor $Q(t)$ is defined as,

$$Q(t) = Q_v(t) \times Q_s(t) \tag{3.23}$$

The *actual* volume of tetrahedron formation at any given time is governed by

$$V(t) = \frac{1}{6} |\boldsymbol{s}_1 \cdot (\boldsymbol{s}_2 \times \boldsymbol{s}_3)| \tag{3.24}$$

The volume of a regular tetrahedron that has the same average side length of $\bar{L}$ is calculated through

$$V_r = \frac{\sqrt{2}}{12} \bar{L}^3 \tag{3.25}$$

The volume metric is defined as the ratio of the actual tetrahedron volume, V_a, to the volume of a regular tetrahedron V_r.

$$Q_v(t) = \frac{V}{V_r} \tag{3.26}$$

Both Q_v and Q_s have a range that falls between 0 and 1. Q_v will equal 1 when the volume of the tetrahedron equals that of a regular tetrahedron and it will be equal to 0 when all four spacecraft lie in a plane. Q_s will equal 1 when the formation falls within the desired size range and 0 when it is outside of the acceptable range. The NLP problem of designing tetrahedron solar sail formation may be written as,

(a) 10 km Formation   (b) 400 km Formation
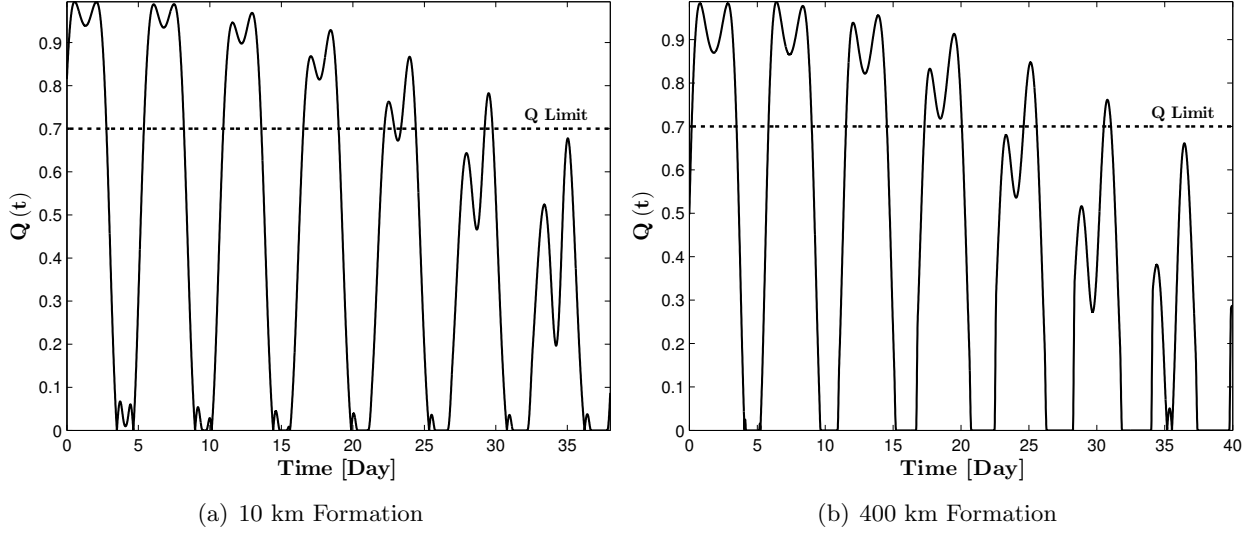
Figure 3.10: 1-Orbit Optimized Tetrahedron Formation

$$\text{minimize} \quad J = \sum_{n=1}^{N_{orb}} J_n$$

$$\text{with respect to} \quad \Delta \boldsymbol{œ}_0 = \begin{bmatrix} \Delta a_{j_0} & \Delta e_{j_0} & \Delta i_{j_0} & \Delta \Omega_{j_0} & \Delta \omega_{j_0} & \Delta M_{j_0} \end{bmatrix}^T \qquad (3.27)$$

$$\text{subject to} \quad \ddot{\boldsymbol{r}} = -\frac{\mu}{r^3}\boldsymbol{r} + \boldsymbol{a}_s$$

$$k_j = \frac{2}{3}\dot{\lambda}_s \frac{e_j}{\sqrt{1 - e_j^2}}\sqrt{\frac{\mu}{a_j}}$$

A regular tetrahedron with side-length $\bar{L}$ is used as an initial guess for the numerical solver [25, 27, 26]. Assuming the chief is at the origin of a local frame $\mathcal{T}$, the deputies' relative position vectors expressed in $\mathcal{T}$ frame are

$$^{\mathcal{T}}\boldsymbol{L}_1 = \begin{bmatrix} L \\ 0 \\ 0 \end{bmatrix} \quad ^{\mathcal{T}}\boldsymbol{L}_2 = \begin{bmatrix} \frac{1}{2}L \\ \frac{\sqrt{3}}{2}L \\ 0 \end{bmatrix} \quad ^{\mathcal{T}}\boldsymbol{L}_3 = \begin{bmatrix} \frac{1}{2}L \\ \frac{1}{2\sqrt{3}}L \\ \sqrt{\frac{2}{3}}L \end{bmatrix} \qquad (3.28)$$

$$\boldsymbol{r}_{d_1} = \boldsymbol{r}_c + \boldsymbol{L}_1 \quad \boldsymbol{r}_{d_2} = \boldsymbol{r}_c + \boldsymbol{L}_2 \quad \boldsymbol{r}_{d_3} = \boldsymbol{r}_c + \boldsymbol{L}_3 \qquad (3.29)$$

$$[\mathcal{OT}] = [\boldsymbol{C}_1(\theta_1)][\boldsymbol{C}_2(\theta_2)][\boldsymbol{C}_3(\theta_3)] \qquad (3.30)$$

$$\boldsymbol{v}_{d_1} = v_1\hat{\boldsymbol{v}}_c \quad \boldsymbol{v}_{d_2} = v_2\hat{\boldsymbol{v}}_c \quad \boldsymbol{v}_{d_3} = v_3\hat{\boldsymbol{v}}_c \qquad (3.31)$$

The velocities of the deputy spacecraft are assumed to have the same direction as the chief's velocity. The velocity magnitudes are computed through $v_j = \sqrt{2(\mathcal{E}_0 + \mu/r_j)}$, $j = 1, 2, 3$ where

(a) Formation Quality   (b) Inter-Spacecraft Range
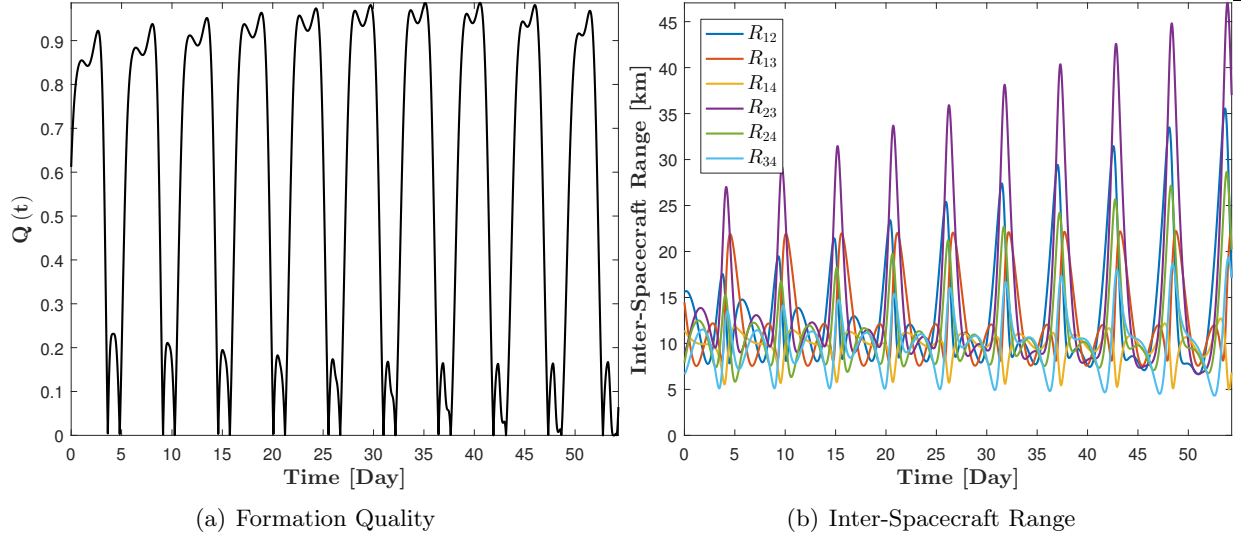
Figure 3.11: Tetrahedron Formation with Average Side-Length of 10 km (10 Orbit Optimized)

$\mathcal{E}_0 = -\mu/a_c$. This crude initial guess is by no means optimal but provides a good starting point for the numerical solver. The Cartesian states of the deputies are converted to orbital elements and those initial differential orbital elements are passed to the numerical solver as an initial guess. An example of a 10-orbit optimized tetrahedron formation design is shown in Fig. 3.11. As evident from Fig. 3.11(a), the formation is useful for at least 10 orbits before it quickly degrades in the following orbits due to the relative out-of-plane variations. The inter-spacecraft ranges shown in Fig. 3.11(b) indicate that the tetrahedron formation has no dangerous close approaches between any of its spacecraft pairs throughout the 10-orbit period.

3.3   Numerical Inclusion of SRP Invariant Condition

As evident from Eq. (3.17) and Eq. (3.27), there is no constraint that leads to the minimization of the the relative drift between the solar sails. The question arises is that whether minimizing the relative drift has any effect on the long-term stability of the formation. Another valid question is whether the formation stability can be improved without sacrificing formation quality. To investigate these questions, the numerical algorithm is modified to include a constraint on how much the deputy spacecraft are allowed to drift apart over the span of optimization. The modified algorithm is summarized as follows for the triangle formation,

$$
\begin{aligned}
\text{minimize} \quad & J = -\sum_{n=1}^{N_{orb}} J_n \\
\text{with respect to} \quad & \Delta \boldsymbol{\mathfrak{oe}}_0 = \begin{bmatrix} \Delta a_{j_0} & \Delta e_{j_0} & \Delta \omega_{j_0} & \Delta M_{j_0} \end{bmatrix}^T \\
\text{subject to} \quad & \ddot{\boldsymbol{r}} = -\frac{\mu}{r^3}\boldsymbol{r} + \boldsymbol{a}_s \\
& \Delta i_{j_0} = 0, \Delta \Omega_{j_0} = 0 \\
& k_j = \frac{2}{3}\dot{\lambda}_s \frac{e_j}{\sqrt{1-e_j^2}}\sqrt{\frac{\mu}{a_j}} \\
& \Delta l_{\min} \leq \Delta l_j \leq \Delta l_{\max}
\end{aligned}
\tag{3.32}
$$

An optimized 10 km triangle formation resulting from Eq. (3.32) is illustrated in Fig. 3.12. As shown in Fig. 3.12(a), the formation quality factor is slightly lower for the case where the relative SRP invariant condition is enforced. However, the formation quality factor degrades at a faster rate for the formation with no constraint on the relative drift, as evident in Fig. 3.12(b). The relative trajectories of the deputies with respect to the chief solar sail are illustrated in Fig. 3.12(e) and Fig. 3.12(f), corresponding to the case without the constraint and the case with relative drift constraint, respectively. With the numerical inclusion of the invariance condition, the formation stability is improved at the price of a small decrease in the formation quality.
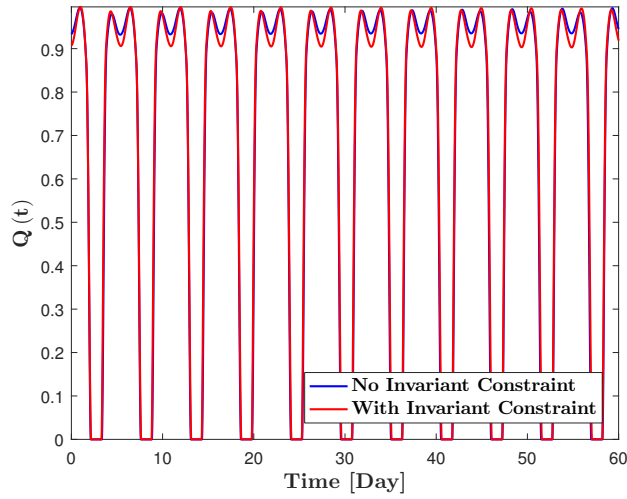
(a) Formation Quality Factor
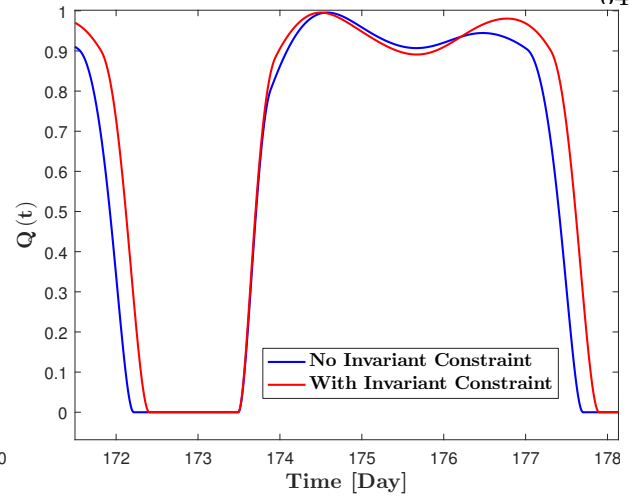
(b) Formation Quality Factor Close Up
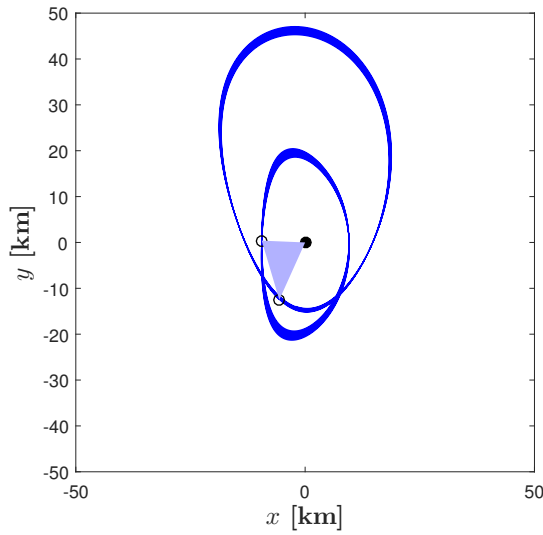
(c) Without Constraint - 60 Days Propagation
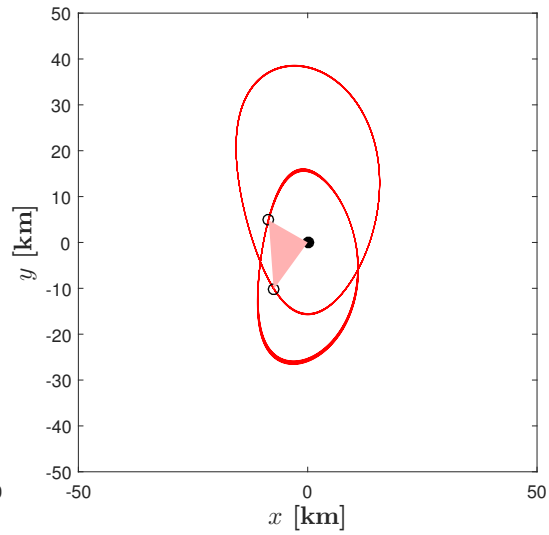
(d) With Constraint - 60 Days Propagation
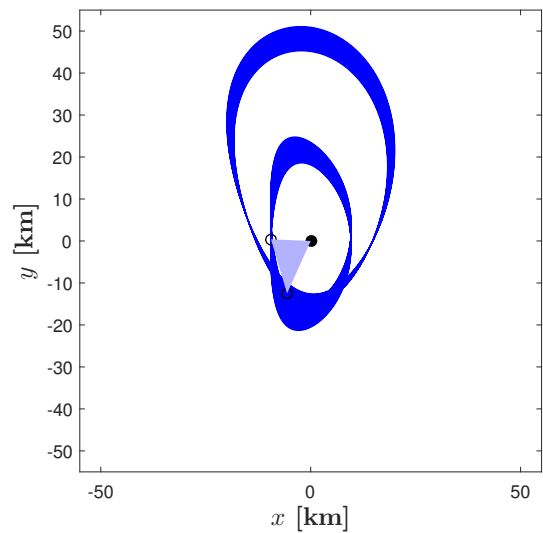
(e) Without Constraint - 180 Days Propagation
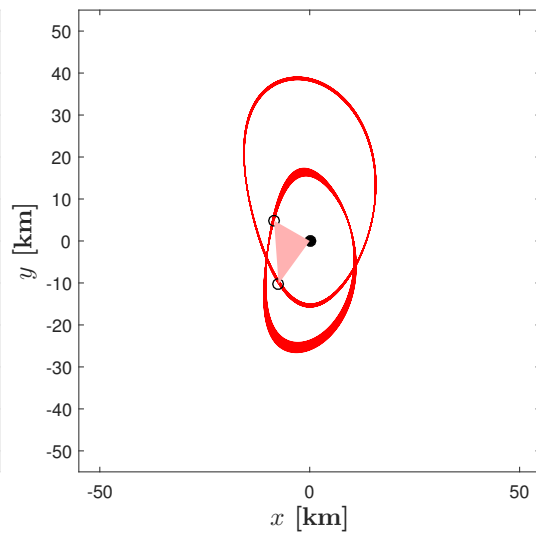
(f) With Constraint - 180 Days Propagation

Figure 3.12: Numerical Inclusion of SRP Invariant Condition in Triangle Formation Design

Chapter 4

Establishment of a Solar Sail Formation

4.1 Formation Deployment

In this section, formation deployment into the GEOSAIL-like mission orbit is discussed. This analysis is required for a more accurate modeling of the initial relative geometry between solar sails in addressing the formation establishment problem. It is assumed that a dedicated launcher releases the two solar sails directly into the 11 R_E × 30 R_E mission orbit. Note that to obtain the GEOSAIL mission orbit, an auxiliary upper stage is required regardless of the selected launch vehicle. The requirement for the two sails to be injected directly into the mission orbit narrows down the launch vehicle options and increases mission cost. However, in terms of flight dynamics, it is the most feasible option since the alternative would require injecting the sails into lower orbits and performing orbit raising to achieve the GEOSAIL mission orbit. The two sails are released sequentially at the perigee of the operational mission orbit. The chief is released along the local velocity direction. The deputy sail is released in a slightly different direction than the velocity to avoid close approaches. In this study, the deputy is assumed to be released along a direction that is 1° off the local velocity direction while lying within the orbit plane. The springs used in deploying the sails are assumed to be capable of generating an impulsive velocity change of 5 m/s relative to the auxiliary upper stage. Thus upon deployment, the impulsive velocity changes for the chief and deputy sails expressed in the $\mathcal{V}$ frame are ${}^{\mathcal{V}}\Delta\boldsymbol{v}_c = \begin{bmatrix} \Delta v_v & \Delta v_h & \Delta v_b \end{bmatrix}^T = \begin{bmatrix} 5 & 0 & 0 \end{bmatrix}^T$
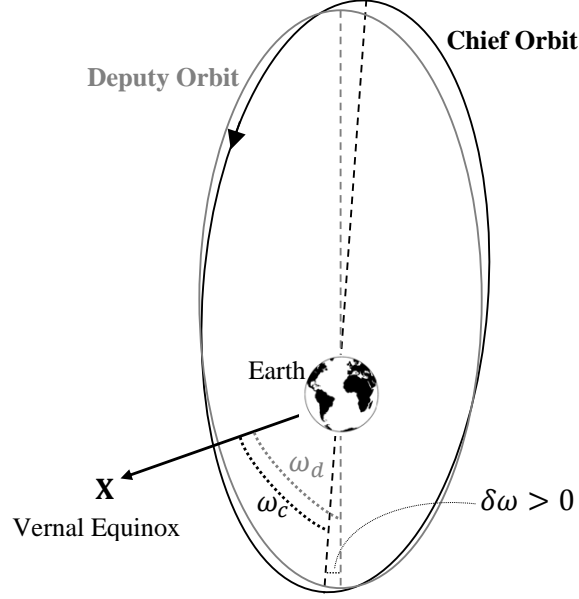
Figure 4.1: Post-Deployment Orbit Configuration

m/s and $^{\mathcal{V}}\Delta\boldsymbol{v}_d = \begin{bmatrix} 4.9992 & 0 & 0.0873 \end{bmatrix}^T$ m/s, respectively. The chief sail is released first, followed by the deputy after a buffer time to further reduce the chance of a close approach immediately after the deployment. During the next 3 orbits, the sails deploy their reflective surface and achieve the desired Sun-pointing mission attitude. The 3 orbit coasting time allows the ground segment to perform orbit and attitude determination before establishing the desired natural formation. To determine the effects of the sails' deployment on the orbit, Gauss's variation-of-parameters equations are used. Because the sails are deployed along the velocity direction, there are no out-of-plane variations. Therefore, the three main orbital elements that change after deployment are

$$\Delta a = \frac{2a^2 v}{\mu}\Delta v_v \tag{4.1a}$$

$$\Delta e = \frac{1}{v}\left[\frac{r}{a}\sin f\Delta v_b + 2\left(e + \cos f\right)\Delta v_v\right] \tag{4.1b}$$

$$\Delta\omega = \frac{1}{ev}\left[-\left(2e + \frac{r}{a}\right)\cos f\Delta v_b + 2\sin f\Delta v_v\right] - \frac{r\sin\theta\cos i}{h\sin i}\Delta v_h \tag{4.1c}$$

where $\theta = \omega + f$. For the chief sail that is released first at the orbit perigee, the changes in the orbital elements are $\Delta a_c \approx 1236.67$ km, $\Delta e_c \approx 0.005075$, and $\Delta\omega_c \approx 0$ deg. In this case, the buffer time selected is 25 minutes. This buffer time directly affects the differential orbital elements post-

deployment and, consequently, affects the finite burn for establishing the formation. Therefore, the deployment buffer time may be used as a **mission design parameter** for the establishment of a particular formation size. Releasing the deputy after 25 minutes leads to the deployment taking place at the true anomaly of $f \approx 3.5°$. Using Eq. (4.1), the changes in the deputy's a, e, and ω are $\Delta a_d \approx 1235.97$ km, $\Delta e_d \approx 0.005071$, and $\Delta \omega_d \approx 0.021$ deg. The corresponding differential orbital elements immediately after deployment are summarized in Table. 4.1.

Differential Element	Value	Unit
δa	-0.7	km
δe	-4.24×10^{-6}	-
$\delta \omega$	$+0.021$	deg

Table 4.1: Post-Deployment Differential Elements

To establish a natural leader-follower formation, the osculating δa, δe, and $\delta \omega$ must vanish at orbit apogee. In the next section, the two-point boundary value problem of formation establishment is discussed in detail, illustrating how to nullify these post-deployment differential elements by changing the deputy's orientation. The formation establishment problem using solar electric propulsion is discussed in Appendix A.

4.2   Optimal Control Theory

In the general optimal control problem, one seeks to find a state-control pair $\boldsymbol{x}(t)$, $\boldsymbol{u}(t)$ over a time span $[t_0, t_f]$ that minimizes a cost functional. The optimal control problem may be expressed

as [55],

$$\text{minimize} \quad J(\boldsymbol{x}(t), \boldsymbol{u}(t), t_0, t_f) = E(\boldsymbol{x}(t_0), \boldsymbol{x}(t_f), t_0, t_f) + \int_{t_0}^{t_f} F(\boldsymbol{x}(t), \boldsymbol{u}(t), t)\mathrm{d}t$$

with respect to $\quad \boldsymbol{u}(t)$

subject to $\quad \dot{\boldsymbol{x}} = \boldsymbol{f}(\boldsymbol{x}(t), \boldsymbol{u}(t), t) \quad$ (Dynamics Constraints) $\hspace{2cm}$ (4.2)

$$\boldsymbol{e}_L \leq \boldsymbol{e}(\boldsymbol{x}(t_0), \boldsymbol{x}(t_f), t_0, t_f) \leq \boldsymbol{e}_U \quad \text{(Bouldary Constraints)}$$

$$\boldsymbol{h}_L \leq \boldsymbol{h}(\boldsymbol{x}(t), \boldsymbol{u}(t), t) \leq \boldsymbol{h}_U \quad \text{(Path Constraints)}$$

The functions $E(\boldsymbol{x}(t_0), \boldsymbol{x}(t_f), t_0, t_f)$ and $F(\boldsymbol{x}(t), \boldsymbol{u}(t), t)$ are known as *endpoint* or *terminal cost* (Mayer) and *running cost* (Lagrangian) functions, respectively. Based on calculus of variation, a Hamiltonian, $\mathcal{H}$, is defined to conveniently formulate a procedure to solve the optimal control problem. The Hamiltonian $\mathcal{H}$ is defined as,

$$\mathcal{H}(\boldsymbol{\lambda}(t), \boldsymbol{x}(t), \boldsymbol{u}(t), t) = F(\boldsymbol{x}(t), \boldsymbol{u}(t), t) + \boldsymbol{\lambda}^T \boldsymbol{f}(\boldsymbol{x}(t), \boldsymbol{u}(t), t) \hspace{2cm} (4.3)$$

where $\boldsymbol{\lambda}(t)$ are known as *adjoint variables* (Lagrange multipliers). The necessary conditions for optimal control $\boldsymbol{u}^*(t)$, assuming that the admissible controls are unconstrained, may be written as,

$$\dot{\boldsymbol{x}}^* = \frac{\partial \mathcal{H}}{\partial \boldsymbol{\lambda}}(\boldsymbol{\lambda}^*(t), \boldsymbol{x}^*(t), \boldsymbol{u}^*(t), t) \hspace{3cm} (4.4\text{a})$$

$$\dot{\boldsymbol{\lambda}}^* = -\frac{\partial \mathcal{H}}{\partial \boldsymbol{\lambda}}(\boldsymbol{\lambda}^*(t), \boldsymbol{x}^*(t), \boldsymbol{u}^*(t), t) \hspace{3cm} (4.4\text{b})$$

$$0 = \frac{\partial \mathcal{H}}{\partial \boldsymbol{u}}(\boldsymbol{\lambda}^*(t), \boldsymbol{x}^*(t), \boldsymbol{u}^*(t), t) \hspace{3cm} (4.4\text{c})$$

$$\left[\frac{\partial E}{\partial \boldsymbol{x}}(\boldsymbol{x}^*(t_f), t_f) - \boldsymbol{\lambda}^*(t_f)\right]^T \delta\boldsymbol{x}_f + \left[\mathcal{H}(\boldsymbol{\lambda}^*(t_f), \boldsymbol{x}^*(t_f), \boldsymbol{u}^*(t_f)) + \frac{\partial E}{\partial t}(\boldsymbol{x}^*(t_f), t_f)\right]^T \delta t_f = 0 \quad (4.4\text{d})$$

For a *constrained* optimal control problem, where there are boundaries on either state or control, the Pontryagin's minimum principle must be applied. The Pontryagin's minimum principle states that an optimal control problem must minimize the Hamiltonian. In other words, we seek an optimal

control $\boldsymbol{u}^*(t)$ that satisfies,

$$\text{minimize} \quad \mathcal{H}(\boldsymbol{\lambda}(t), \boldsymbol{x}(t), \boldsymbol{u}(t), t)$$

$$\text{with respect to} \quad \boldsymbol{u}(t) \tag{4.5}$$

$$\text{subject to} \quad \boldsymbol{u} \in \mathbb{U}$$

where the control space $\mathbb{U}$ is constrained by,

$$\mathbb{U} = \left[\boldsymbol{u} : \boldsymbol{h}_L \leq \boldsymbol{h}(\boldsymbol{x}(t), \boldsymbol{u}(t), t) \leq \boldsymbol{h}_U \right] \cap \left[\boldsymbol{u} : \boldsymbol{u}_L \leq \boldsymbol{u} \leq \boldsymbol{u}_U \right] \tag{4.6}$$

The problem in Eq. (4.5) can be converted into a nonlinear programming problem (NLP) given

by,

$$\text{minimize} \quad \mathcal{H}(\boldsymbol{\lambda}(t), \boldsymbol{x}(t), \boldsymbol{u}(t), t)$$

$$\text{with respect to} \quad \boldsymbol{u}(t)$$

$$\tag{4.7}$$

$$\text{subject to} \quad \boldsymbol{h}_L \leq \boldsymbol{h}(\boldsymbol{x}(t), \boldsymbol{u}(t), t) \leq \boldsymbol{h}_U$$

$$\boldsymbol{u}_L \leq \boldsymbol{u} \leq \boldsymbol{u}_U$$

The optimal control problem converted into the NLP problem in Eq. (4.7) must satisfy the necessary conditions known as Karush-Kuhn-Tucker (KKT) conditions [55]. Define a new augmented Hamiltonian $\bar{\mathcal{H}}$ as,

$$\bar{\mathcal{H}}(\boldsymbol{\lambda}(t), \boldsymbol{x}(t), \boldsymbol{u}(t), t) = \mathcal{H}(\boldsymbol{\lambda}(t), \boldsymbol{x}(t), \boldsymbol{u}(t), t) + \boldsymbol{\mu}_h^T \boldsymbol{h}(\boldsymbol{x}(t), \boldsymbol{u}(t), t) + \boldsymbol{\mu}_x^T \boldsymbol{x}(t) + \boldsymbol{\mu}_u^T \boldsymbol{u}(t) \tag{4.8}$$

where $\boldsymbol{\mu} = (\boldsymbol{\mu}_h, \boldsymbol{\mu}_x, \boldsymbol{\mu}_u)$ are the adjoint functions associated with the path constrained, state variables constraints, and control variable constraints respectively. The KKT gradient normality condition that must be satisfied is,

$$0 = \frac{\partial \bar{\mathcal{H}}}{\partial \boldsymbol{u}} (\boldsymbol{\lambda}^*(t), \boldsymbol{x}^*(t), \boldsymbol{u}^*(t), t) \tag{4.9}$$

The complementarity conditions that must be checked as part of the KKT conditions are,

$$\mu_{h,i} = \begin{cases} \leq 0 & h_i(\boldsymbol{x}(t), \boldsymbol{u}(t), t) = h_{i_L} \\ = 0 & h_{i_L} < h_i(\boldsymbol{x}(t), \boldsymbol{u}(t), t) < h_{i_U} \\ \geq 0 & h_i(\boldsymbol{x}(t), \boldsymbol{u}(t), t) = h_{i_U} \end{cases} \tag{4.10}$$

$$\mu_{x,i} = \begin{cases} \leq 0 & x_i = x_{i_L} \\ = 0 & x_{i_L} < x_i < x_{i_U} \\ \geq 0 & x_i = x_{i_U} \end{cases} \tag{4.11}$$

$$\mu_{u,i} = \begin{cases} \leq 0 & u_i = u_{i_L} \\ = 0 & u_{i_L} < u_i < u_{i_U} \\ \geq 0 & u_i = u_{i_U} \end{cases} \tag{4.12}$$

Note that the KKT conditions are only necessary conditions and not sufficient conditions. If a optimal control $\boldsymbol{u}^*(t)$ satisfies the KKT conditions, that control trajectory is only an extremal control. Additional conditions must be checked to show whether an optimal control is a minimizer or a global minimizer of the Hamiltonian.

Most optimal control problems are solved numerically since analytic solutions are rarely available. There are generally two numerical methods for solving optimal control problems, namely, *indirect* and *direct* methods.

Indirect methods take advantage of calculus of variation and the Pontryagins minimum principle to drive first-order optimality conditions. Using indirect methods leads to the optimal control problem being converted to a boundary-value problem. Numerical methods such as multiple-shooting method are then utilized to solve the system of differential equations that satisfy the boundary conditions. The solutions found using indirect methods are typically highly accurate. However, necessary conditions must be derived analytically, which can be difficult in practice, especially for complicated nonlinear dynamical systems. The main difficulty that arises when using indirect methods is finding a *good* initial guess for the iterative numerical methods. The lack of an appropriate initial guess can quickly lead to divergence.

Direct methods do not require the necessary conditions to be analytically derived and they are not sensitive to the availability of an initial guess for adjoint variables; the state and control variables are adjusted to minimize the cost function. In direct methods, the continuous optimal control problem is transformed into a discrete nonlinear programming problem. The discretization

of the problem is necessary to define a system that has a *finite* number of variables. Thus, the total number of variables in the system becomes the number of variables in the original system multiplied by the number of discrete points. Different direct techniques are proposed for solving optimal control problems and they deploy different discretization techniques that directly affects the size of the problem at hand.

A fast direct method to solve optimal control problems is the *Legendre Pseudo-Spectral* Method. This method uses Legendre polynomials to approximate (discretize) states and controls for each segment between nodes. The nodes are selected using a Gaussian quadrature method. Once the problem is discretized, a NLP numerical solver is used to solve for the states and the required control. A version of this method is implemented in the software package DIDO [55]. Many direct methods do not produce costate information, which may be considered a drawback because it inhibits checking for optimality. The main advantage of DIDO is that it is capable of computing accurate values for the adjoint functions without solving the associated necessary conditions. This will allow checking the optimality conditions once DIDO converges on an optimal solution.

4.3   Problem Formulation for Optimal Formation Establishment

This section describes the optimal formation establishment problem in detail. In this problem formulation, the chief is assumed to maintain a Sun-pointing attitude and is assumed to not apply a control to *cooperatively* achieve a desired relative motion; only the deputy is assumed to have the capability to change its attitude in order to establish a desired formation. The chief's SRP acceleration expressed in the chief's LVLH frame is,

$$
{}^{\mathcal{O}_c}\boldsymbol{a}_{s_c} = {}^{\mathcal{O}_c}\begin{bmatrix} a_{r_c} \\ a_{\theta_c} \end{bmatrix} = k_c \, {}^{\mathcal{O}_c}\begin{bmatrix} \cos \phi_c \\ \sin \phi_c \end{bmatrix}
\tag{4.13}
$$

where the subscript c denotes the chief solar sail. The deputy solar sail is nominally maintaining a Sun-pointing attitude, but it is capable of changing its orientation within the orbit plane by $\delta\phi$. The change in deputy's orientation is assumed to have physical lower and upper limits. Therefore, the deputy's attitude varies from its nominal Sun-pointing attitude by $\delta\phi_{\min} \le \delta\phi(t) \le \delta\phi_{\max}$. The deputy's SRP acceleration expressed in the deputy's LVLH frame is written as,

$$
{}^{\mathcal{O}_d}\boldsymbol{a}_{s_d} = {}^{\mathcal{O}_d}\begin{bmatrix} a_{r_d} \\ a_{\theta_d} \end{bmatrix} = k_d \, {}^{\mathcal{O}_d}\begin{bmatrix} \cos\left(\phi_d + \delta\phi_d\right) \\ \sin\left(\phi_d + \delta\phi_d\right) \end{bmatrix}
\tag{4.14}
$$

The equations of motion for a spacecraft governed by the Gauss variational equations may be expressed using,

$$
\dot{\boldsymbol{œ}} = \boldsymbol{A} + \boldsymbol{B}\left(\boldsymbol{œ}\right)\boldsymbol{u}
\tag{4.15}
$$

where $\boldsymbol{u}$ is the perturbing acceleration and the matrices $\boldsymbol{A}$ and $\boldsymbol{B}\left(\boldsymbol{œ}\right)$ are defined as,

$$
\boldsymbol{A} = \begin{bmatrix} 0 & 0 & 0 & n \end{bmatrix}^T
\tag{4.16}
$$

$$
\boldsymbol{B}\left(\boldsymbol{œ}\right) = \begin{bmatrix} \dfrac{2ea^2 \sin f}{h} & \dfrac{2a^2 p}{hr} \\[2mm] \dfrac{p \sin f}{h} & \dfrac{\left[(p+r)\cos f + re\right]}{h} \\[2mm] -\dfrac{p \cos f}{he} & \dfrac{(p+r)\sin f}{he} \\[2mm] \dfrac{b(p \cos f - 2re)}{ahe} & -\dfrac{b(p+r)\sin f}{ahe} \end{bmatrix}
\tag{4.17}
$$

Let $\overline{\text{œ}}$ denote the orbital elements of the formation comprising both the chief and deputy solar sails,

$$\overline{\text{œ}} = \begin{bmatrix} \text{œ}_c & \text{œ}_d \end{bmatrix}^T = \begin{bmatrix} a_c & e_c & \omega_c & M_c & a_d & e_d & \omega_d & M_d \end{bmatrix}^T \tag{4.18}$$

The equations of motion for the formation may be written as,

$$\dot{\overline{\text{œ}}} = \overline{A} + \overline{B}\,\overline{a}_s \tag{4.19}$$

where the augmented matrices $\overline{A}$, $\overline{B}$, and $\overline{a}_s$ are defined as follows,

$$\overline{A}\,(n_c, n_d) = \begin{bmatrix} A_c \\ A_d \end{bmatrix} \tag{4.20}$$

$$\overline{B}\,(\text{œ}_c, \text{œ}_d) = \begin{bmatrix} B_c \\ B_d \end{bmatrix} \tag{4.21}$$

$$\overline{a}_s = \begin{bmatrix} a_{s_c} \\ a_{s_d} \end{bmatrix} \tag{4.22}$$

The formation establishment problem is formulated as follows,

$$\text{minimize} \quad J = \int_{t_0}^{t_f} \delta\phi_d^2(t)\,\mathrm{d}t$$

$$\text{with respect to} \quad \dot{\overline{\text{œ}}} = \overline{A} + \overline{B}\,\overline{a}_s$$

$$\text{subject to} \quad \overline{\text{œ}}\,(t_0) = \overline{\text{œ}}_0$$

$$\delta\text{œ}\,(t_f) \leq \delta\text{œ}_f \tag{4.23}$$

$$\delta\phi(t_0) = \delta\phi(t_f) = 0$$

$$\delta\phi_{\min} \leq \delta\phi(t) \leq \delta\phi_{\max}$$

where the differential orbital elements $\delta\text{œ}$ are defined as,

$$\delta\text{œ} = \text{œ}_d - \text{œ}_c = \begin{bmatrix} \delta a & \delta e & \delta\omega & \delta M \end{bmatrix}^T \tag{4.24}$$

The array $\delta\text{œ}_f$ contains the desired osculating differential elements at the final boundary epoch. It is assumed that the deputy starts with a Sun-pointing attitude flying in a Sun-synchronous orbit. Because the desired relative motions are natural, the deputy solar sail must have a Sun-pointing attitude once the formation is established, otherwise the relative secular drift rates due to the relative

SRP forces will lead to the degradation of the achieved formation. For these reasons, the constraint $\delta\phi(t_0) = \delta\phi(t_f) = 0$ is included in the formation establishment problem in Eq. (4.23).

For this formation establishment problem, two different time horizons are examined. At first, it is assumed that the deputy solar sail achieves the desired relative motion within 0.5 orbit (denoted by T-1), as illustrated in Fig. 4.2(a). The same problem is then solved assuming that the formation is established in 1.5 orbits (T-2), as shown in Fig. 4.2(b). Similarly, two initial boundaries ($\overline{\boldsymbol{\infty}}_0$) are selected to further investigate the sensitivity of the control effort to initial relative geometry. The first initial boundary (IB-1) is assumed to be the post-deployment state followed by 3 coasting orbits. The second initial boundary (IB-2) is assumed to be the post-deployment state without any coasting phase.

Once the optimal control problem is solved, the solution is first checked for its feasibility. This is to assure that the solution satisfies the the ordinary differential equations (ODE), since there is no propagation involved in the Legendre Pseudo-Spectral method employed to solve the optimal control problem. Once a solution satisfies the ODE feasibility test, the necessary conditions are numerically checked to test the optimality of the solution.
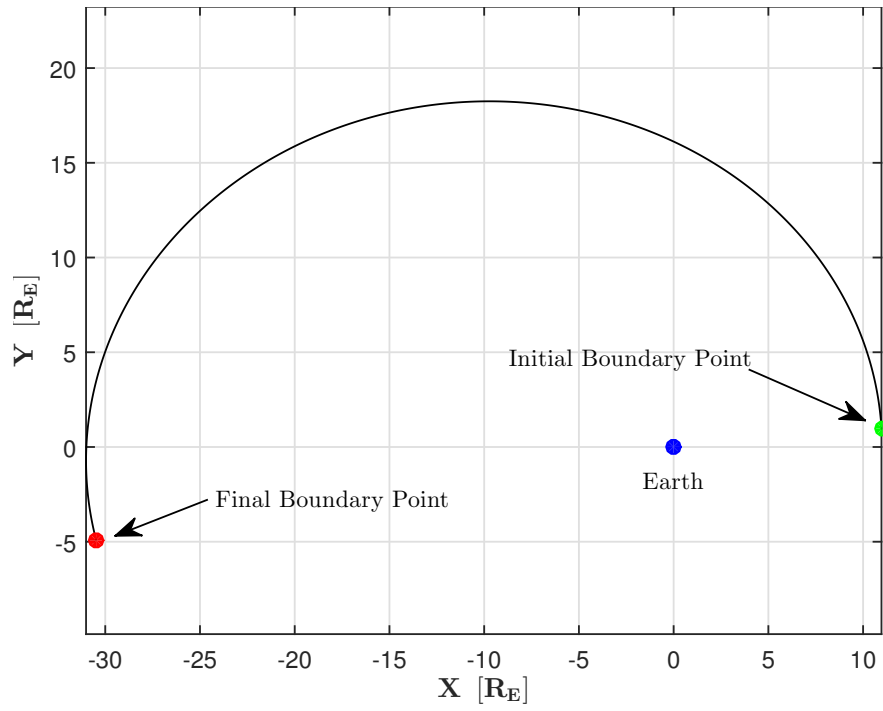
(a) 0.5 Orbit
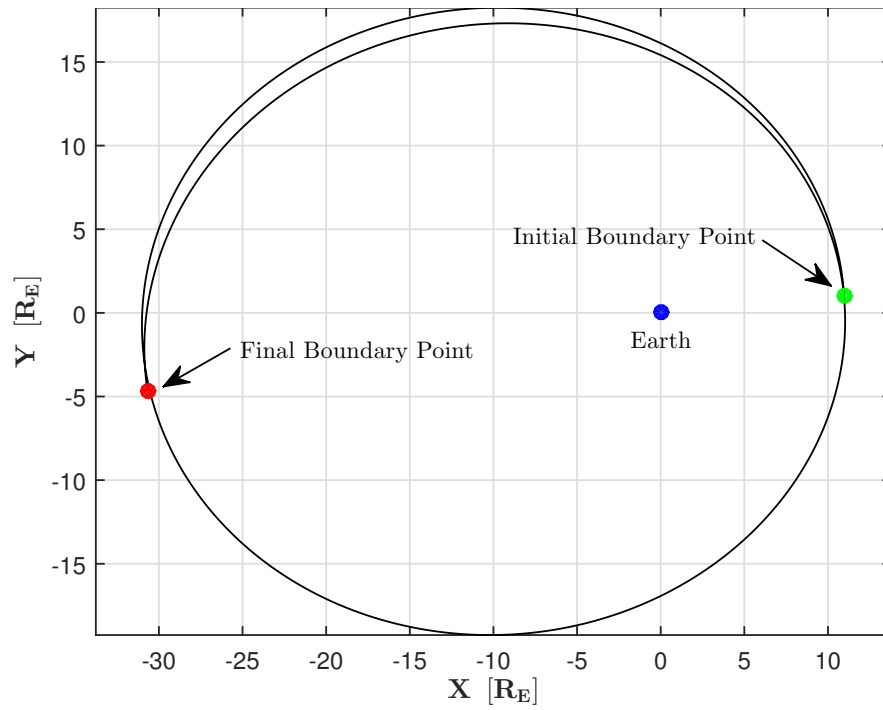
(b) 1.5 Orbit

Figure 4.2: Time-Horizons Used in Solving the Optimal Formation Establishment Problem

4.3.1   Leader-Follower Formation Establishment

As shown in Chapter 2, an achievable simple natural formation is the leader-follower formation. This formation requires both the chief and deputy to be in the same orbit and consequently have the same characteristic acceleration. The same characteristic acceleration implies that the two solar sails must have the same design and reflective surface area. Building two identical solar sails may reduce cost and complexity in terms of design. For a leader-follower formation, the desired osculating orbital elements at the final epoch are,

$$\delta \boldsymbol{\alpha}_f = \begin{bmatrix} \delta a_f & \delta e_f & \delta \omega_f & \delta M_f \end{bmatrix}^T = \begin{bmatrix} 0 & 0 & 0 & \delta M_f \end{bmatrix}^T \tag{4.25}$$

Depending on the value of δM_f, the leader-follower formation has a different size. Thus, δM_f directly controls the relative formation size, which is typically dictated by the scientists for magnetosphere missions.

The optimal formation establishment problem is solved using the initial boundary IB-1 and the time horizon T-1 for four different formation sizes as shown in Fig. 4.6. The entire formation deployment and establishment scenario as seen by the chief solar sail is illustrated in Fig. 4.3(a). As noted earlier, the chief sail is released first along the velocity direction. After 25 minutes, the deputy sail is released along a direction that is 1° off the local velocity direction. Because there is a difference between the orbit periods of the two sails due to nonzero δa, the deputy experiences a secular drift in the along-track direction during the next 3 orbits. After the coasting time, the deputy begins to change its attitude to achieve the leader-follower formation at the chief's orbit apogee. The controller's effort is shown in Fig. 4.3(b). In all cases, the control effort falls within the specified imposed constraints. For the initial boundary IB-1, the most optimal formation is achieved for the $\delta M_f = +0.0205°$ case, which leads to the smallest cost of $J = 0.00025$ as evident by Table. 4.2 and Fig. 4.3(b). Although the required attitude change does not exceed the limits defined, the rate of change of $\delta \phi$ is relatively high for the two cases shown in blue and red. Given the size of the solar sail assumed in this study, such angle rates may or may not be achievable. Thus, picking

the right formation size for a given initial boundary is important. The time history of the adjoint variables is shown in Fig. 4.4(a) for the $\delta M_f = +0.0205°$ case. As shown in Fig. 4.4(b), the adjoint variables are used to check the *gradient normality condition* of Eq. (4.9). The variations in the differential elements throughout the formation establishment process is illustrated in Fig. 4.5. It is evident that the initial differential orbital elements in Table. 4.1 are nullified to establish the leader-follower formation. Note that the differential element δa increases in magnitude from -0.7 km at the initial boundary to -26 km before it is nullified at the final epoch. Similarly, there is a significant variation in the δe before the formation is established.

(a) Relative Trajectory in Chief's LVLH Frame

(b) Control Effort
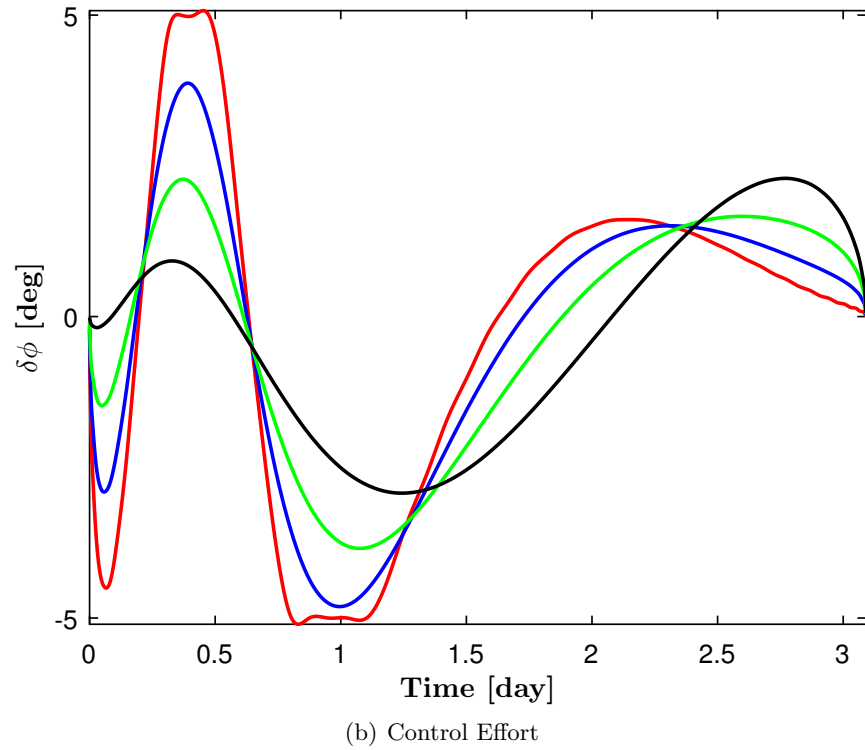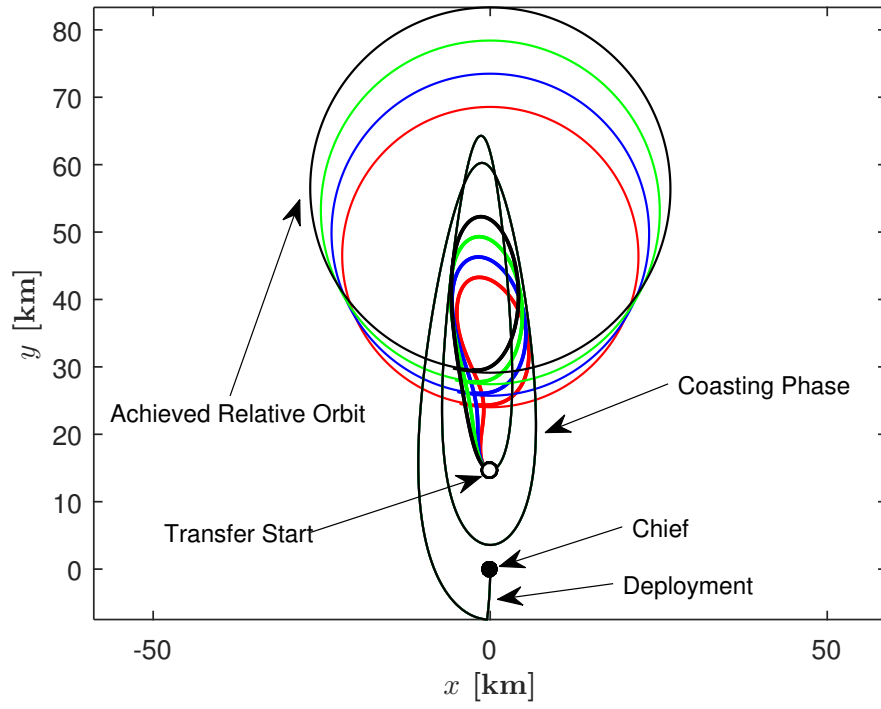
Figure 4.3: Leader-Follower Formation Establishment (IB-1 — T-1)
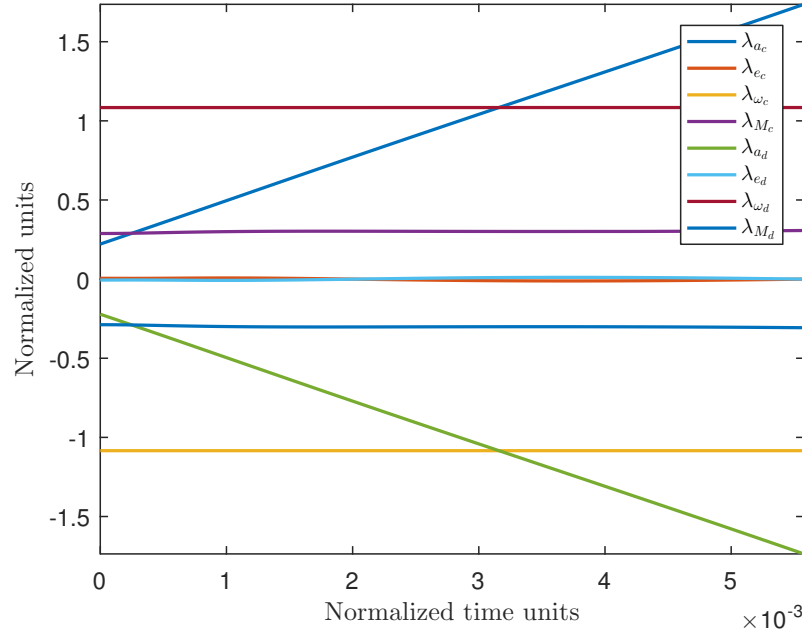
(a) Time History of Adjoint Variables
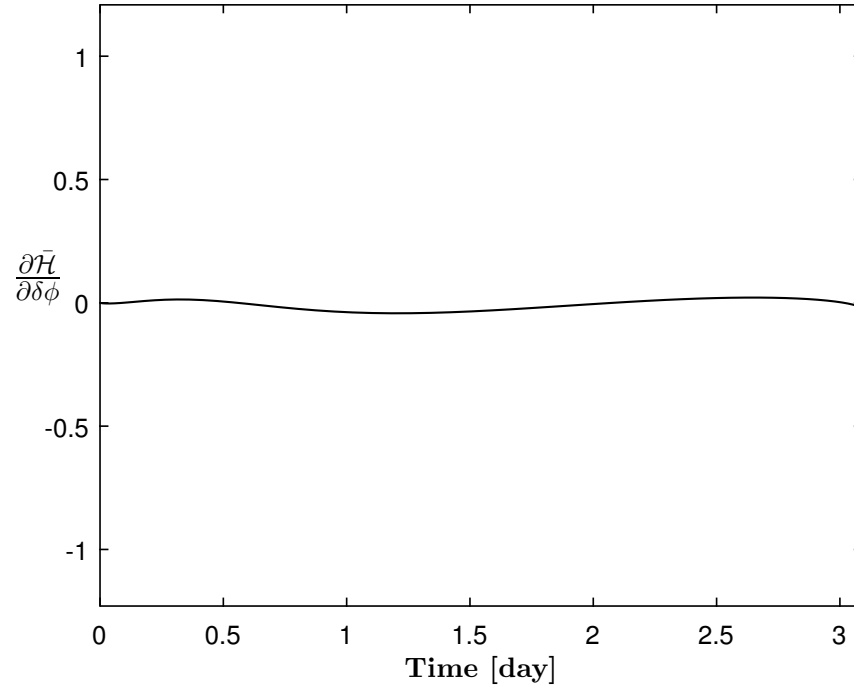
(b) Verification of Necessary Condition for Optimality

Figure 4.4: Checking First-Order Optimality Conditions

(a) Difference in Semi-Major Axis

(b) Difference in Eccentricity

(c) Difference in Argument of Perigee

(d) Difference in Mean Anomaly

Figure 4.5: Variation in Differential Elements throughput the Formation Establishment

To illustrate the effects of the initial boundary (initial relative geometry of the two sails) on the control performance, the optimal formation establishment is solved for the same formation sizes assuming the initial boundary condition IB-2. The corresponding cost to each of the desired relative geometries are shown in Table. 4.2. For this initial boundary, the most optimal control effort corresponds to the smallest desired relative motion of $\delta M_f = +0.0169°$. As the formation size increases, the required control becomes less optimal. For the case of $\delta M_f = +0.0205°$, the rate of change of $\delta\phi_d$ is high, which may or may not be achievable for the deputy solar sail. Comparing Fig. 4.6 to Fig. 4.3, it is evident that different initial relative geometry yields a different optimal control for the same desired formation. Therefore, a careful formation deployment strategy must be selected, since the deployment directly affects the relative initial geometry between two sails before the formation is established. This is typically not an issue for spacecraft that use chemical propulsion. However, in the case of solar sails and systems lacking high thrust propulsion, the deployment strategy may be used as a knob to turn for setting up the initial relative geometry such that the sail's effort to achieve the desired relative motion is minimized.

To illustrate the effect of time-horizon on the control, the formation establishment problem is solved using the IB-1 boundary conditions and the time span T-2. Two trajectories are generated for two different formation sizes as illustrated in Fig. 4.7. Comparing Fig. 4.3(b) to Fig. 4.7(b), it is clear that the sail requires smaller changes in its orientation to achieve the desired relative motion. Therefore, as the time-horizon increases, the deputy's control effort decreases. The increase in the time horizon directly increases the computational time for the numerical optimal control solver, which may be an issue in practice.

Table 4.2: Cost vs. Formation Size in Establishment of Leader-Follower Formation

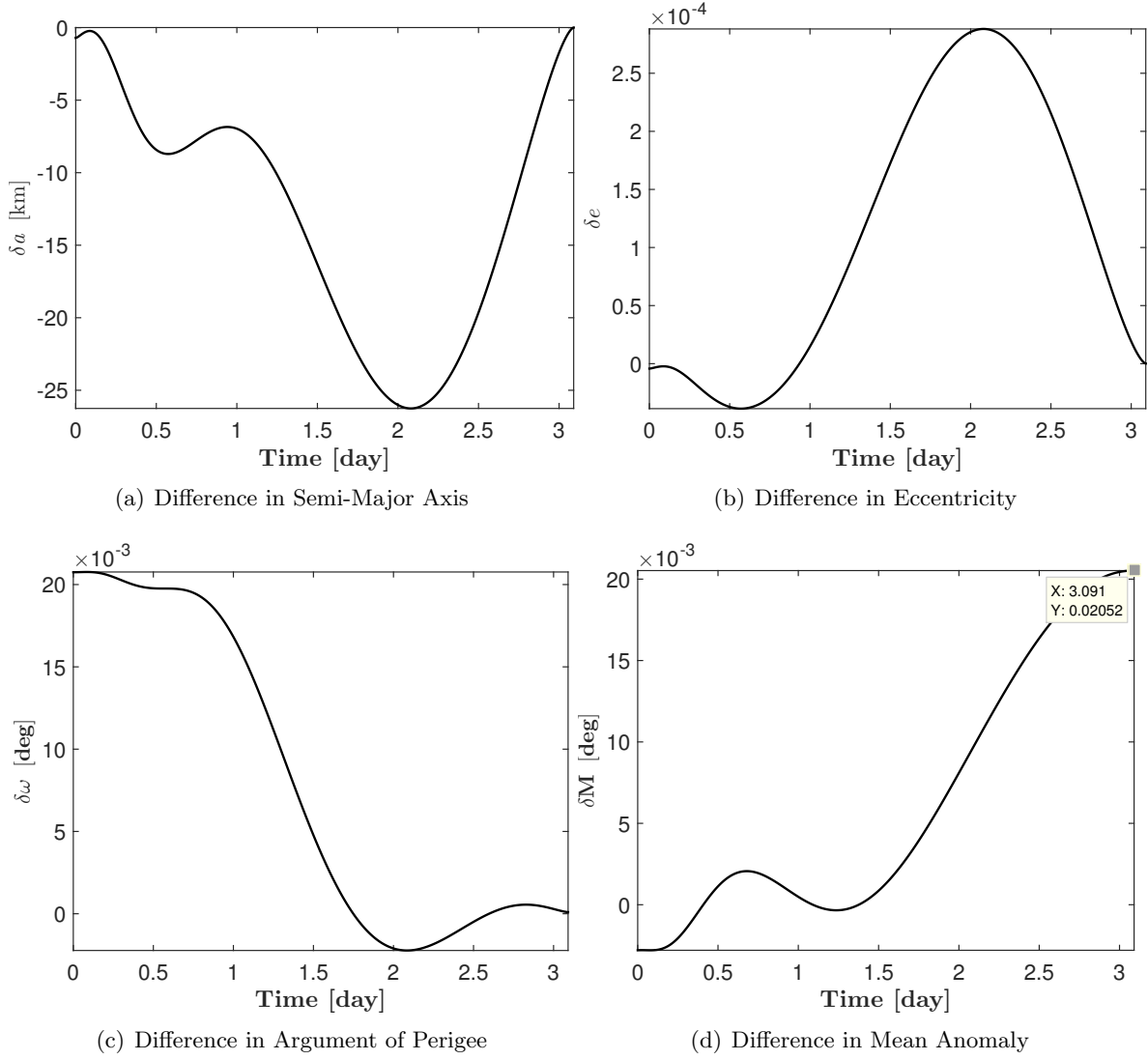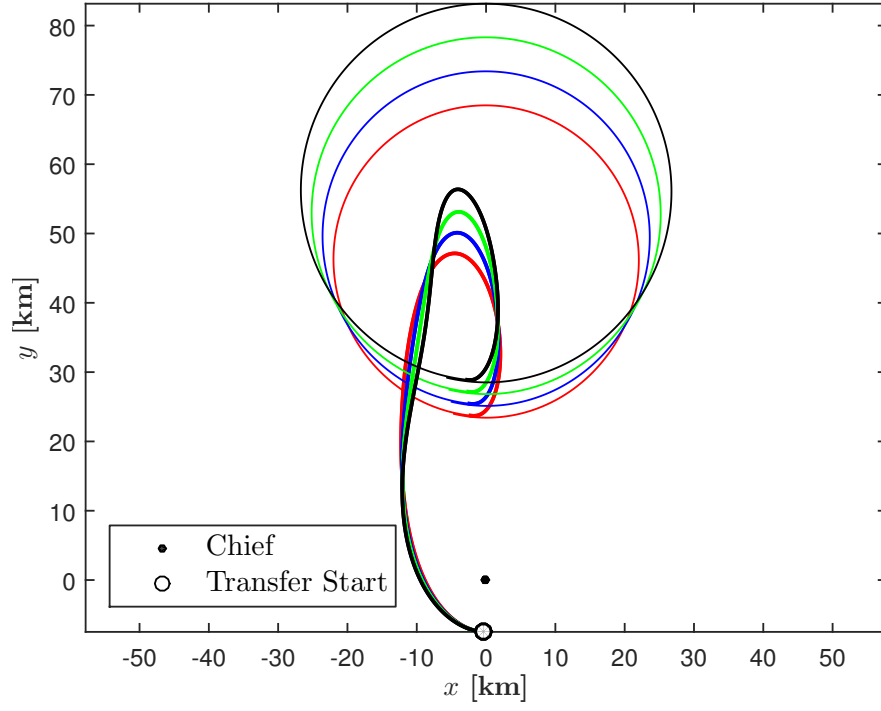| Trajectory	Desired Differential Mean Anomaly	IB-1 T-1 Case	IB-2 T-1 Case
Red	$\delta M_f = +0.0169°$	$J = 0.00072$	$J = 0.00034$
Blue	$\delta M_f = +0.0181°$	$J = 0.00047$	$J = 0.00051$
Green	$\delta M_f = +0.0193°$	$J = 0.00031$	$J = 0.00075$
Black	$\delta M_f = +0.0205°$	$J = 0.00025$	$J = 0.00110$

(a) Relative Trajectory in Chief's LVLH Frame
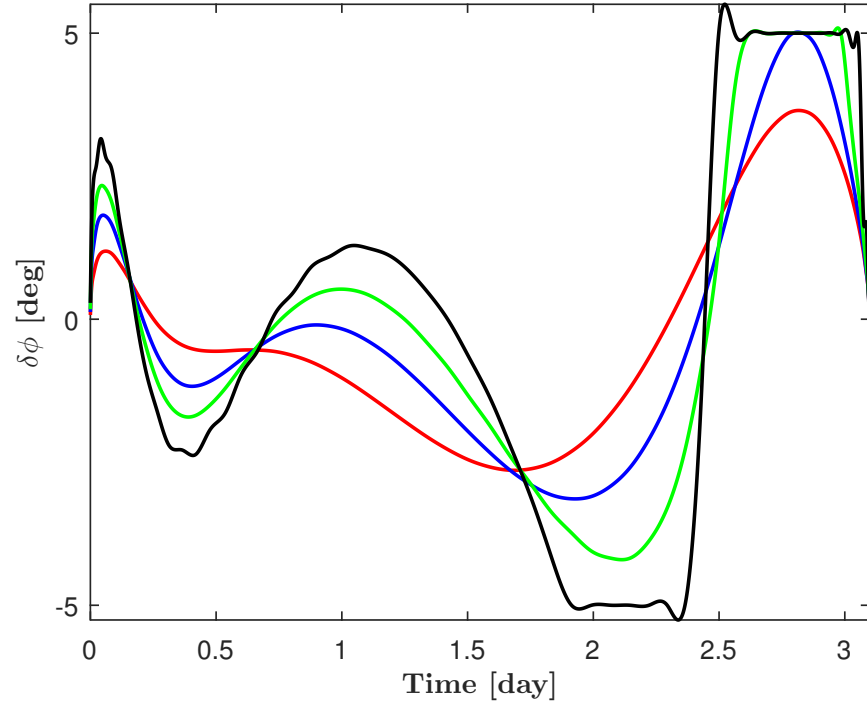
(b) Control Effort

Figure 4.6: Leader-Follower Formation Establishment (IB-2 — T-1)
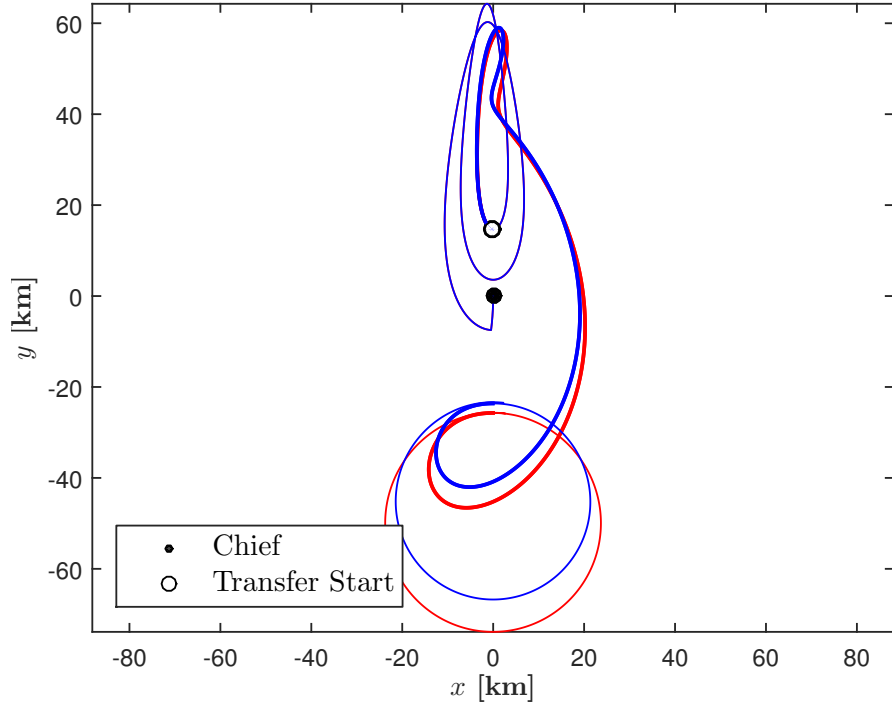
(a) Relative Trajectory in Chief's LVLH Frame
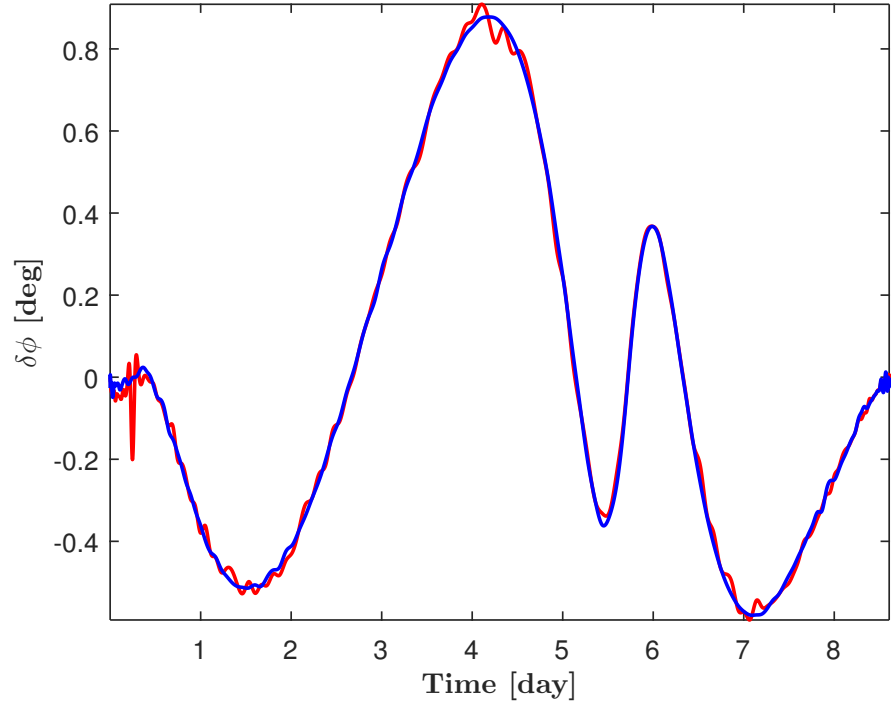
(b) Control Effort

Figure 4.7: Leader-Follower Formation Establishment (IB-1 — T-2)

4.3.2 Effects of Changing the Measure of Optimality

As evident from Eq. (4.23), the cost function selected is the $\mathcal{L}_2$ norm of the change in sail's orientation, which leads to smooth changes in $\delta\phi$. To explore the effects of cost function on the controller performance, the cost function is changed from $\mathcal{L}_2$ norm to $\mathcal{L}_1$ norm. Thus the formulation in Eq. (4.26) is changed to,

$$
\begin{aligned}
\text{minimize} \quad & J = \int_{t_0}^{t_f} |\delta\phi_d(t)| \, \mathrm{d}t \\
\text{with respect to} \quad & \dot{\overline{\mathbf{œ}}} = \overline{\boldsymbol{A}} + \overline{\boldsymbol{B}} \, \overline{\boldsymbol{a}}_s \\
\text{subject to} \quad & \overline{\mathbf{œ}}\,(t_0) = \overline{\mathbf{œ}}_0 \\
& \delta\mathbf{œ}\,(t_f) \leq \delta\mathbf{œ}_f \\
& \delta\phi(t_0) = \delta\phi(t_f) = 0 \\
& \delta\phi_{\min} \leq \delta\phi(t) \leq \delta\phi_{\max}
\end{aligned}
\tag{4.26}
$$

As evident from Fig. 4.8(a), the desired leader-follower formation is established in all cases. However, the control effort, Fig. 4.8(b), seems to behave similarly to a *bang-bang* controller. Due to the high frequency of variations in the deputy's attitude, which is difficult to achieve for a solar sail, it is concluded that the $\mathcal{L}_1$ norm cost function does not yield solutions that are practical. Similar to the $\mathcal{L}_2$ norm control, the black trajectory leads to the lowest cost relative to other formation sizes. The main challenge in controlling a solar sail's attitude are the physical limits on the angular velocity that a large solar sail is able to achieve. For this reason, it is crucial to assure that the sail's orientation is not subjected to rapid changes. To achieve slow changes in orientation, the cost function is changed from minimizing the angle $\delta\phi$ to minimizing the angle rate $\delta\dot{\phi}$. The effects of changing the measure of optimality is illustrated in Fig. 4.9 for four different cost functions, namely, $||\delta\phi(t)||_{\mathcal{L}_2}^2$, $||\delta\dot{\phi}(t)||_{\mathcal{L}_2}^2$, $||\delta\dot{\phi}(t)||_{\mathcal{L}_1}$, and $||\delta\phi(t)||_{\mathcal{L}_1}$. It is evident in Fig. 4.9(b) that minimizing the $\mathcal{L}_1$ norm of $\delta\dot{\phi}$ leads to nearly zero rates throughout the maneuver but requires rapid changes in attitude at the boundary points that may or may not be achievable depending on the type of attitude control system on-board.
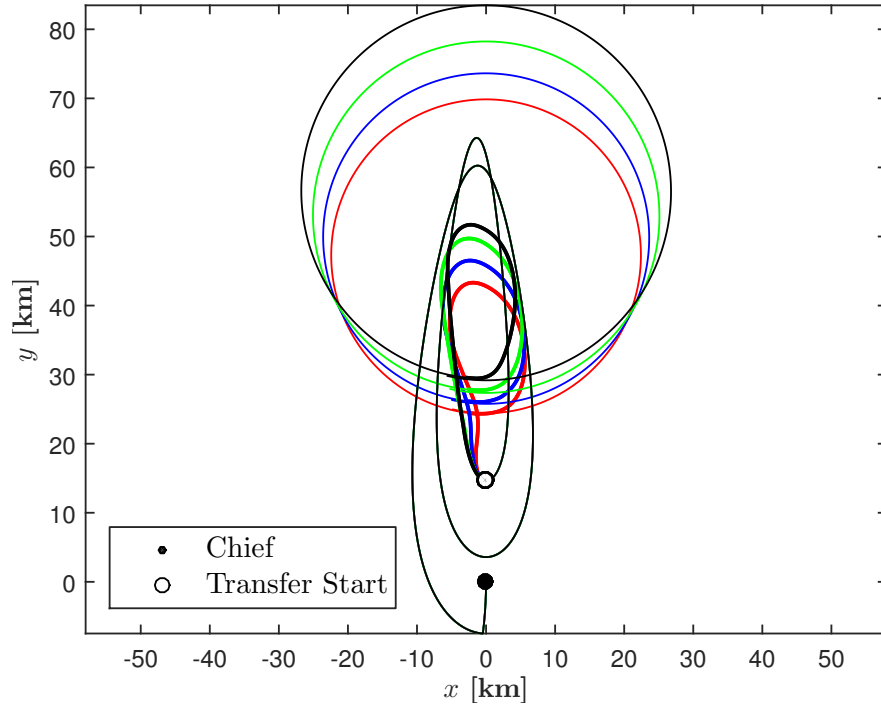
(a) Relative Trajectory in Chief's LVLH Frame
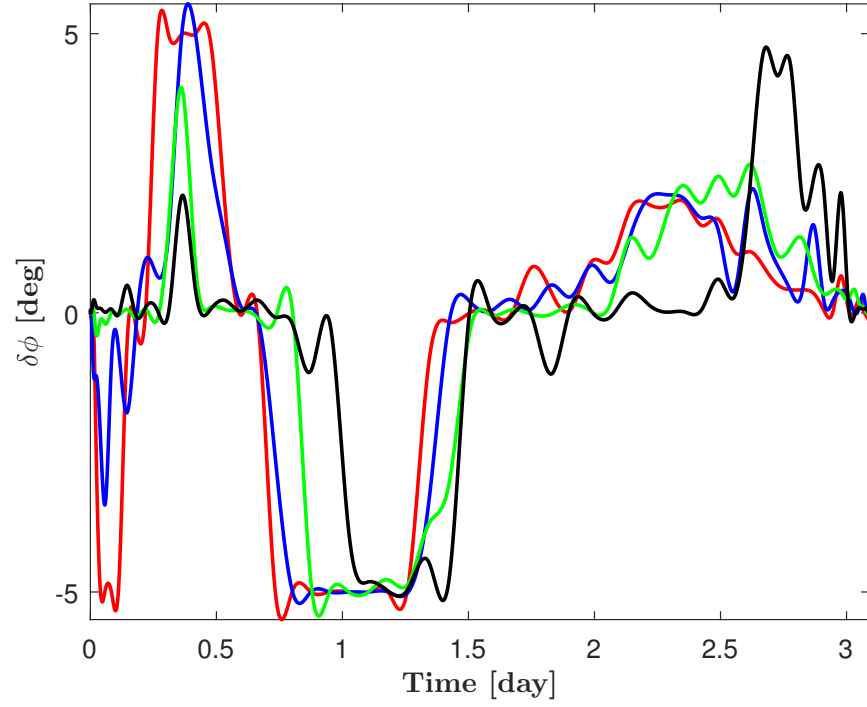
(b) Control Effort

Figure 4.8: Optimal Leader-Follower Formation Establishment with $\mathcal{L}_1$ Norm Cost Function

(a) Changes in Attitude

(b) Changes in Angle Rate

(c) Transfer Orbit

(d) Relative Trajectory in Chief's LVLH Frame
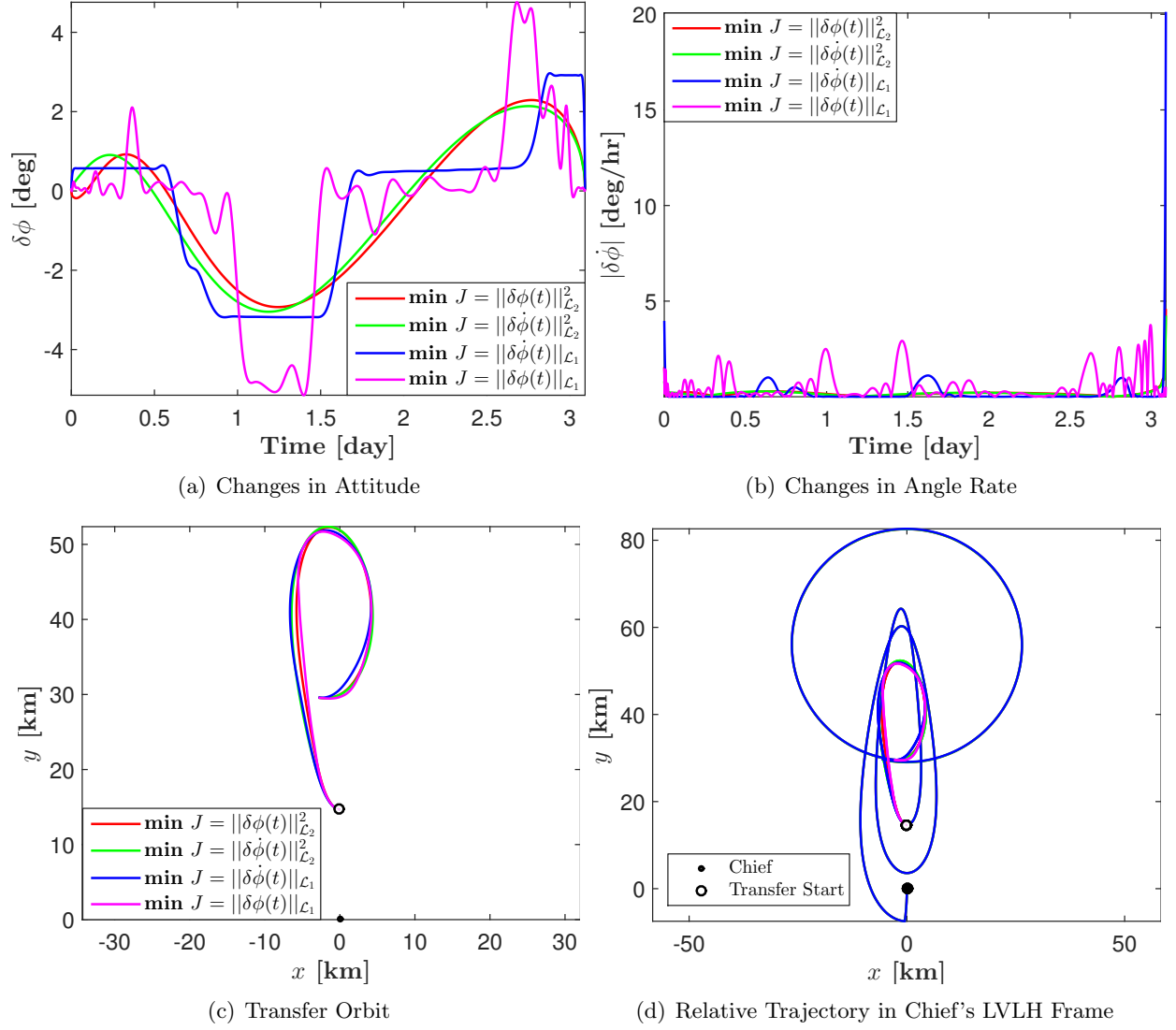
Figure 4.9: The Effects of Employing Different Cost Functions for a Specific Desired Formation

4.3.3   SRP Invariant Formation Establishment

In this section, the establishment of other SRP invariant formations besides the trivial solution of leader-follower formation is explored. First, SRP invariant formations are designed according to the numerical algorithm described in Chapter 3. Those states are then used as the final boundary conditions for the formation establishment problem in Eq. (4.23).

Fig. 4.10 illustrates families of SRP invariant relative orbits established by the deputy using the IB-1 initial boundary and T-1 time span. Note that the only difference between the deputy's desired relative orbits shown in Fig. 4.10(a) is the difference in the mean anomaly δM_f with respect to the chief in each case. In terms of the cost, the green trajectory is the most optimal to achieve, followed by the black, blue, and red trajectories.

The establishment of another SRP invariant relative orbit family is shown in Fig. 4.11(a) for the IB-2 initial boundary and T-1 time span. The corresponding control effort for each case is in Fig. 4.11(b). In terms of the cost, the green trajectory is the most optimal to achieve followed by the blue, black, and red trajectories.
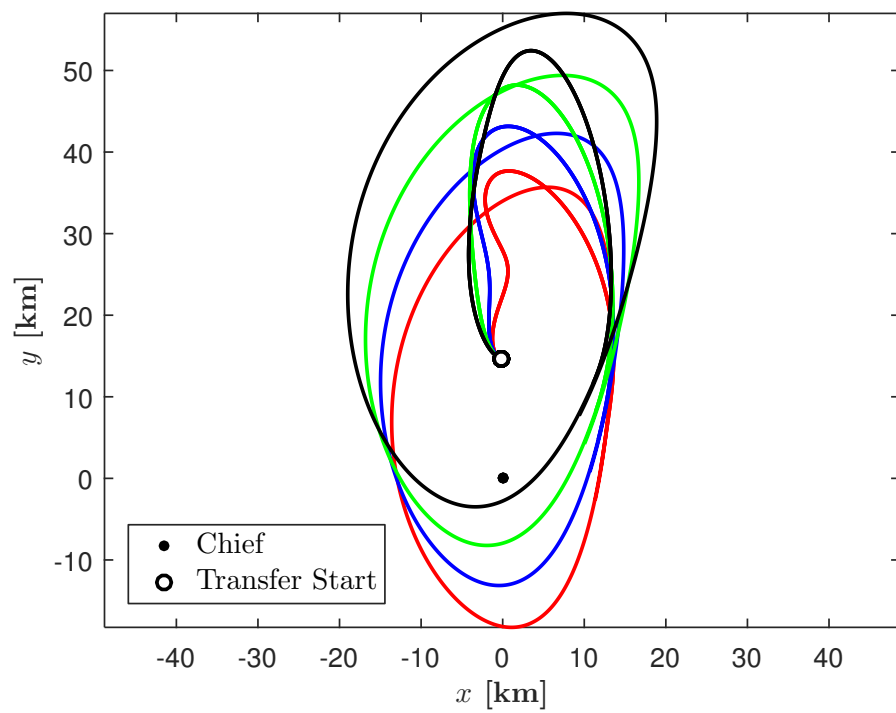
(a) Relative Trajectory in Chief's LVLH Frame
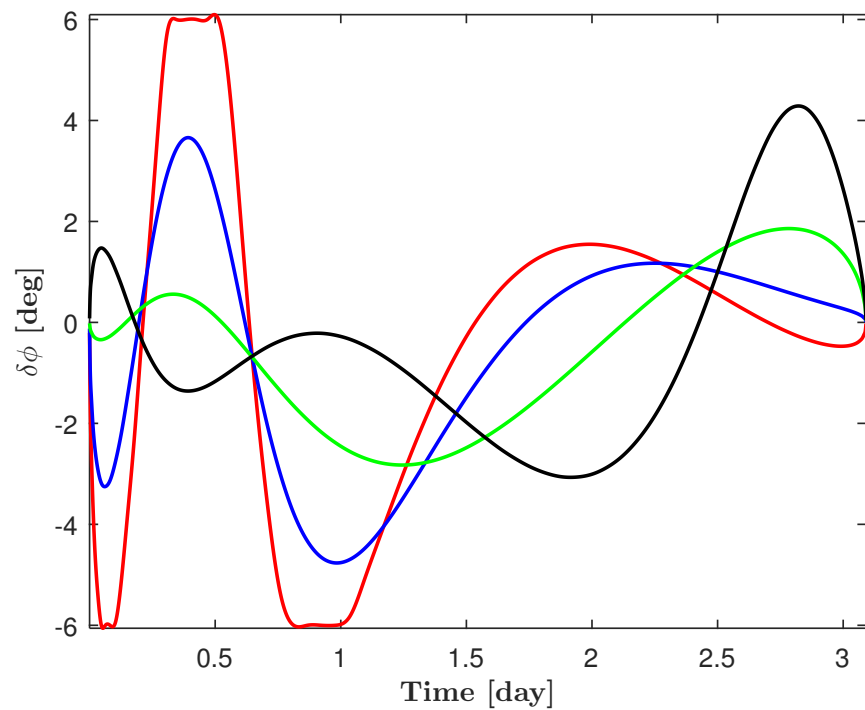
(b) Control Effort

Figure 4.10: Optimal Establishment of SRP Invariant Relative Orbits (IB-1 — T-1)
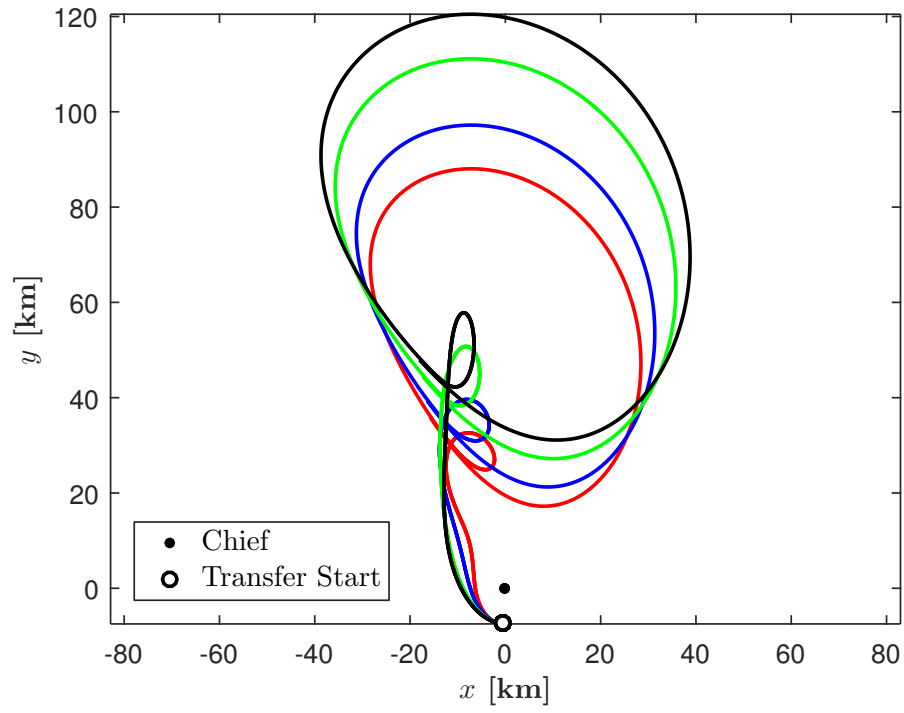
(a) Relative Trajectory in Chief's LVLH Frame
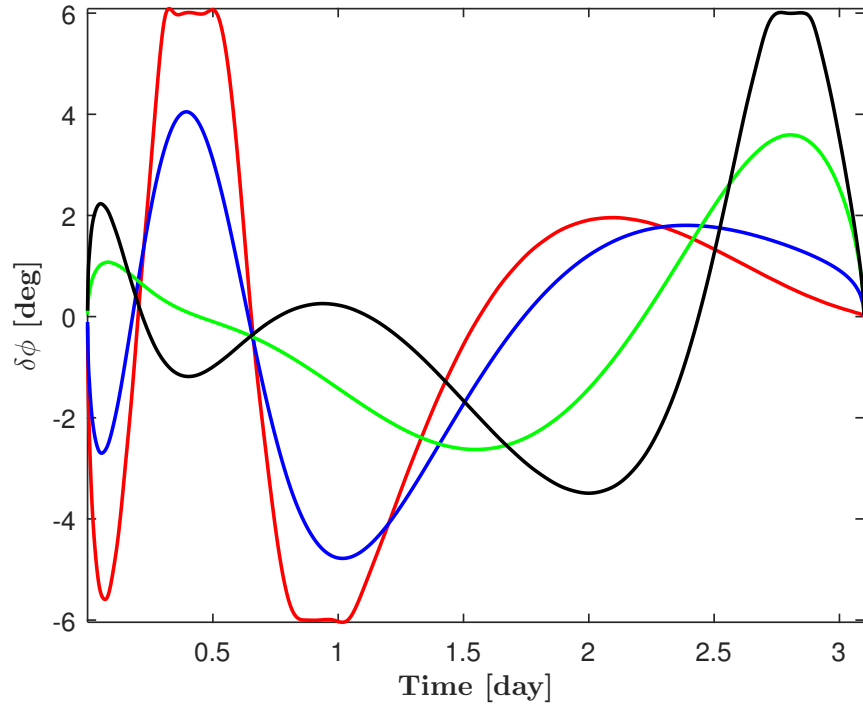
(b) Control Effort

Figure 4.11: Optimal Establishment of SRP Invariant Relative Orbits (IB-2 — T-1)

4.4　　　Triangle Formation Establishment

In this section, the establishment of the in-plane equilateral triangle formation is discussed. A triangle formation with a specific average side-length is first designed as described in Chapter 3. The states are then used to solve the optimal formation establishment problem. For this example, the formation size to be achieved is chosen to be a 40 km formation. The optimal control problem fails to converge for both initial boundary conditions resulting from the assumed deployment strategy. For each of the initial boundary conditions both time-horizons are explored, but changing the time-horizons does not help with convergence.

The initial boundary condition is modified to a state that is closer to the final desired relative trajectory in terms of relative position and velocity. The optimal control problem is then solved for various initial boundary conditions, as illustrated in Fig. 4.12. The establishment of the desired relative trajectory for various initial boundary conditions are illustrated in Fig. 4.12(a). The final desired relative trajectory is shown in dashed lines. As evident from Fig. 4.12(b), even a slightly different initial relative state leads to a significantly different control effort. The relative position and velocity for each of the initial boundary conditions are given in Table. 4.3. Since the natural relative motion mostly takes place in the along-track direction (y axis), the initial boundaries with larger initial relative velocity errors in the along-track direction require more control effort to converge. This is most evident in Case 3 shown in Table. 4.3. To draw stronger conclusions regarding the controllability of the sail, we switch from the relative position and velocity to orbital elements and use the averaged results from Eq. (2.33).

Table 4.3: Deputy's Initial Relative State with respect to the Desired Relative Orbit at Epoch t_0

Relative State	Case 1	Case 2	Case 3	Case 4
x_0 [km]	-2.91	0.67	-0.39	1.26
y_0 [km]	19.54	18.57	18.55	11.57
$\dot{x}_0$ [m/s]	0.3738	0.3494	0.3506	0.2515
$\dot{y}_0$ [m/s]	0.1353	-0.1189	-0.0525	-0.1835
J	0.0006	0.0001	4×10^{-6}	0.0009

As evident from Eq. (2.33), the average semi-major axis does not change for a perfectly Sun-pointing attitude or tiny variations in the attitude. This suggests that the average semi-major axis is difficult to control if the attitude variation is restricted to vary only a few degrees. To evaluate this hypothesis, we create a test case where the deputy's initial state and the desired state only differ in their average semi-major axis. This allows testing the controllability of only semi-major axis by isolating the semi-major axis from other orbital elements and the effects of their variations on semi-major axis. Fig. 4.13(b) illustrates the control effort for various offsets in average semi-major axis. As expected, the control effort increases with the increase in the average semi-major axis offset. In the case of $\delta\bar{a} = 10$ km, the controller reaches the maximum allowable variation in the attitude. The optimal control problem will have no solution if the $\delta\bar{a}$ is increased beyond 10 km while the physical constraint on attitude variation is kept unchanged. Given the size of the semi-major axis which is approximately 20.5 $\mathrm{R_E}$, it is evident that the semi-major axis is only changed by 0.0015% to 0.0076% for the $\delta\bar{a}$ cases explored in this simulation. Thus, it can be concluded that if there is a significant difference in the average semi-major axis between the deputy's current and desired states, the desired relative motion may not be achievable by using small variations in the sail's orientation.
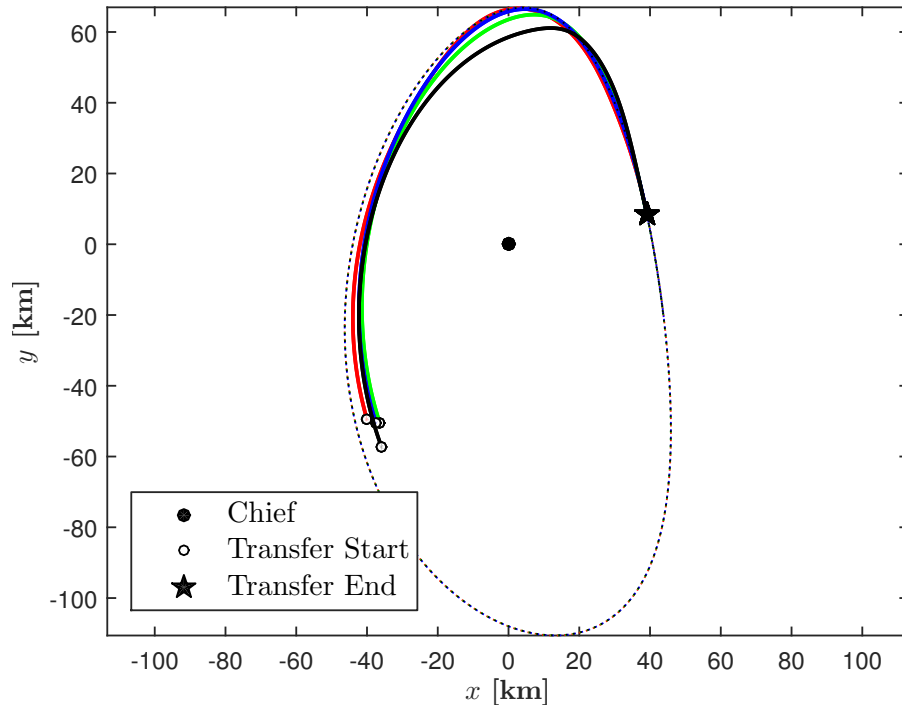
(a) Relative Trajectory in Chief's LVLH Frame
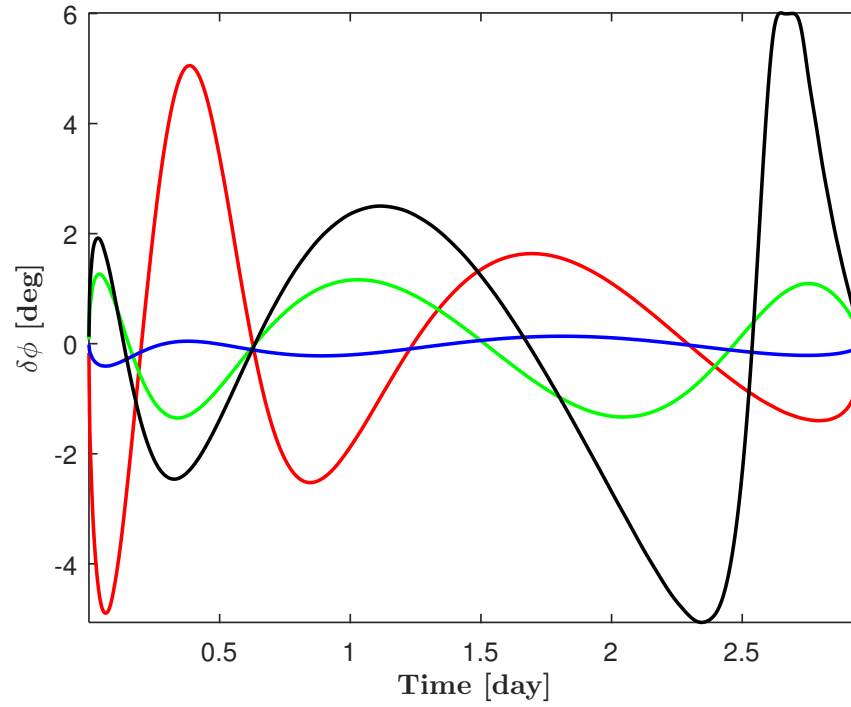
(b) Control Effort

Figure 4.12: Triangle Formation Establishment
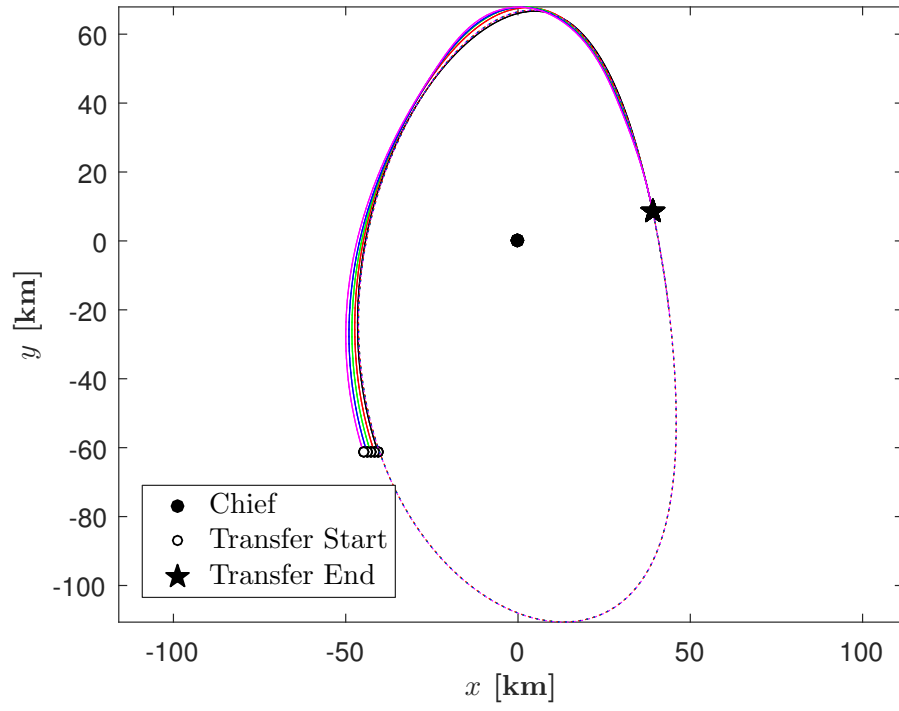
(a) Relative Trajectory in Chief's LVLH Frame
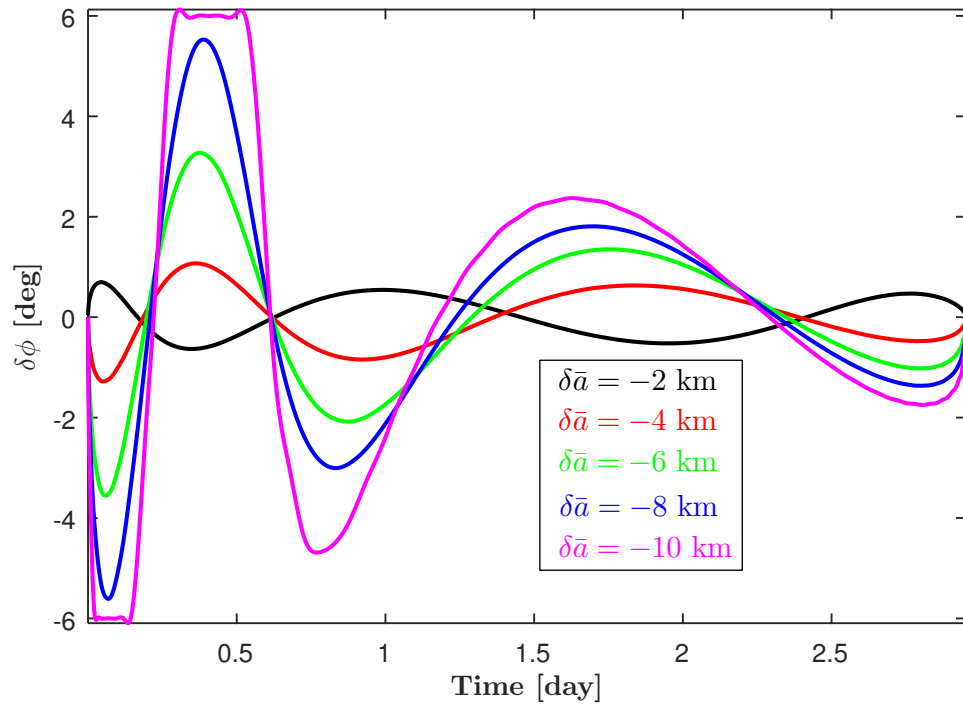
(b) Control Effort

Figure 4.13: Difficulty of Controlling Semi-Major Axis

Chapter 5

Conclusions

To study the spatial and temporal variations of plasma in the highly dynamic environment of the Earth's geomagnetic tail, a spacecraft formation must be deployed in a highly eccentric Keplerian reference orbit that has its apogee inside the science region of interest. The geomagnetic tail is always aligned with the Sun-Earth line and, therefore, rotates annually. Because Keplerian orbits are inertially fixed, the orbit apogee is only aligned with the geomagnetic tail once a year. Solar sails are capable of slowly rotating the orbit apse-line Sun-synchronously such that the orbit apogee remains inside the geomagnetic tail throughout the entire year, which can significantly increase the period of in situ observations inside the magnetosphere. In this dissertation, the feasibility of using solar sail formation flying to explore the Earth's magnetosphere, in particular the geomagnetic tail, is investigated.

5.1   Summary of Main Results

In Chapter 2, the effects of SRP perturbations in Sun-synchronous orbits are studied in detail using the averaging theory, which leads to the identification of the secular variations in the orbital elements. Next, the analytic first-order necessary conditions for a SRP invariant relative motion are derived, assuming that all solar sails in the formation maintain a Sun-pointing attitude. Numerical simulations are used to verify the validity of the conditions derived. It is shown that the first-order

necessary conditions lead to a quasi-periodic formation, as opposed to truly SRP invariant relative motion. This is a direct result of the first-order linear approximation used to derive the necessary conditions. Next, the average effects of small constant inaccuracies in the Sun-pointing attitude on the mean rates of orbital elements are derived analytically. The sensitivity analysis with respect to the sail's characteristic acceleration is investigated and it is shown that larger than 0.1% uncertainty in the characteristic acceleration of a sail leads to a significant changes in the size and the shape of a tight formation.

In Chapter 3, the problem of formation design is explored in detail using numerical optimization for two-craft, three-craft, and four-craft formations. First, it is shown how the slow secular drifts resulting from the analytic first-order conditions can be removed using numerical techniques. This leads to the design of truly SRP invariant solar sail formations. Motivated by NASA's MMS mission, the problem of formation design within a specific region of interest around the orbit apogee is investigated next. The proposed algorithm is applied to the design of in-plane two-craft, in-plane equilateral triangle, and tetrahedron formations. In all cases, various formation sizes ranging from 10 km to 400 km in terms of average inter-spacecraft range are explored. It is shown that the in-plane solar sail formation geometries are stable, while the tetrahedron formation is difficult to design assuming the Sun-pointing attitude. Next, the SRP invariant condition is numerically implemented in the formation design algorithm. The formations designed with the inclusion of the SRP invariant condition are shown to be more stable and to degrade at a lower rate. This increase in stability may come with a small penalty in the quality of the designed formation.

In Chapter 4, the problem of establishing the formations designed in Chapter 3 are discussed. First, a deployment scenario into the mission orbit is considered. From this deployment scenario, the relative geometry between the two solar sails are estimated after they are injected into the mission orbit. This is a crucial step before employing active control to achieve a desired formation; it allows for a solution to the formation establishment problem, assuming a pragmatic initial relative geometry. The formation establishment problem is solved using optimal control the-

ory, assuming that the deputy solar sail is capable of changing its attitude and that the chief solar sail flies in a Sun-synchronous orbit and does not employ active control. Since there is no analytic solution, numerical techniques are used to solve the optimal formation establishment problem. The commercial software package DIDO is employed, which uses Legendre pseudo-spectral method to turn the problem into a nonlinear programming problem that is solved using a sequential quadratic programming solver. Solutions to the optimal control problem are found for a simple leader-follower formation of various sizes. It is shown that changing the formation size may require a significantly different control effort for the same initial boundary conditions. The effects of changing the measure of optimality is also explored. It is demonstrated that smooth quadratic cost functions ($\mathcal{L}_2$ norms) lead to smoother control efforts when compared to non-smooth cost functions ($\mathcal{L}_1$ norms). This is especially important for solar sails since they are not capable of making abrupt changes to their orientations. Next, the effects of increasing the time-horizon for the optimal control is investigated and as expected, there is a reduction in control effort when the time-horizon is expanded; the deputy solar sail requires small changes to achieve the desired leader-follower formation. The optimal establishment of other SRP invariant relative orbits and triangle formations are studied next. It is demonstrated that the average semi-major axis is difficult to control as predicted by average theory. The results and conclusions are similar to those made in the optimal establishment of the leader-follower formation. Lastly, in order to draw comparisons between achieving desired relative motion using the sail alone and other low-thrust strategies, the establishment of a leader-follower formation using a hybrid system that combines solar sailing with solar electric propulsion (SEP) is investigated. Two low-thrust maneuver strategies are considered using a relatively small SEP thruster. It is shown that a formation may be established with a small amount of propellant for a fraction of time it takes to establish a formation using the sail alone.

5.2   Future Work

The research performed in this dissertation is by no means saturated in scope. There are many research areas available for enabling solar sail formation flying for the exploration of the Earth's geomagnetic tail. A few suggestions for building upon the work in this dissertation, which focuses on the mission design aspect of the problem, are discussed next.

A reasonable choice for future work is to include higher fidelity SRP models to verify the results from this dissertation once the exact design of the solar sails are known. In particular, the validity of the solar sail flat-plate model approximation used for deriving analytic expressions for the averaged rates of the orbital elements, as a result of sails' Sun-pointing attitude, need to be verified. Likewise, the necessary conditions for SRP invariant relative orbits in Sun-synchronous orbits need to be revisited when the best estimated force model for the sails is available.

Another interesting research area would be to revisit the optimal formation establishment problem to include third-body perturbations and higher fidelity SRP models. Furthermore, this dissertation only considered in-plane variations in the sail's attitude for establishing a desired relative geometry. Both in-plane and out-of-plane changes in a sail's orientation will be necessary in practice for establishing a desired relative motion, even if the sail lie in the same plane initially. The relative third-body effects will certainly create relative out-of-plane separations that the deputy solar sails must correct for before establishing the desired in-plane relative geometries discussed in this dissertation. Because of the highly coupled orbit-attitude dynamics of solar sails, a six DoF simulation for further validating the result of this dissertation is another good area for future work once the decision is made on the type of attitude control system for maintaining the Sun-pointing attitude.

Bibliography

[1] National Aeronautics and Space Administration. <u>Magnetospheric Multi-Scale Mission Overview</u>, 2015 (accessed August 27, 2016).

[2] National Aeronautics and Space Administration. <u>THEMIS and ARTEMIS Missions Overview</u>, 2015 (accessed August 27, 2016).

[3] European Space Agency. <u>Cluster Mission Overview</u>, 2015 (accessed August 27, 2016).

[4] Kyle Alfriend, Srinivas Rao Vadali, Pini Gurfil, Jonathan How, and Louis Breger. <u>Spacecraft formation flying: Dynamics, control and navigation</u>, volume 2. Butterworth-Heinemann, 2009.

[5] Nathan C Barnes, William C Derbes, Charles J Player, and Benjamin L Diedrich. Sunjammer: a solar sail demonstration. In <u>Advances in Solar Sailing</u>, pages 115–126. Springer, 2014.

[6] Richard H Battin. <u>An Introduction to the Mathematics and Methods of Astrodynamics</u>. AIAA Education Series, revised edition, 1999.

[7] Matteo Ceriotti and Colin R McInnes. Hybrid solar sail and solar electric propulsion for novel earth observation missions. <u>Acta Astronautica</u>, 69(9):809–821, 2011.

[8] Matteo Ceriotti and Colin R McInnes. Systems design of a hybrid sail pole-sitter. <u>Advances in Space Research</u>, 48(11):1754–1762, 2011.

[9] Guido Colasurdo and Lorenzo Casalino. Optimal control law for interplanetary trajectories with nonideal solar sail. <u>Journal of Spacecraft and Rockets</u>, 40(2):260–265, 2003.

[10] Howard Curtis. <u>Orbital mechanics for engineering students</u>. Butterworth-Heinemann, 2013.

[11] Steve Curtis. The magnetospheric multiscale mission... resolving fundamental processes in space plasmas. 1999.

[12] Bernd Dachwald. Optimal solar sail trajectories for missions to the outer solar system. <u>Journal of Guidance, Control, and Dynamics</u>, 28(6):1187–1193, 2005.

[13] Bernd Dachwald and Bong Wie. Solar sail kinetic energy impactor trajectory optimization for an asteroid-deflection mission. <u>Journal of Spacecraft and Rockets</u>, 44(4):755–764, 2007.

[14] Robert Gershman and Calina Seybold. Propulsion trades for space science missions. Acta Astronautica, 45(4):541–548, 1999.

[15] Sheng-ping Gong, Jun-feng Li, and He-xi Baoyin. Formation around planetary displaced orbit. Applied Mathematics and Mechanics, 28:759–767, 2007.

[16] Shengping Gong and Junfeng Li. Solar sail heliocentric elliptic displaced orbits. Journal of Guidance, Control, and Dynamics, 37(6):2021–2026, 2014.

[17] Shengping Gong, Junfeng Li, and Hexi BaoYin. Formation flying solar-sail gravity tractors in displaced orbit for towing near-earth asteroids. Celestial Mechanics and Dynamical Astronomy, 105(1-3):159–177, 2009.

[18] ShengPing Gong, JunFeng Li, HeXi Baoyin, and Jules Simo. A new solar sail orbit. SCIENCE CHINA Technological Sciences, 55(3):848–855, 2012.

[19] Shengping Gong, Gao Yunfeng, and Junfeng Li. Solar sail formation flying on an inclined earth orbit. Acta Astronautica, 68(1):226–239, 2011.

[20] Daniel J Grebow, Martin T Ozimek, and Kathleen C Howell. Advanced modeling of optimal low-thrust lunar pole-sitter trajectories. Acta Astronautica, 67(7):991–1001, 2010.

[21] Daniel J Grebow, Martin T Ozimek, and Kathleen C Howell. Design of optimal low-thrust lunar pole-sitter missions. The Journal of the Astronautical Sciences, 58(1):55–79, 2011.

[22] Jeannette Heiligers, Matteo Ceriotti, Colin R McInnes, and James D Biggs. Displaced geostationary orbit design using hybrid sail propulsion. Journal of Guidance, Control, and Dynamics, 34(6):1852–1866, 2011.

[23] Jeannette Heiligers and Colin R McInnes. New families of non-keplerian orbits: Solar sail motion over cylinders and spheres. In Advances in Solar Sailing, pages 851–870. Springer, 2014.

[24] Jeannette Heiligers and Colin R McInnes. Solar sail heliocentric earth-following orbits. Journal of Guidance Control Dynamics, 38:937–944, 2015.

[25] Steven P Hughes. A simple, powerful method for optimal guidance of spacecraft formations. 2005.

[26] Steven P Hughes. Formation design and sensitivity analysis for the magnetospheric multiscale mission (mms). In AIAA/AAS Astrodynamics Specialist Conference, Honolulu, HI, 2008.

[27] Steven P Hughes. General method for optimal guidance of spacecraft formations. Journal of guidance, control, and dynamics, 31(2):414–423, 2008.

[28] Donald E Kirk. Optimal control theory: an introduction. Courier Corporation, 2012.

[29] Shoji Kitamura, Yasushi Ohkawa, Yukio Hayakawa, Hideki Yoshida, and Katsuhiro Miyazaki. Overview and research status of the jaxa 150-mn ion engine. Acta Astronautica, 61(1):360–366, 2007.

[30] Wiley J Larson and James Richard Wertz. Space mission analysis and design. Technical report, Microcosm, Inc., Torrance, CA (US), 1992, pp. 353–497.

[31] Dale A Lawrence and Scott W Piggott. Integrated trajectory and attitude control for a four-vane solar sail. In AIAA Guidance, Navigation, and Control Conference and Exhibit, pages 15–18, 2005.

[32] M Leipold. To the sun and pluto with solar sails and micro-sciencecraft. Acta Astronautica, 45(4):549–555, 1999.

[33] Malcolm Macdonald, Gareth Hughes, Colin McInnes, Aleksander Lyngvi, Peter Falkner, and Alessandro Atzei. Geosail: An elegant solar sail demonstration mission. Journal of Spacecraft and Rockets, 44(4):784–796, 2007.

[34] Malcolm Macdonald and Colin McInnes. Analytical control laws for planet-centered solar sailing. Journal of Guidance, Control, and Dynamics, 28(5):1038–1048, 2005.

[35] L Mann, K Parsay, T Williams, and W Yu. Comparison of magnetospheric multiscale (mms) formation design algorithms. In 4th International Conference on Formation Flying, Montreal QUEBEC, 2011.

[36] Colin R McInnes. Solar sail trajectories at the lunar l2 lagrange point. Journal of Spacecraft and Rockets, 30(6):782–784, 1993.

[37] Colin R McInnes. Deflection of near-earth asteroids by kinetic energy impacts from retrograde orbits. Planetary and Space Science, 52(7):587–590, 2004.

[38] Colin R McInnes. Solar Sailing: Technology, Dynamics and Mission Applications. Springer, 2004.

[39] Colin R McInnes, Malcolm MacDonald, Vassilis Angelopolous, and David Alexander. Geosail: Exploring the geomagnetic tail using a small solar sail. Journal of Spacecraft and Rockets, 38(4):622–629, 2001.

[40] Robert McKay, Malcolm Macdonald, James Biggs, and Colin McInnes. Survey of highly non-keplerian orbits with low-thrust propulsion. Journal of Guidance, Control, and Dynamics, 34(3):645–666, 2011.

[41] Giovanni Mengali and Alessandro A Quarta. Optimal three-dimensional interplanetary rendezvous using non-ideal solar sail. Journal of Guidance, Control, and Dynamics, 28(1):173–177, 2005.

[42] Giovanni Mengali and Alessandro A Quarta. Rapid solar sail rendezvous missions to asteroid 99942 apophis. Journal of Spacecraft and Rockets, 46(1):134–140, 2009.

[43] Giovanni Mengali and Alessandro A Quarta. Optimal solar sail interplanetary trajectories with constant cone angle. In Advances in Solar Sailing, pages 831–850. Springer, 2014.

[44] Giorgio Mingotti, Jeannette Heiligers, and Colin McInnes. First-guess generation of solar sail interplanetary heteroclinic connections. In 2nd Conference on Dynamics and Control of Space Systems, DyCoSS2, pages Paper–IAA, 2014.

[45] Osamu Mori, Yoji Shirasawa, Yuya Mimasu, Yuichi Tsuda, Hirotaka Sawada, Takanao Saiki, Takayuki Yamamoto, Katsuhide Yonekura, Hirokazu Hoshino, Junichiro Kawaguchi, et al. Overview of ikaros mission. In Advances in Solar Sailing, pages 25–43. Springer, 2014.

[46] Esther Morrow, Daniel J Scheeres, and Dan Lubin. Solar sail orbit operations at asteroids. Journal of Spacecraft and Rockets, 38(2):279–286, 2001.

[47] Junshan Mu, Shengping Gong, and Junfeng Li. Reflectivity-controlled solar sail formation flying for magnetosphere mission. Aerospace Science and Technology, 30(1):339–348, 2013.

[48] Junshan Mu, Shengping Gong, and Junfeng Li. Coupled control of reflectivity modulated solar sail for geosail formation flying. Journal of Guidance, Control, and Dynamics, pages 1–12, 2014.

[49] Junshan Mu, Shengping Gong, Pengbin Ma, and Junfeng Li. Dynamics and control of flexible spinning solar sails under reflectivity modulation. Advances in Space Research, 56(8):1737–1751, 2015.

[50] Martin T Ozimek, Daniel J Grebow, and Kathleen C Howell. A collocation approach for computing solar sail lunar pole-sitter orbits. Open Aerospace Engineering Journal, 3:65–75, 2010.

[51] MT Ozimek, DJ Grebow, and KC Howell. Design of solar sail trajectories with applications to lunar south pole coverage. Journal of guidance, control, and dynamics, 32(6):1884–1897, 2009.

[52] Alessandro Peloni, Matteo Ceriotti, and Bernd Dachwald. Solar sail trajectory design for a multiple near-earth asteroid rendezvous mission. Journal of Guidance, Control, and Dynamics, 2016.

[53] Gerd Prölss. Physics of the Earths space environment: an introduction. Springer Science & Business Media, 2012.

[54] Christopher William Thomas Roscoe. Satellite Formation Design in Orbits of High Eccentricity for Missions with Performance Criteria Specified over a Region of Interest. PhD thesis, Texas A&M University, 2012.

[55] I Michael Ross. A primer on pontryagin's principle in optimal control. Collegiate Publishers, 2015.

[56] Carl G Sauer. Optimum solar-sail interplanetary trajectories. AIAA Paper, 76792, 1976.

[57] Hanspeter Schaub. Relative orbit geometry through classical orbit element differences. Journal of Guidance, Control, and Dynamics, 27(5):839–848, 2004.

[58] Hanspeter Schaub and Kyle T Alfriend. J2 invariant relative orbits for spacecraft formations. Celestial Mechanics and Dynamical Astronomy, 79(2):77–95, 2001.

[59] Hanspeter Schaub and John L Junkins. Analytical Mechanics of Space Systems. AIAA Education Series, 2nd edition, 2009.

[60] Giovanni Vulpetti, Les Johnson, and Gregory L Matloff. Solar sails: a novel approach to interplanetary travel. Springer, 2014.

[61] Thomas J Waters and Colin R McInnes. Periodic orbits above the ecliptic in the solar-sail restricted three-body problem. Journal of Guidance, Control, and Dynamics, 30(3):687–693, 2007.

[62] Bong Wie. Solar sail attitude control and dynamics, part one. Journal of Guidance, Control, and Dynamics, 27(4):526–535, 2004.

[63] Bong Wie. Solar sail attitude control and dynamics, part two. Journal of Guidance, Control, and Dynamics, 27(4):536–544, 2004.

[64] Xiangyuan Zeng, Shengping Gong, Junfeng Li, and Kyle T Alfriend. Solar sail body-fixed hovering over elongated asteroids. Journal of Guidance, Control, and Dynamics, pages 1223–1231, 2016.

Appendix A

Formation Establishment Using Solar Electric Propulsion

In this section, a natural leader-follower formation is established using a hybrid system that combines solar sailing with solar electric propulsion (SEP). The use of hybrid systems to control a solar sail is explored in Ref. [8, 24]. The main motivation for this section is to draw a comparison between the establishment of a solar sail formation using the sail alone to other low-thrust methods. As evident in Chapter 4, a formation may be established by making small and slow variations in the deputy's orientation. Although changing the sail's orientation through large angles is not practical, having small variations in the sail's orientation may be a problem, especially for a solar sail whose attitude is maintained via reflective tip-vanes. In such a system, changing the sail's orientation by a fraction of a degree may fall within the margin of error for the accuracy of the attitude control system. For these potential difficulties, the use of other low-thrust methods which require employing a hybrid solar sail system may be worth considering. An example of such a hybrid system is illustrated in Fig. A.1. In this hybrid spacecraft, part of the reflective surface is covered with thin film solar cells (TFSC), which are used to power the SEP thruster. The two sails employ the Sun-pointing attitude to precess their orbit apse-lines Sun-synchronously. The chief is assumed to be a low-cost solar sail that only maintains a Sun-pointing attitude, while the deputy is a hybrid system with a small SEP thruster. The problem of deployment and establishment of natural formations using low-thrust one-burn and two-burn maneuver strategies are discussed in detail. Because the SEP system is unable to fire thrusters in the direction of the sail's reflective surface, the for-

mation establishment problem is a constrained two-point boundary value problem (TPBVP). This constrained TPBVP is solved numerically using a predictor-corrector method.

A.1   Hybrid Solar Sail Mass

Although a hybrid sail enables the establishment of formation geometries that may not be possible with a solar sail alone, the design of such a system is significantly more difficult. With the additional mass of the SEP system, the required reflective surface area must increase in order to maintain the required characteristic acceleration given in Eq. (2.12) for Sun-synchronous precession of the orbit apse-line. Because the natural formation requires no formation maintenance, the SEP system is primarily used for establishing the desired formation. This allows for the selection of a small SEP system, leading to only a small increase in solar sail mass and reflective surface area. This section attempts to determine a **crude** mass estimation for a hybrid sail. The estimated mass is required to solve the low-thrust TPBVP. The initial mass of the hybrid solar sail m_0 may be written as [8] [22]

$$m_0 = m_{\text{propellant}} + m_{\text{tank}} + m_{\text{gimbal}} + m_{\text{SEP}} + m_{\text{power}} + m_{\text{sail}} \tag{A.1}$$

The tank and the gimbal masses may be approximated as $m_{\text{tank}} = 0.1m_{\text{propellant}}$ and $m_{\text{gimbal}} = 0.3m_{\text{SEP}}$, respectively [14]. The mass of the SEP thruster is $m_{\text{SEP}} = k_{\text{SEP}}P_{\text{SEP}_{\text{max}}}$ where the maximum power required by the SEP subsystem is determined by

$$P_{\text{SEP}_{\text{max}}} = \frac{T_{\text{max}}I_{\text{SP}}g_0}{2\eta_{\text{SEP}}} \tag{A.2}$$

The specific performance of the SEP thruster and the thruster efficiency are assumed to be $k_{\text{SEP}} = 0.02$ kg/W [30] and $\eta_{\text{SEP}} = 0.7$ [29], respectively. Because the SEP is primarily used for formation establishment and formation reconfiguration while the sail SRP acceleration is responsible for the artificial Sun-synchronous precession of the orbit apse-line, only a few kilograms of xenon gas is reserved for the SEP system. Thus, the propellant mass of $m_{\text{propellant}} = 5$ kg is proposed. The SEP
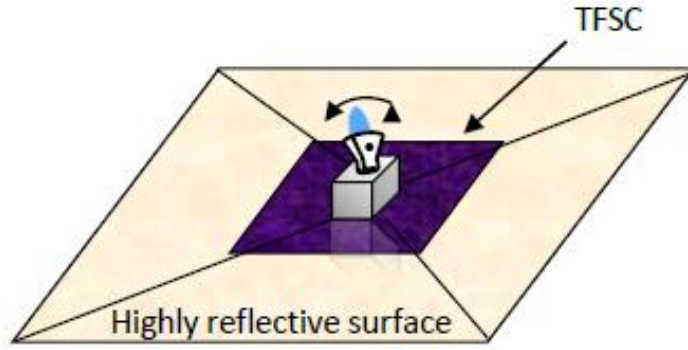
Figure A.1: A Hybrid Sail/SEP Spacecraft with a Steerable Thruster [8]

system is assumed to be able to generate the maximum thrust of $T_{\max} = 0.01$ N with an $I_{\mathrm{SP}} = 2500$ s. Such an SEP system falls directly within the scope of the current technology. To provide electrical energy to the SEP system, part of the sail area is covered with thin film cells [8]. The required area covered with solar cells is determined by the maximum power to be required by the SEP system and is computed using

$$A_{\mathrm{cells}} = \frac{P_{\mathrm{SEP}_{\max}}}{\eta_{\mathrm{cells}} W} \cos \gamma_{\mathrm{SEP}_{\max}} \tag{A.3}$$

where the efficiency of the thin film solar cells is assumed to be $\eta_{\mathrm{cells}} = 0.05$. The solar energy flux density at 1 AU is $W = 1367$ W/m^2. The angle $\gamma_{\mathrm{SEP}_{\max}}$ is the angle between the solar sail normal and the Sun-sail vectors at $T_{\max}$. The mass of the thin films is $m_{\mathrm{power}} = \sigma_{\mathrm{cells}} A_{\mathrm{cells}}$ where $\sigma_{\mathrm{cells}} = 100$ g/m^2 [22]. The mass of the sail subsystem is set to an ambitious value of $m_{\mathrm{sail}} = 100$ kg, which includes the spacecraft bus, instruments, and solar sail structure [33]. Summing over the individual components leads to a total initial mass of $m_0 = 120$ kg. This estimated total mass may be optimistic. However, changing the total mass has only minor effects on the finite burn outcome when solving the formation establishment problem. The estimated total mass is an acceptable initial guess for this analysis, since solving the constrained TPBVP is the main focus of this analysis.

The required characteristic acceleration to precess the apse-line of a 11 R$_{\mathrm{E}}$ × 30 R$_{\mathrm{E}}$ orbit Sun-synchronously is $k = 0.12119$ mm/s^2. Assuming a constant solar radiation of $P = 4.56 \times 10^{-6}$

Table A.1: Hybrid Sail/SEP Spacecraft Specifications

	Value	Unit
Max Thrust	0.01	N
I_{sp}	2500	s
Propellant Mass	5	kg
Total Mass	120	kg
Reflective Area	1876	m^2

N/m^2 and solar sail efficiency of $\eta = 0.85$, the required sail loading $\sigma = 2\eta P/k = m_0/A_s$ for generating the characteristic acceleration of $k = 0.12119$ mm/s^2 is 63.96 g/m^2. For a solar sail with a total launch mass of $m_0 = 120$ kg, a reflectable area of $A_s \approx 1876$ m^2 is required for generating the computed sail loading. The total surface area of the sail is computed using $A = A_s + A_{\mathrm{cells}}$. For a typical square sail configuration, the size of the sail is approximately 44 m $\times$ 44 m. Because the mass of the tank changes, the sail area for generating the required characteristic acceleration for the Sun-synchronous orbit changes. However, since the mass of the tank is small, this effect is neglected in this study. The hybrid spacecraft specifications are summarized in Table. A.1.

A.2　Low-Thrust Maneuvers for Formation Establishment

Formation establishment is a **constrained** TPBVP for a hybrid solar sail system because of the SEP system's inability to generate thrust in the direction of the sail's reflective surface. As described in Eq. (2.25), the desired formation is achieved upon nullifying the differential elements according to $\delta\boldsymbol{\alpha} = \begin{bmatrix} 0 & 0 & 0 & 0 & 0 & \delta f \end{bmatrix}^T$ at the orbit apogee. The main elements that require adjustment for establishing the desired formation are a, e, and ω, since the deployment takes place within the orbit plane. Although the main goal is to nullify δa, δe, and $\delta\omega$, there is a small variation in δi because of lunar-solar effects and it must be corrected for establishing the desired formation. Furthermore, the sails may not be inserted exactly into the nominally designed orbit plane, causing variations in δi and $\delta\Omega$. For these reasons, the relative out-of-plane motion must be corrected, even though the corrections are small relative to the corrections required for nullifying

the in-plane differential elements. The variation in $\delta\Omega$ is negligible. Therefore, only δi is nullified for correcting the relative out-of-plane motion in solving the TPBVP.

Although it is important to nullify all five differential elements mentioned to achieve the proposed natural formation, two differential elements are more important than the others, namely δa and $\delta\omega$. The identity $\delta a \equiv 0$ must hold for any bounded relative motion, such as the proposed natural formation. A nonzero δa causes the formation to drift apart due to each spacecraft having a different orbit period. Achieving $\delta a \equiv 0$ may not be possible in reality but $|\delta a|$ must be minimized to have a quasi-periodic relative motion. For the selected burn locations in this analysis, only $\delta\omega > 0$ can be nullified without violating the SEP physical constraint. This is explained in more detail in Section A.2.0.1.

Two solutions are proposed for solving the constrained TPBVP. In the first solution, a one-burn maneuver performed at the deputy's perigee is considered. For the second solution, the first burn is performed at the deputy's perigee and the second burn is performed at the deputy's apogee. To numerically solve the constrained TPBVP, a predictor-corrector procedure employing the **shooting** method is developed in the high-fidelity FreeFlyer® mission design software. The deputy's thruster is assumed to generate a constant thrust value of 0.01 N throughout the maneuver. Thruster burn direction is expressed in the deputy's local $\mathcal{V}$ frame. The differential element δf only affects the formation size and it has no influence on the shape of the relative orbit. Depending on the deployment strategy, enforcing a particular δf value may lead to overconstraining the problem and to the divergence of the predictor-corrector method for the selected number of burns and burn locations in this study. Therefore, the δf is not explicitly included in the predictor-corrector setup.

(a) Post-deployment orbit configuration

(b) Unit burn direction $\hat{T}$ in the deputy's local frame $\mathcal{V}$
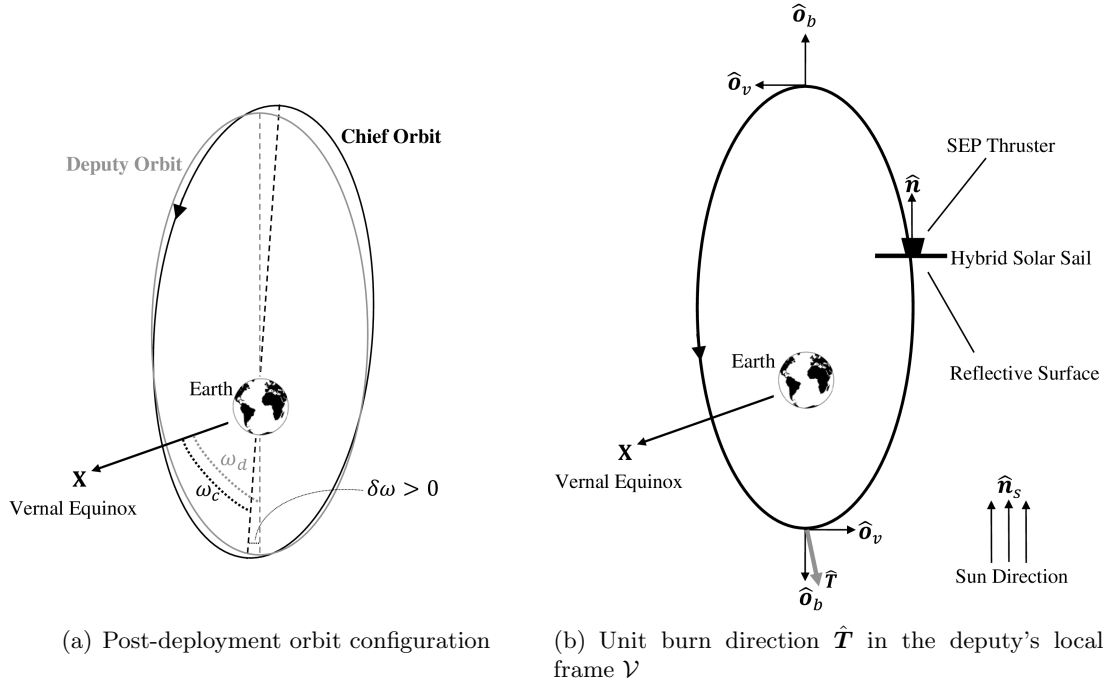
Figure A.2: Sign of $\delta\omega$ After Deployment and Direction of Burn in One-Burn Strategy

A.2.0.1 One-Burn Maneuver

Let $\hat{T}$ and Δt denote the finite burn unit direction and duration respectively. The finite burn starts at the deputy's perigee. Using the predictor-corrector method, $\hat{T}$ and Δt are modified until $\delta\boldsymbol{\mathrm{oe}} = \begin{bmatrix} \delta a & \delta i & \delta\omega \end{bmatrix}^T = \begin{bmatrix} 0 & 0 & 0 \end{bmatrix}^T$ is achieved at the next chief's orbit apogee. The differential element δe is not explicitly nullified in the one-burn strategy. As evident from Table. 4.1, the deputy must increase its semi-major axis and eccentricity to nullify the negative values of δa and δe. To increase both the semi-major axis and eccentricity by burning at orbit perigee, the deputy must burn along the velocity direction (i.e. $\Delta v_v > 0$). The corresponding increase in apogee radius, as a result of burning along velocity at perigee, leads to an increase in the deputy's semi-major axis and eccentricity. Note that depending on the values of the desired a and e and the initial orbit, a one-burn strategy at perigee does not always lead to achieving the desired a and e. In such case, both the perigee radius and the apogee radius must be adjusted, which requires a two-burn strategy.

The required burn direction at perigee to nullify $\delta\omega$ depends on the sign of post-deployment $\delta\omega$. To

---

while desired $\delta\text{œ}$ not achieved **do**

    modify finite burn (direction $^{\mathcal{V}}\hat{\boldsymbol{T}}$ and duration Δt)

    propagate formation to deputy's perigee

    maneuver deputy using finite burn

    propagate formation for one orbit

    check $\delta\text{œ} = \begin{bmatrix} \delta a & \delta i & \delta\omega \end{bmatrix}^T = \begin{bmatrix} 0 & 0 & 0 \end{bmatrix}^T$

end

**Algorithm 1:** Predictor-corrector setup for one-burn scenario

---

correct for the positive $\delta\omega$ value, the deputy must decrease its argument of perigee as illustrated in

Fig. A.2(a). Inspecting Eq. (2.13e), to have $\Delta\omega < 0$, we must have

$$\Delta v_b > \frac{2a}{2ae + r} \tan f \Delta v_v \tag{A.4}$$

where $\Delta v_v > 0$ and it is assumed that $\Delta v_h = 0$. Therefore, in order to decrease the deputy's

argument of perigee (i.e. to have $\Delta\omega < 0$) by burning at perigee, the condition of $\Delta v_b > 0$

must hold. This is the main reason why the chief solar sail is deployed first. Because if the order

of the deployment is switched, the deputy must then **increase** its ω to correct for $\delta\omega < 0$. At

perigee, this can only be achieved if the deputy executes a radially inward maneuver (i.e. $\Delta v_b < 0$),

which violates the SEP system's physical constraint as shown in Fig. A.2(b). For the deployment

scenario considered in Section 4.1, the predictor-corrector method converges to a burn unit direction

$^{\mathcal{V}}\hat{\boldsymbol{T}} = \begin{bmatrix} 0.00901 & -0.00413 & 0.99995 \end{bmatrix}^T$ and burn duration of 4011.092 seconds (≈ 67 minutes). As

expected, the burn direction is radially outward (along the bi-normal direction $\hat{\boldsymbol{o}}_b$) and has a positive

component along the velocity direction. The nonzero normal component is required to correct for

the small nonzero δi that is caused by the lunar-solar perturbations. The net change in velocity is

0.3343 m/s. The total propellant used by the deputy is approximately $\Delta m = 1.64$ g. Fig. A.3(a)

illustrates the entire scenario consisting of the formation deployment and the establishment of the

desired formation using the proposed one-burn maneuver at perigee. As noted earlier, the chief sail

is released first along the velocity direction. After 25 minutes, the deputy sail is released along a

direction that is 1° off the local velocity direction. Because there is a difference between the orbit
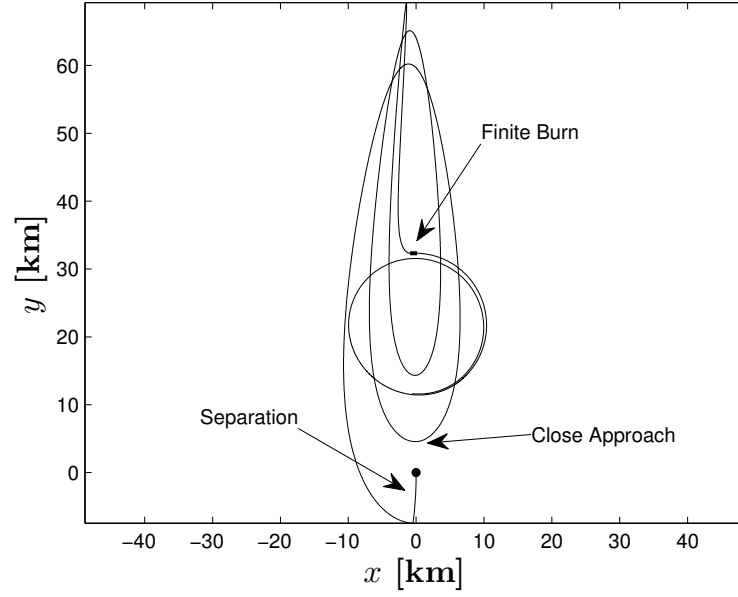
(a) Formation establishment via one-burn strategy at perigee
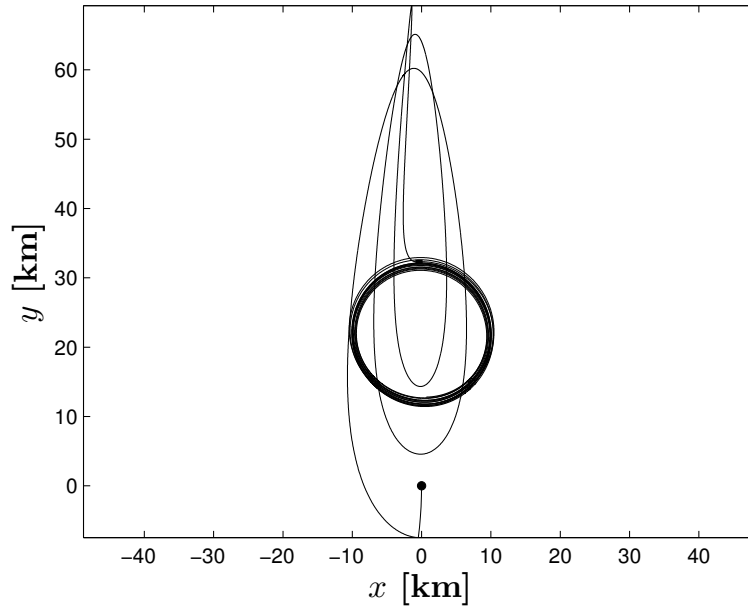
(b) 60 days of propagation post formation establishment

Figure A.3: Deployment and Formation Establishment as seen in the Chief's LVLH Frame

periods of the two sails due to nonzero δa, the deputy experiences a secular drift in the along-track direction during the next 3 orbits before the finite burn begins at the deputy's perigee. To analyze the formation's stability, the established formation is propagated for 60 days as illustrated
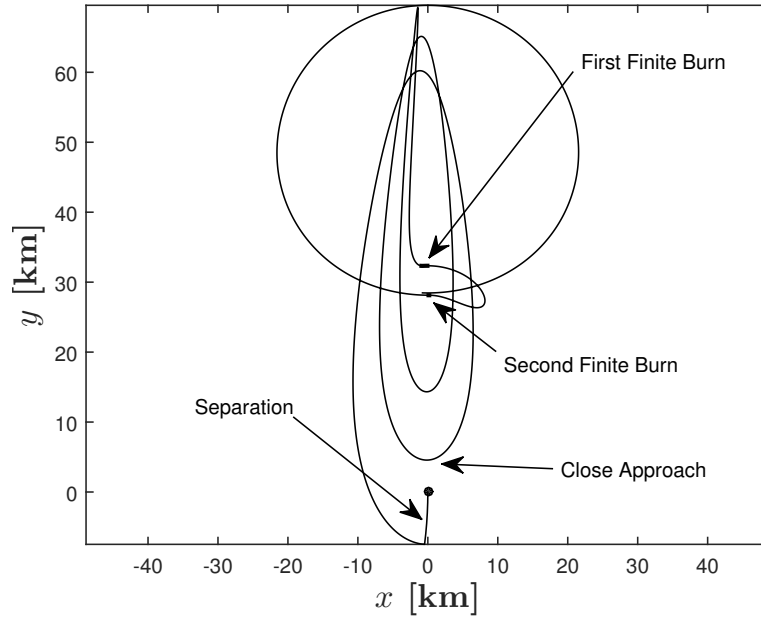
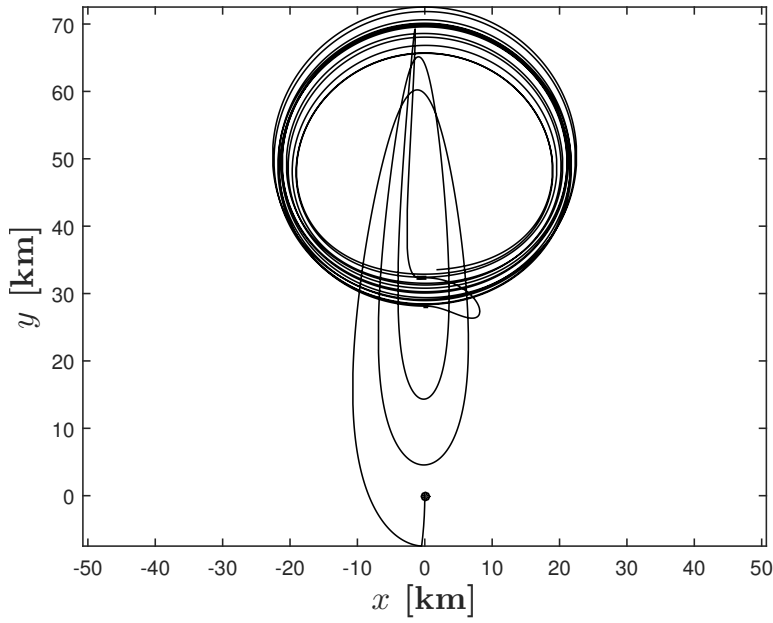(a) Formation establishment via two-burn strategy at perigee and apogee

(b) 60 days of propagation post formation establishment

Figure A.4: Deployment and Formation Establishment as seen in the Chief's LVLH Frame

in Fig. A.3(b). Despite the presence of the perturbations, the formation remains useful throughout the two months period.

A.2.0.2 Two-Burn Maneuver

Typically, changing the orbit semi-major axis and eccentricity requires adjusting both the perigee radius and apogee radius. Thus, a two-burn maneuver may be needed, depending on the post-deployment differential elements. In this case, the first burn is performed at perigee followed by the second burn at apogee. The two-burn strategy allows the deputy to nullify all four nonzero differential elements, namely δa, δe, δi, and $\delta \omega$. A sample two-burn solution for the same initial condition used in the one-burn scenario is shown in Fig. A.4(a). The established formation is propagated for 60 days to determine formation stability under perturbations. As

while desired $\delta œ$ not achieved **do**
    modify finite burn 1 (direction $^{\mathcal{V}}\hat{\boldsymbol{T}}_1$ and duration Δt_1)
    modify finite burn 2 (direction $^{\mathcal{V}}\hat{\boldsymbol{T}}_2$ and duration Δt_2)
    propagate formation to deputy's perigee
    maneuver deputy using finite burn 1
    propagate formation to deputy's apogee
    maneuver deputy using finite burn 2
    propagate formation for one orbit
    check $\delta œ = \begin{bmatrix} \delta a\ \delta e\ \delta i\ \delta \omega \end{bmatrix}^T = \begin{bmatrix} 0 & 0 & 0 & 0 \end{bmatrix}^T$
end

Algorithm 2: Predictor-corrector setup for two-burn scenario

shown in Fig. A.4(b), the relative trajectory remains quasi-periodic during the 60 day propagation period. Note that the closest approach of 4.6 km occurs at the next perigee following the deployment of the deputy sail. The required finite burn unit direction and duration for the first burn at perigee are $^{\mathcal{V}}\hat{\boldsymbol{T}}_1 = \begin{bmatrix} 0.0125 & -0.7161 & 0.6979 \end{bmatrix}^T$ and $\Delta t_1 = 4108.741$ seconds ($\approx$ 68.5 minutes). For the second burn at apogee, the finite burn unit direction and duration are $^{\mathcal{V}}\hat{\boldsymbol{T}}_2 = \begin{bmatrix} -0.0335 & -0.7447 & -0.6665 \end{bmatrix}^T$ and $\Delta t_2 = 1444.163$ seconds ($\approx$ 24 minutes). The net velocity change for the two burns are 0.2571 m/s and 0.0905 m/s, respectively. The propellant expenditure for the first burn and the second burn are approximately $\Delta m_1 = 1.68$ g and $\Delta m_2 = 0.59$ g, respectively. Both burn directions satisfy the SEP physical constraint. Inspecting the second component in both burn unit directions, it is clear that the transfer trajectory is an out-of-plane transfer orbit. The maximum out-of-plane point in the transfer trajectory is 3 km.

From the perspective of ground system support, it is best to minimize the number of maneuvers to lower the cost of staffing and expensive communication network coverage. Thus, the one-burn strategy has an advantage over the two-burn strategy in terms of mission support cost. Furthermore, the net velocity change for the one-burn maneuver is slightly more efficient than the two-burn maneuver (by approximately 13.3 mm/s). The main drawback of the one-burn maneuver is that it is not always possible to establish the desired formation using a single burn, especially when large errors are introduced during deployment. Because the SEP system is only used for the purpose of establishing the formation, only a small and light SEP system is required. It is shown that the desired formation may be established via a modest 0.01 N SEP thruster with an I_{SP} of 2500 s. The constrained two-point boundary value problem (TPBVP) of formation establishment is numerically solved using two low-thrust maneuver strategies taking place at perigee and apogee shortly after injection into the GEOSAIL mission orbit.

Appendix B

Optimized Initial Conditions for Triangle Formations

Table B.1: Optimized Initial Conditions for Triangle Formation of Size 10 km

Orbital Elements	Chief	Deputy 1	Deputy 2
a	130751.8085	130751.8085	130751.8085
e	0.463414634146341	0.463446311608762	0.463484360867204
ω	$0°$	$0.00987803923541°$	$0.00130477164328°$
M	$180°$	$179.985400692904°$	$179.998483986702°$

Table B.2: Optimized Initial Conditions for Triangle Formation of Size 160 km

Orbital Elements	Chief	Deputy 1	Deputy 2
a	130751.8085	130751.8085	130751.8085
e	0.463414634146341	0.464160628795219	0.464096312392204
ω	$0°$	$0.0653062296582088°$	$-0.0718207441407206°$
M	$180°$	$179.925328159501°$	$180.091934788862°$

Table B.3: Optimized Initial Conditions for Triangle Formation of Size 400 km

Orbital Elements	Chief	Deputy 1	Deputy 2
a	130751.8085	130751.8085	130751.8085
e	0.463414634146341	0.465522424638437	0.464770398302903
ω	$0°$	$0.103832134255972°$	$-0.243214594819135°$
M	$180°$	$179.864170293478°$	$180.342626213542°$